Schopp Philipp, BSc

CFD Simulation Approach: Characterizing an Advanced Polymer Electrolyte Fuel Cell

MASTER`S THESIS

to achieve the university degree of

Diplom-Ingenieur

Master´s degree programme: Chemical and Process Engineering

submitted to

Graz University of Technology

Supervisor

Assoc.Prof. Dipl.-Ing. Dr.techn. Viktor Hacker

Institute of Chemical Engineering and Environmental Technologies

Graz, January 2017

AFFIDAVIT

I declare that I have authored this thesis independently, that I have not used other than the declared sources/resources, and that I have explicitly indicated all the material which has been quoted either literally or by content from the sources used. The text document uploaded to the TUGRA-Zonline is identical to the present master´s thesis.

06.01.17
_____
Date

_____
Signature

ACKNOWLEDGEMENTS

ABSTRACT

In the thesis at hand a computational fluid dynamic system (CFD) is applied to model fuel cell operation behavior. In the beginning, theoretical basics concerning the components and the assembly of a fuel cell are discussed. Subsequently the CFD software used for the investigation is presented. In this context the fundamentals of the application required for its use are shown. Upon this section the experimental processing is described. The settings and the conduction of the required laboratory examination are discussed. On the other hand, the preparation for the CFD simulation is presented. In this context, the focus is on the generation of the computational mesh and the geometrical requirements of the fuel cell to be reproduced. Furthermore, several issues concerning the transfer of operation conditions from the laboratory examination to the CFD simulation are discussed.

Based on the preceding description of both investigations, the results are presented. The quality of the resulting data, particularly in context of the CFD simulation, is of special concern as the required computing power to reach full convergence of all observed parameters was not available. Furthermore, a comparison of the results from polarization curve simulation is presented. In conclusion, spatial distribution characteristics of reaction current density and temperature from laboratory examinations are compared to simulation results. In this context, feed gas distributions within the flow field channels are also discussed as a result of the CFD simulation.

KURZFASSUNG

In der vorliegenden Masterarbeit untersucht ein von Computational Fluid Dynamics System (CFD) zur Modellierung des Betriebsverhaltens von Brennstoffzellen angewandt. Am Beginn werden theoretische Grundlagen zu den Bauelementen und dem Aufbau einer Brennstoffzelle vorgestellt. Folgend wird die zur Untersuchung herangezogene CFD-Software vorgestellt. In diesem Zusammenhang werden die Grundlagen zur Anwendung der Software erörtert. Daraufhin wird die experimentelle Vorgehensweise präsentiert. Es werden die im Labor durchgeführten Experimente dargestellt, und die Vorbereitung zur Durchführung der CFD-Simulation wird erläutert. Dabei wird spezielles Augenmerk auf die Erstellung des Berechnungsgitters sowie der geometrischen Ausgangsbedingungen der zu simulierenden Brennstoffzelle gelegt. Des Weiteren werden mehrere Themen bezüglich des Transfers der Betriebsbedingungen von der Laboruntersuchung zur CFD-Simulation diskutiert.

Dabei ist die Qualität der Ergebnisdaten, speziell hinsichtlich der CFD-Berechnung, von besonderem Interesse, da die notwendige Rechenleistung zum Erreichen vollständiger Konvergenz aller beobachteten Größen nicht vorhanden war. Es wird ein Vergleich der Simulation einer aus Laborversuchen ermittelten Polarisationskurve vorgestellt. Anschließend werden aus Laboruntersuchungen hervorgehende Verteilungscharakteristika von Stromdichte und Temperatur mit Simulationsergebnissen verglichen. Ebenso werden Simulationsergebnisse zu den Verteilungen von Reaktionsgasen in den Strömungskanälen der Brennstoffzelle diskutiert.

TABLE OF CONTENTS

1. Introduction

The climate change represents a major challenge, which humanity has to face within the 21st century. National and international efforts try to reduce carbon dioxide emissions generated by society. One key to bear to a sustainable community is to use technologies which are polluting the earth's environment less than present technologies. Their implementation into our everyday life is an important step to a green and sustainable society.

Measurements of the carbon dioxide content in the atmosphere show that its concentration is steadily increasing as it is shown in Figure 1. Only a broad worldwide alliance will be able to solve this issue. Therefore, one can reckon that within the first half of the 21st century the use of carbon and hydrocarbon based fuels will likely be regulated. The political decisions made in this critical phase will determine which and when new technologies will enter the market [1].
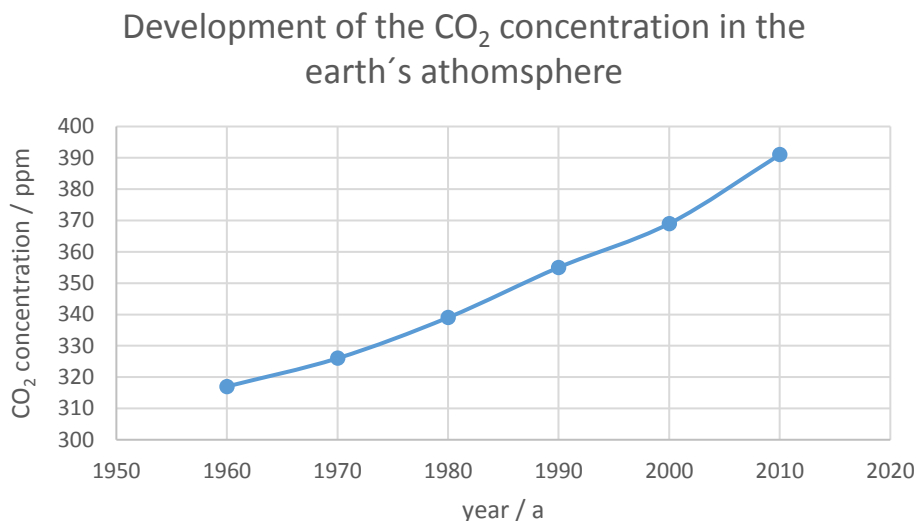
Figure 1: Development of the CO_2 concentration in the earth´s atmosphere. Interpolated data measured on the Mauna Loa, Hawaii, since 1959 [1].

The ongoing research on alternative technologies is spread widely. Candidates for a clean future are technologies based on hydrogen. Compared than fossil fuels, hydrogen does not produce any carbon dioxide when burned.

Hydrogen can be used to produce electric power with fuel cells. Within such a device, hydrogen is oxidized electrochemically to water. The energy is converted directly into electrical power. Fuel cell technology can be regarded an alternative to conventional thermodynamic cycles like coal-fired power plants, gas turbines and internal combustion engines. The advantage of the electrochemical conversion in a fuel cell is the fact that higher efficiencies can be reached in comparison to these thermodynamic cycles, for instance occurring in combustion engines [1].

The energy generation of our society tends to decentralization in the future [2]. Production of electricity will take place where it is consumed. This approach allows to keep transmission and transformation losses low. Furthermore, decentralization is seen as an aspect of the current energy revolution. However, this trend opens another market for the fuel cell: compared to power plants based on thermodynamic cycles as common nowadays, the efficiency of a fuel cell is independent of its size most widely. The advantage of the fuel cell is that a high degree of efficiency can be reached in a small scale plant [1]. Therefore, the fuel cell is an ideal candidate for decentralized energy production maybe leading to a paradigm shift in electricity generation [1].

Important for the clean operation of a fuel cell system is the production of hydrogen. Only if the fuel is produced sustainably, the fuel cell can be called a green technology.

Until now, hydrogen is mainly made by reforming natural gas, heavy oil and coal [1]. To reduce the global carbon dioxide emission, the generation of hydrogen needs to be based on regenerative energy technologies. This means, hydrogen has to be produced either by reforming renewable resources or with electricity coming for instance from wind turbines, hydroelectric power plants or photovoltaic power plants.

The generated electricity then can be used for electrochemical production of hydrogen. In electrolysis-plants, water is split into its components: hydrogen and oxygen. Whilst oxygen can be released into the atmosphere, hydrogen acts as energy carrier and can be distributed to where electricity provided by fuel cells is required. Nowadays, hydrogen pipelines are successfully established in Germany, France and the United States [1].

To overcome the carbon dioxide emission issue, a mix of several new technological approaches will be necessary. Fuel cells exhibit the potential to be part of this mix and to contribute to a sustainable and clean future. However, aside from that, the fuel cell is an alternative technology, independent of the advantage of being clean. Compared to common technologies for energy generation, its performance limits are not exhausted yet and it may lead to an extensive shift of everyday electricity generation: From thermodynamic cycles to electrochemical power plants.

2. Theory I: Fuel Cell

To introduce the theoretical principles of fuel cell technology to the reader, the most important issues of this topic are shown subsequently. Next to general theoretical approaches concerning the working principle, focus will be laid on the construction of a fuel cell. This includes extended discussion of fuel cell elements and requirements to successfully operate fuel cells.

2.1. Fuel Cell Overview

To give an overview of fuel cell basics, this chapter discusses the main topics required for the understanding of adjacent issues. Subsequently, a glance is thrown at the working principle, the measurement techniques and the practical use of fuel cells.

2.1.1. Working Principle

A fuel cell is a device which converts chemical energy into electrical energy. For continuous operation, it needs to be supplied with hydrogen and oxygen continuously. Unlike common plants, fuel cells convert the reactants directly into electrical power. They exhibit no intermediate steps, where heat is transformed into kinetic energy finally generating electrical energy.

Commonly, fuel cells are driven by carbon-free fuels, therefore only minimal pollution occurs. Thus, fuel cells are a technology to reduce greenhouse gases and toxic emissions. Figure 2 shows the general operation principle of a fuel cell.
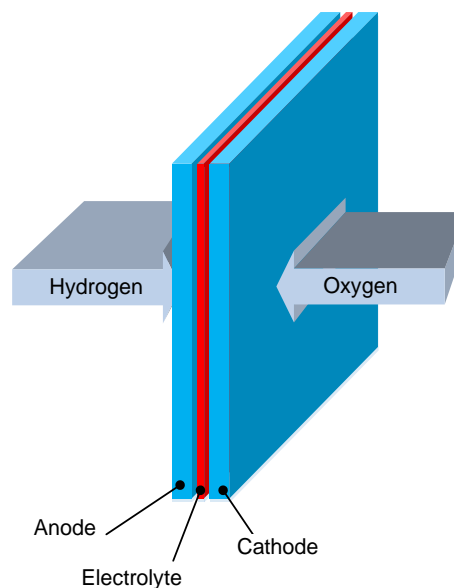

Figure 2: General principle of a fuel cell. The illustrated elements are required for the conversion of hydrogen and oxygen to water and electrical energy.

As can be seen, hydrogen and oxygen are fed into the device. Furthermore, components such as anode, cathode as well as an electrolyte are required. By means of this construction, hydrogen and oxygen are consumed, generating water as shown in Formula 1.

$$2\,H_2 + O_2 \rightarrow 2\,H_2O$$
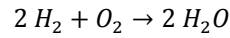
Formula 1: Reaction of hydrogen and oxygen generating water.

On the anode and the cathode side, fuel and oxygen, respectively, are converted. On the anode, the fuel is oxidized and oxygen is reduced on the cathode. The electrolyte separates the cathode from the anode. It ensures that only charge carrying species are transported through without allowing electric conduction. Electrons, being charged negatively, have to run through an external circuit to get from the anode to the cathode side. This way, an external appliance can be powered with electrical energy.

The design of the fuel cell is strongly dependent of its type. Since the invention of the fuel cell in 1838/39 [3], a variety of versions have been developed. Today, four types of fuel cells can be considered as the most important ones. These include the Molten Carbonate Electrolyte Fuel Cell (MCFC), the Solid Oxide Fuel Cell (SOFC), the Proton-Exchange Membrane Fuel Cell (PEMFC) and the Alkaline Fuel Cell (AFC) [4]. They are mainly distinguished from each other by using different electrolytes and operation temperatures.

2.1.2. PEM Fuel Cell

Within this thesis, a special fuel cell type is examined: The *PEMFC*. This notation is used for the extended description of *proton exchange membrane fuel cell* or *polymer electrolyte membrane fuel cell*.

The composition basically follows the scheme shown in Figure 3. The gas supply takes place spatially separated: At the anode side, hydrogen is provided and at the cathode side, oxygen is provided. At the anode, molecular hydrogen is split up into H^+-ions and electrons, as Formula 2 illustrates. This oxidation reaction happens by assistance of a catalyst, fixed to the anode.

$$2\,H_2 \rightarrow 4\,H^+ + 4\,e^-$$
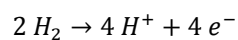
Formula 2: Oxidation of molecular hydrogen, being split into H^+-ions and electrons.

The space between anode and cathode is filled up with a membrane which is permeable only for protons but not for electrons. Therefore, the H^+-ions can pass through the membrane while the electrons must run through an external appliance to close the circuit, as shown in Figure 3.
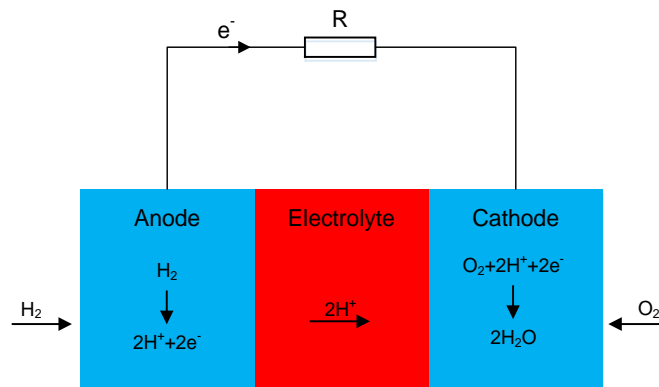
Figure 3: Scheme of a fuel cell. The protons can pass through the electrolyte while the electrons run via an external appliance.

At the cathode, oxygen is reduced. H^+-ions, electrons and oxygen react, forming water molecules as shown in Formula 3.

$$O_2 + 4\,H^+ + 4\,e^- \rightarrow 2\,H_2O$$
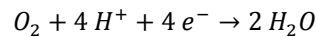
Formula 3: Reduction of oxygen. It takes up the electrons and reacts with protons, forming water.

The PEMFC distinguishes itself from other fuel cell types by using a polymeric membrane. The membrane is solid and only permeable for H^+-ions, but not for electrons. The most widely used material for the membrane is called Nafion®. It is a thermoplastic polymer, which uses -SO_3H groups to conduct the protons through the solid [4].

The reaction of 2 H_2 and O_2 creating 2 H_2O, as shown in Formula 1, exhibits a reaction enthalpy of ΔH_R = - 72 kJ mol^{-1} [5]. Therefore, the reaction is exothermic and gives off heat. When operating single cells, this phenomenon is of no special interest, as the fuel cell needs to be heated anyway to sustain operation temperature. However, when operating a fuel cell stack, the overall electrochemical reaction heat is important to be known. Usually, this excessive heat needs to be drained from the stack to prevent thermal destruction of components.

To investigate the electrochemical reaction as well as the materials used in a fuel cell, different measurement techniques are used. Subsequently two important approaches are shown.

2.1.3. Measurement Techniques

For the characterization of fuel cells, electrical measurement techniques are required. Following, two basic proceedings are discussed being able to gain knowledge about the properties of a fuel cell being in operation.

2.1.3.1. Polarization Curve

To describe the performance of a fuel cell, the polarization curve model can be used. It describes the total losses occurring during operation and allows the characterization of different operation states.

The polarization curve describes the cell voltage as a function of the current density. Figure 4 illustrates the voltage behavior and lists three regions inherent to the polarization curve.
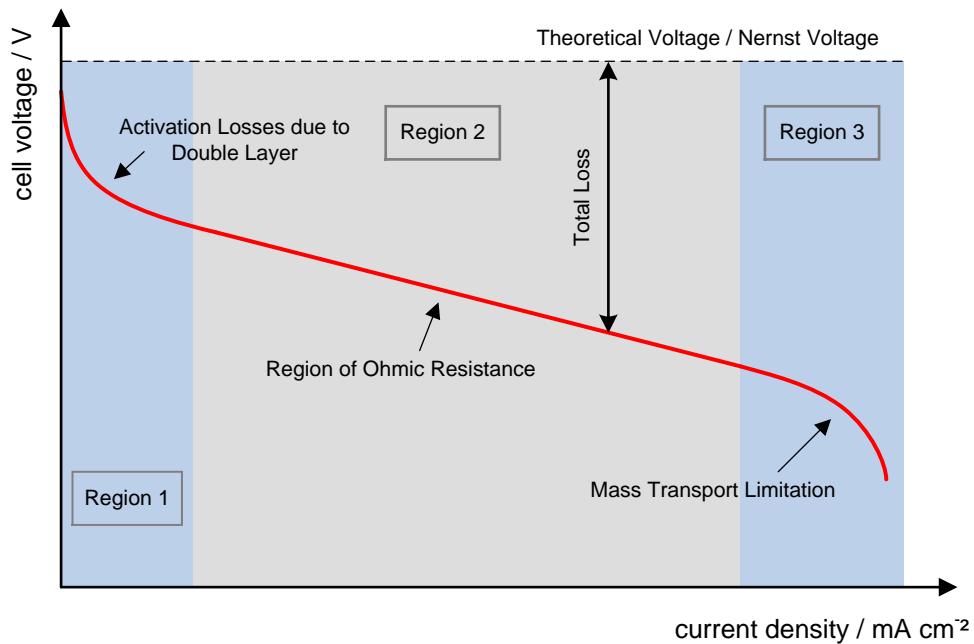
Figure 4: Polarization curve to characterize fuel cell operation. In the three regions, different types of losses dominate [3].

To formally describe the curve shown in Figure 4, the shares of the total loss need to be considered. Formula 4 [6] illustrates an approach to specify the nonlinear behavior of the cell voltage:

$$E_{cell} = E_{Nernst} - \eta_{act} - R_\Omega * j - \eta_{trans}$$

Formula 4: Description of the cell voltage function by means of loss terms.

The cell voltage E_{cell} is deceased by loss terms. The starting point is the Nernst Voltage E_{Nernst} representing the cell voltage at thermodynamic equilibrium [6]. It is equal to the open circuit voltage which basically incorporates the voltage of the fuel cell with at a current of 0 A. The three subtracted loss terms are typical for the three regions of the polarization curve. In each region, one of the loss terms dominates the two others.

The activation losses, illustrated by η_{act}, result from an electrode process called *polarization* [6]. It is caused by the development of an *electrochemical double layer* between electrolyte and membrane material and characterizes Region 1 shown in Figure 4. When the double layer is fully developed, the resistance and therefore the activation losses η_{act} are widely independent of the applied load.

6

Region 2 in Figure 4 is characterized by the existence of ohmic resistance R_Ω. Ohmic losses result from applying a current load j. Due to the fact that the electric conductivity in the electrodes is typically 40 times higher than the ionic conductivity of the membrane [3], the resistance is mainly caused by the membrane.

In Region 3 of the polarization curve, limited mass transport is the dominating effect. As the gas diffusion layer (refer to chapter 2.2 for further information) exhibits a fine structure, hydrogen and oxygen are transported to the reactive area via diffusion. In case of high voltages, not enough educts can be brought to the reactive zone and therefore, a drop of the cell voltage can be observed [3]. The resistance associated to this effect is expressed by the term η_{trans}.

To characterize the values of the terms shown in Formula 4, further measurement techniques can be useful. To obtain values for the ohmic resistance, an electrochemical impedance spectroscopy can be taken into account [6].

2.1.3.2. Electrochemical Impedance Spectroscopy (EIS)

The electrochemical impedance spectroscopy is a tool to describe various phenomena in a fuel cell. For instance it can be used to assign electrical losses to different processes[7].

The technique works by means of the electrical impedance. The *impedance* of an alternating current system represents the equivalent to the ohmic resistance of a direct current system. The impedance Z is of interest, as soon as a phase shift φ of current and voltage in an alternating current system occurs. Figure 5 (left) shows the principle of a phase shift over time. It can result from different electrical elements such as capacitors or inductors in series or parallel connections.

In general, the impedance Z is composed of the ohmic resistance R and the reactance X as shown in Formula 5 [6]. The reactance X results from the existence of a phase shift φ. j illustrates the imaginary unit $\sqrt{-1}$. In this context, all values except for j are considered as vectors.

$$\underline{Z} = \underline{R} + j * \underline{X}$$

Formula 5: Composition of the impedance Z in an alternating current system.

Formula 6 gives an impression how values of the impedance Z are calculated for electronic elements. The resistor only exhibits the ohmic share while the capacitors´ impedance is depending on its capacity C and the applied frequency ω.

$$Resistor: Z = R, \quad Capacitor: Z = \frac{1}{j * \omega * C}$$

Formula 6: Calculation of impedance values of resistor and capacitor [6].

As shown in Figure 5 (right), the shares of ohmic resistance R and reactance X are depending on the phase shift φ. Capacitive reactance leads to negative φ-values, inductive reactance leads to positive φ-values. When no phase shift is present, the impedance Z only consists of the ohmic resistance R.
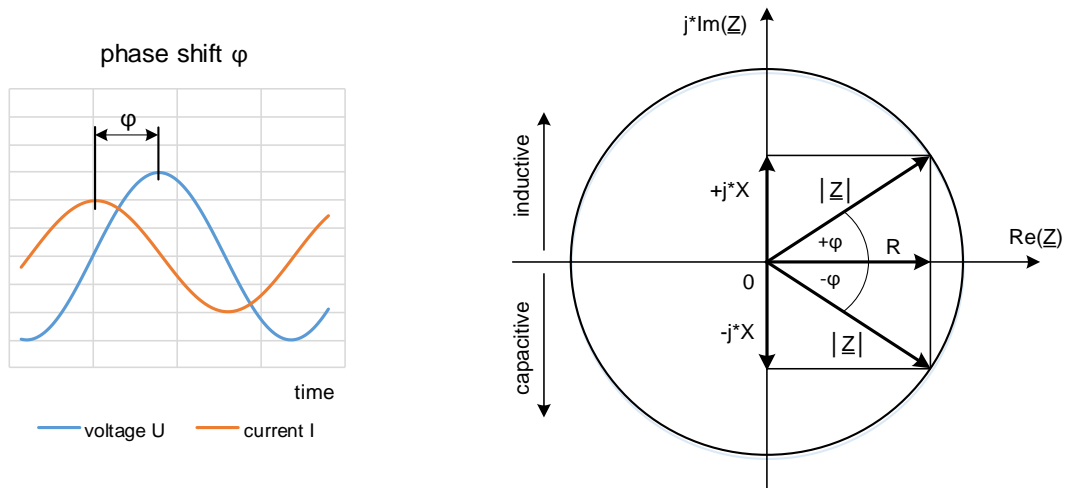
Figure 5: Alternating current systems can show a phase shift φ in respect to voltage and current being time variant (left). The shares of the impedance Z are depending on the phase shift φ (right) [6].

To understand the impedance spectroscopy in terms of measuring techniques, an equivalent circuit model needs to be generated alinged to the physical model of a fuel cell. As shown in Figure 6, the MEA can be modelled as a series connection of an ohmic resistance and two parallel connections [6]. With this illustration it becomes obvious, that impedance spectroscopy can be useful investigating fuel cells: The parallel connections of ohmic resistance and capacitor lead to a phase shift φ when applying alternating current.
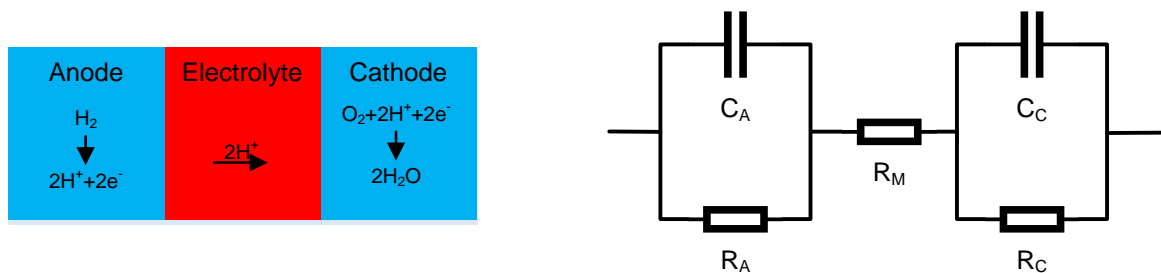
Figure 6: Physical model of the reactive zone of a fuel cell (left). The resistances of this physical model can be illustrated as a combination of parallel and series connections of ohmic resistors and capacitors (right) [6].

As Formula 6 shows, the impedance of a capacitor is depending on the frequency ω. Therefore, the impedance of the equivalent circuit model in Figure 6 depends on the applied frequency too. By scanning across a frequency range, phenomena occuring at specific frequencies can be observed [6]. This implies, that it is possible to separate processes which take place at different timescales,for instance anode or cathode activation, diffusion or relaxation phenomena [3].

2.1.4. Enhanced Use - Stack Basic

In practical application, single cells are combined to a *stack*. By using a serial connection between single cells, higher voltages are generated. This is a necessity for the use of fuel cells to supply every day applications. Different geometrical arrangements how to arrange single cells can be put together exist [7]. The most common composition is the bipolar construction as shown in Figure 7.
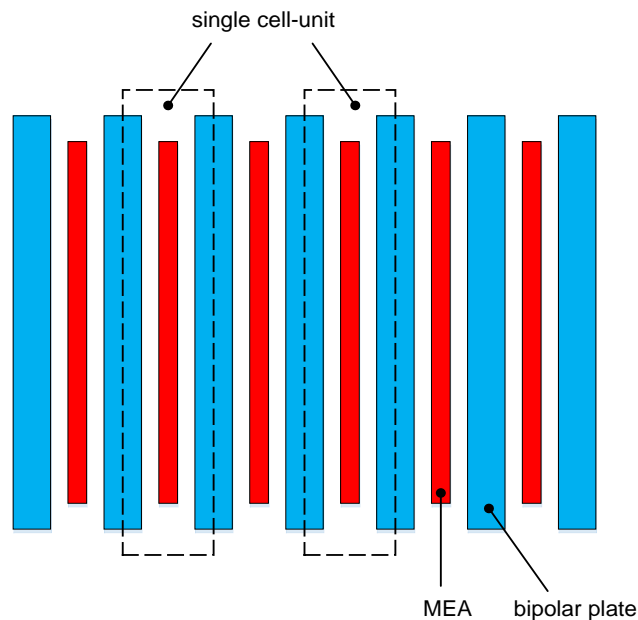
Figure 7: Single cells connected in series form a stack by means of a bipolar connection.

Figure 7 shows how the arrangement of the different elements of a stack can be realized. The main parts are the *bipolar plates* and the *membrane-electrode assembly (MEA).* For practical use, they need to be fixed to each other by means of endplates and tie rods, as shown in chapter 2.5.

Figure 8 illustrates an exploded view of a PEMFC-stack. The construction is equivalent to the scheme shown in Figure 7. To ensure a proper distribution of the hydrogen and the air, gas flow channels are integrated into the bipolar plates. The combination of a bipolar plate and a membrane-electrode-assembly is called *repeat unit*. The higher the resulting voltage needs to be, the more repeat units have to be put into a row.
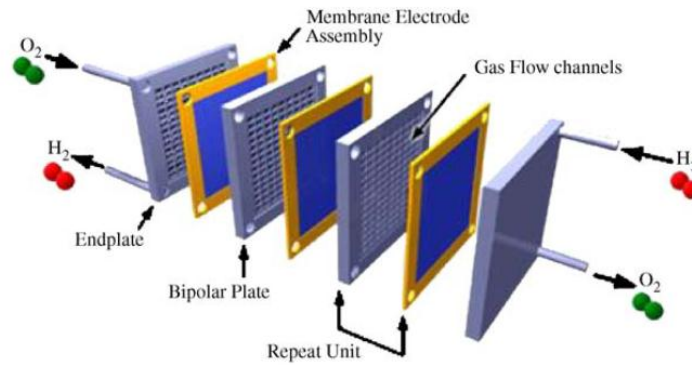
Figure 8: Exploded view of a PEMFC stack. The more repeat units, the higher the voltage [8].

This thesis treats single cell operation behavior, the theory shown subsequently will sometimes refer to stack construction. The extent of practical fuel cell use is shown. The elements required for single cell and stack construction are basically the same. Expanded information concerning fuel cell parts is shown to gain a more detailed understanding of the matter discussed.

2.2. Membrane-Electrode-Assembly (MEA)

The membrane-electrode-assembly (MEA) the most important part of the fuel cell as it is providing the electrochemical reaction converting hydrogen and oxygen. It consists of different layers which are assembled. Figure 9 shows the composition of a MEA.

Figure 9: The membrane-electrode-assembly is composed of several layers.

In the core a *polymer-electrolyte-membrane* (PEM) is accommodated. It is sandwiched between a cathode and an anode layer, consisting of thin layers of a catalyst usually on carbon support, so

called *catalyst layers* (CL). Upon them, *gas diffusion layers* (GDL), taking care of a homogenous distribution of the reaction gases, are fixed. Usually, between the catalyst layer and the gas diffusion layer, a microporous layer is placed for an optimized water management [4].

Figure 10 shows a microscope photography of a MEA cross-section. It shows that the catalyst layers are very thin compared to the PEM and the GDL. Furthermore, the microporous-layer shows a texture much finer than the GDL itself.
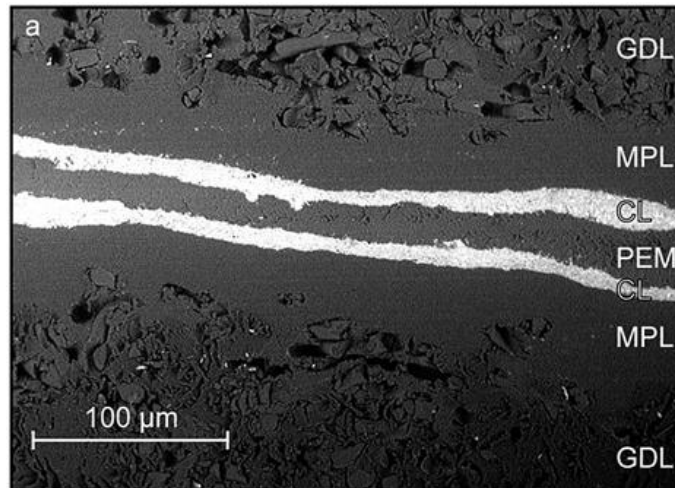
Figure 10: Microscope photography of a MEA cross-section. A microporous layer (MPL) is placed in between the gas diffusion layer (GDL) and the cathode layer (CL) to optimize water management [9].

2.2.1. Polymer-Electrolyte-Membrane (PEM)

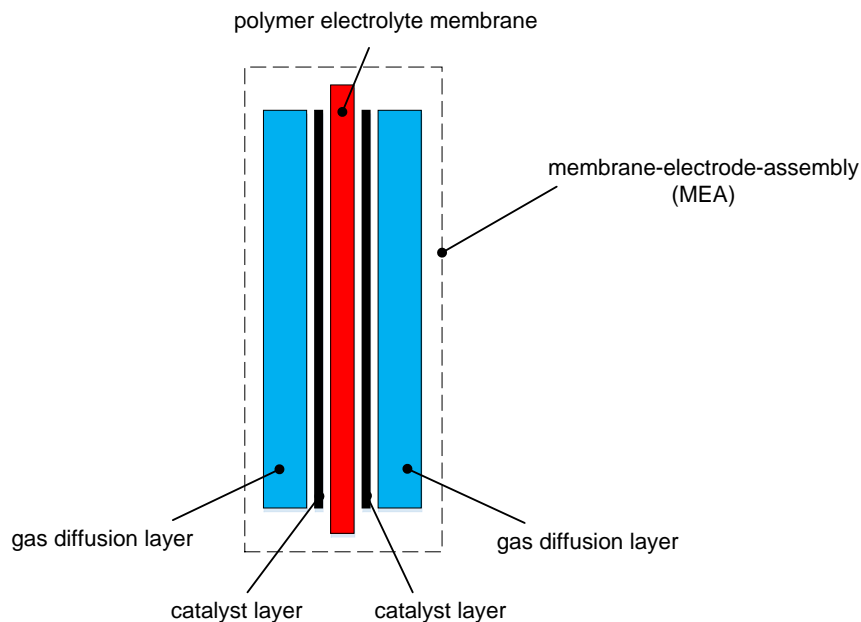The polymer-electrolyte-membrane conducts H^+-ions from the anode to the cathode. On the one hand, it acts as spatial separator. Electrons flow through the external appliance, which is powered thereby. The membranes' ability of adsorbing water is crucial for its ion transport capability. On the other hand, the PEM ensures the separation of anode and cathode space and therefore prohibits the mixing of the reaction gases. Commonly, Nafion®, a product of DuPont, is used as PEM material. It consists of a polytetrafluoroethylene-backbone with sulfonic acid groups in the side chain (-SO_3H). The sulfonic acid groups create hydrophilic cluster, which attract water and are therefore necessary for the ion conductivity through the membrane. The -SO_3H-groups can only transport H^+-ions in form of H_3O^+-ions. Therefore, the -SO_3H-groups need to be contacted to each other by means of H_2O. The thickness of a dry Nafion®-membrane is between 25 and 125 µm. In a wet state, the thickness can increase to 240% of its original size [4].

2.2.2. Catalyst Layer (CL)

The catalyst layers of anode and cathode consist of a porous structure. The catalysts are necessary to enable and enhance the respective reactions on anode and cathode. Next to their catalytic activity, the layers need to be conductive in terms of ions as well as electrons. For the cathode, it is important to have sufficient electrocatalytic activity towards the reduction of oxygen. The anode on the other hand, needs to have a high tolerance against pollution as contaminations are an issue in

the hydrogen feed and platinum catalysts suffer from poisoning in the presence of compounds such as CO. To decrease damage done by carbon monoxide, carbon dioxide or hydrogen sulfide, alloys of platinum and other noble metals are used as catalytic layer materials. These alloys are applied to a porous carbon carrier. To ensure good ion-conduction properties, up to 20 or 30 mass percent of Nafion® are processed into the catalytic layers [4]. Thus, ions generated at the catalyst layers can be conducted to the PEM more efficiently.

2.2.3. Gas Diffusion Layer (GDL)

The gas diffusion layers ensure a homogenous distribution of the reaction gases at the catalyst layers. They consist of a porous structure based on carbon. The structure creates pressure loss and therefore achieves a proper distribution of the gases across the MEA surface. However, aside from that the GDL also needs to provide electrical conductivity, give mechanical stability to the MEA and improve the water management. The structure of the GDL is crucial when it comes to removing water. It ensures that the cell is operated at optimum humidity without being flooded [10]. The diameter of the pores in the structure usually is between 10 and 30 µm. Additionally, a microporous layer is put in between the catalyst layers and the gas diffusion layer to optimize water treatment within the MEA. The pores diameter of this layer can be found between 50 nm and 5 µm [4].

2.3. Bipolar Plates

The bipolar plates are a crucial element in a PEMFC-cell and particularly within a fuel cell stack. They ensure that hydrogen and air are supplied to the MEA homogeneously. Especially for mobile applications an optimized design is important, as the main part of a fuel cell stack weight results from the bipolar plates, shown in Figure 11 [11].

**GRAPHITE BIPOLAR PLATES
TOTAL WEIGHT = 40 KG**

Bipolar Plates Electrode Membranes
Gasket End-Plate Current Collector

**COATED METAL
BIPOLAR PLATES
TOTAL WEIGHT = 24 KG**

Bipolar Plates Electrode
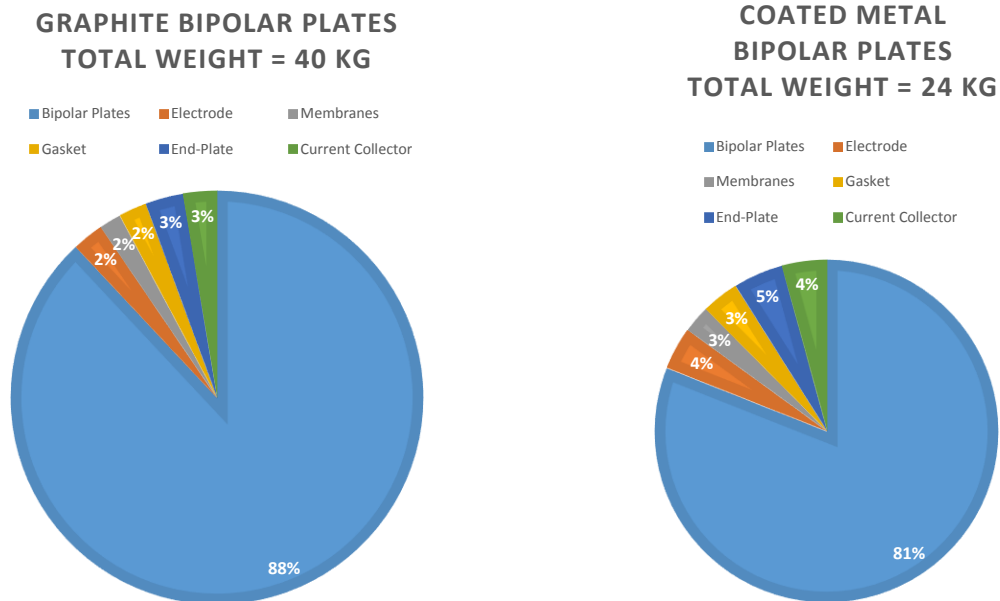Membranes Gasket
End-Plate Current Collector

Figure 11: Weight distribution of an exemplary fuel cell stack with bipolar plates milled from graphite (left) and bipolar plates deep drawn from metal sheets (right) [11].

The bipolar plates have different functions within a fuel cell: On the one hand, they provide mechanical stability of the MEA and ensure a homogenous overall distribution of reaction gases onto the MEA. On the other hand, they serve as an electrical conductor within the cell. They also need to be able to handle condensed reaction water to prohibit blocking of the channels by liquid water.

2.3.1. Manufacturing

To save money, weight and space, an optimization of the plates concerning the volume of the material is important. Therefore, the thickness of the plates should be kept smaller than 3 mm [11], if they are produced by milling, as plates made from graphite usually are. Graphite ensures a good electrical conductivity and chemical resistance, but exhibits poor mechanical properties concerning the use of a stack: it is brittle and shaping in terms of cheap mass production is difficult.

For single cell laboratory tests, milled bipolar plates made from graphite are often used. As thin and stable graphite plates cannot be manufactured, stacks exhibit bipolar plates made from steel. State of the art manufacturing is deep drawing metal sheets with a thickness in the range of 0.1 mm to 0.3 mm consisting of plated steel. The deep drawing can be realized either with one or two cavity-tools using a fluid as pressure active medium [12].

2.3.2. Functions

The primary function of the bipolar plates is to ensure the homogeneous distribution of hydrogen and air onto the MEA. This is accomplished via channel layout, through which the fluids streams run, as shown in Figure 12. The channel design is critical as it influences the distribution of the reactants and therefore has a crucial impact on the performance of a single cell. Only by optimiza-

tion of the flow field design, an increase of power density of 50 percent has been accomplished by Li and Sabir [11].

Figure 12: Concept of a bipolar plate made from thin metal sheet with flow fields on both sides. The inlet and the outlet is realized by circular holes. For both sided use additional sealing elements are required to give shape to the flow field channels next to the inlet and outlet.

The bipolar plate also represents the electrical connection between two cells within a cell. The name "bipolar plate" results from the fact, that within a stack it serves as electrical anode in one cell and as cathode in the neighbor cell [11]. So, the plate acts both as anode and cathode, even it is electrically conductive and has practically a constant potential across its thickness. For the use within a stack, sufficient conductivity for maximum efficiency is required, as the bipolar plate is the connective element between two cells. An important part of the overall-conductivity is the contact resistance between the gas diffusion layer and the bipolar plate [13]. Also the quality of the contacting surfaces and the contact pressure are crucial issues in terms of conductivity [14].

The bipolar plate is an important element creating mechanical stability within the stack. Despite of its lean design it needs to exhibit high stability within the assembled stack. It needs to be able to withstand the mechanic force required for the contact pressure to increase the electrical conductivity. All the forces resulting from the sealing pressure act on the plate [14]. The design of the plate also needs to consider that the contact pressure does not result in mechanical damages of the gas diffusion layers.

The water generated at the cathode side needs to be drained via the channels of the bipolar plate. Depending on the operation mode of the fuel cell, condensation of the water vapor might occur. This phenomenon can have a crucial impact on the function of the cell. The formation of droplets can lead to a plugging of the channels. The gas flow is blocked, resulting in an inhomogeneous distribution of the reactants, which leads to locally accelerated degradation and thus a power decrease of the cell.

The bipolar plate material has to be resistant against corrosion as next to the proton conductive membrane low pH-values of 1 to 4 occur [14]. Corrosion of the bipolar plate material can lead to the contamination of the ionomer by metal ions. This causes an increased electrolyte resistance, a decreased performance, accelerated degradation and shortens the life time of the MEA [15]. Also, passivation of the contact area between the bipolar plate and the gas diffusion layer occurs. This phenomenon leads to an increased electrical resistance and reduces the cell performance dramatically [14].

The bipolar plates are important design elements within a stack in terms of draining reaction heat effectively off the stack. On the one hand, the channels are filled with air and hydrogen rushing through the stack. When brought in with ambient temperature, they take up reaction heat and cool the stack when exiting. Using a heat management circuit and cooling with water or air as heat transfer media, the heat transition between plate and cooling medium is important and has to be maximized. This ensures to keep the heat management construction as lean as possible.

2.3.3. Flow Field Design

The flow channels usually have a rectangular cross section, particularly if the flow field is processed by milling. Channels of deep drawn metal sheets exhibit a trapeze-like cross section.

The channel width is in most cases in between 1 and 2 mm. The minimal depth is restricted by the pressure loss due to friction losses at the channel walls [11]. Higher ratios of wetted perimeter U to cross-sectional area A lead to higher friction losses per gas volume. Figure 13 depicts the flow within a rectangular cross-section of a channel.

force balance: $\Delta p \times A = U \times l \times t_w$

$\Delta p = U/A \times l \times t_w$
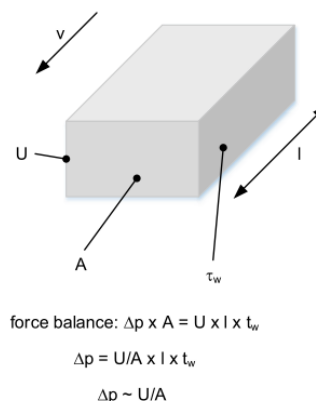
$\Delta p \sim U/A$

Figure 13: Approximation of the pressure drop in a rectangular flow field channel.

Figure 14 gives an example of two different channel geometries. Both exhibit the same cross-sectional area of A = 1 mm². However, the flat channel shown in Figure 14 left has more contacted circumference and therefore higher friction losses than the channel in Figure 14 right.

As the velocity v of the fluid remains constant, a force balance can be established: On one hand, the pressure loss Δp delivers a force when multiplied with the cross-section A. On the other hand, the wall shear force is equal to the touched area U x l multiplied with the wall shear rate τ_w. As Figure 13 shows, this balance results in the conclusion, that the pressure loss is proportional to the ratio of touched circumference U to the cross-sectional area A.

$A_1 = 1\ mm^2$

$B_1 = 4\ mm$

$H_1 = 0{,}25\ mm$

$A_2 = 1\ mm^2$

$H_2 = 1\ mm$

$B_2 = 1\ mm$

$U_1 = 2 \times (H_1 + B_1)$

$U_1 = 8{,}5\ mm$

$U_1 / A_1 = 8{,}5\ mm$

$U_2 = 2 \times (H_2 + B_2)$
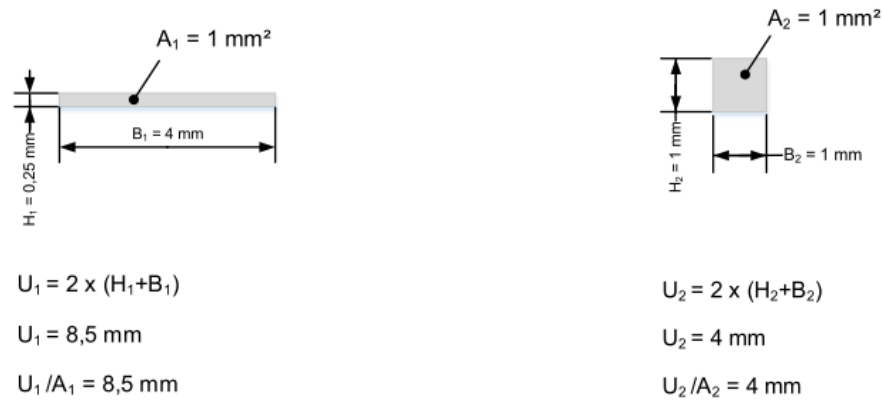
$U_2 = 4\ mm$

$U_2 / A_2 = 4\ mm$

Figure 14: A channel with a flat cross section exhibits higher friction losses than a square cross section (left). A channel with a square cross section exhibits the least friction losses of all rectangular cross sections (right).

The correlation shown above generates a conflict when deep drawing bipolar plates from metal sheets: Flat channel designs are easier to achieve from the manufacturing point of view. Deep channels require sophisticated production engineering knowledge and longtime experience. But in terms of optimized fuel cell operation they are desired.

However, simulations recommend different channel width and depth for optimized stack performance. Li and Sabir [11] conclude a depth and a width of the channels of 1.5 mm and a land width between the channels of 0.5 mm. Her, Hsieh and Chen [16] on the other hand suggest a channel to land ratio of 1 of optimum power output. Generally, the land width is on the one hand restricted by the contact pressure of the gas diffusion layer. Too high pressures can result in damaging the porous structure. On the other hand, less land width means decreased area where electrons can pass. Resulting heightened electrical resistance leads to diminished cell performance [13]. Yoon et al. [17] show, that gas diffusion generally has more impact on the power output than electric conduction. In the next step, different types of flow field design are presented and discussed concerning operational characteristics.

2.3.3.1. Pin-Type Flow Field

The pin-type design creates flow channels by using pins. Figure 15 shows a classical pattern how the pins can be arranged.
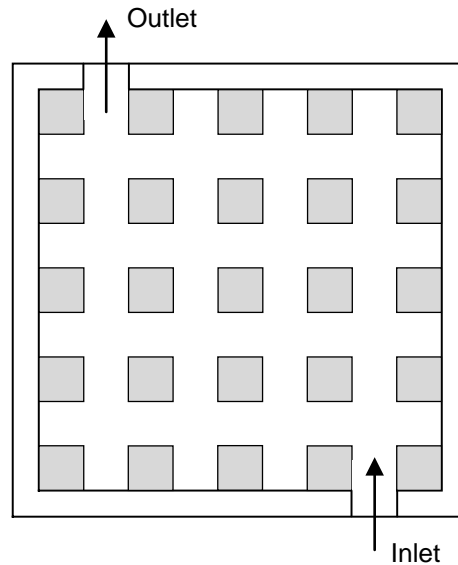
Figure 15: Pin-type flow field. The flow channels originate from utilizing small pins.

The pins generally can have any shape, but are usually manufactured with a rectangular cross section. When using this design, the flux of the reaction gases can use different ways through the flow field. According to fluid mechanical principles, the reactants choose the way of least flow resistance [18].

The present design shows small pressure losses between entry and exit of the flow field. As the fluid chooses the way of least resistance, a poor gas distribution is a characteristic of this design. Next to the creation of preferred streaming channels and resulting eddy water, agglomeration of condensed liquid water in the eddying areas can occur. Therefore, the generation of a preferred pathway is further supported, additionally leading to poor gas distribution. Aside from that, recirculation areas at the rear of each pin establish [11]. Depending on the flow regime, the pressure and therefore the concentration of reaction gas within these eddies can be reduced. At the cathode side, the recirculation areas can lead to a decreased concentration of oxygen within the eddies – the laminar recirculation can diminish the mass transport of oxygen into the eddies [19].
Isa and Aziz [13] describe the pin-type flow field as the one with the least performance density compared to straight flow field and serpentine flow field.

2.3.3.2. Straight Flow Field

Another possibility to create a flow flied is to use straight or parallel channels as pictured in Figure 16.
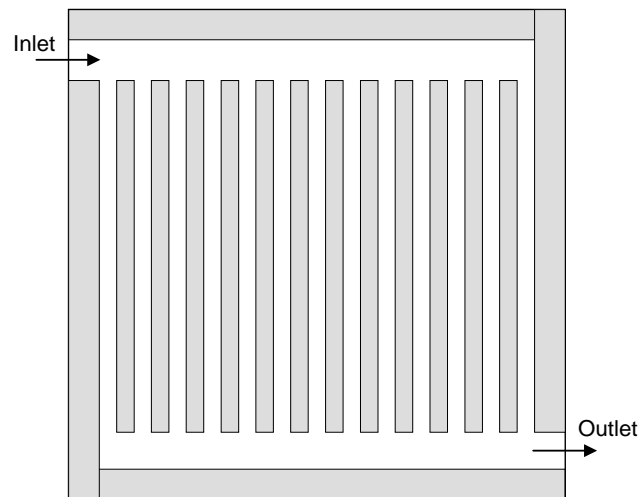
Figure 16: Straight flow field.

Li and Sabir [11] claim that this layout is prone to the formation of liquid water. This leads to blockage of single channels and thus a local of gas shortage. The reason for this phenomenon is the small pressure loss between gas entry and gas exit. The pressure loss is inadequate to purge the water, which is filling the whole cross sectional area, out of the channel. This results in the blockage of single channels. Thus, reaction gas is not supplied to the respective areas of the electrode surface anymore and therefore the cell performance decreases. To overcome this issue, the design shown subsequently gives remedy.

2.3.3.3. Serpentine Flow Field

The serpentine flow field has been developed to counteract the blockage of channels by condensed water. Li and Sabir [11] describe a design created by meanders of only one channel. Enhanced layouts use more channels to accomplish a serpentine flow field, as shown in Figure 17.
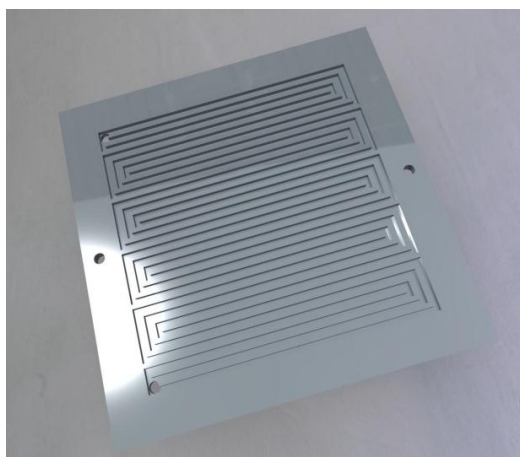

Figure 17: CAD-model of a bipolar plate with a serpentine flow field. The inlet and outlet channels are placed normally to the plate surface at the dead ends of the channels.

The advantage of this design is the high pressure loss generated by the twisted channels. They ensure that any condensed water is properly removed. Therefore, a high compressor power is es-

sential to generate the required pressure for the operation of the cell. This is a drawback in respect to the fact that the consumed compressor power can amount an considerable share of the power exit of a fuel cell stack [11]. A compromise could be a design with more than one channel, as presented in Figure 17. This leads to less compressor power required and ensures an adequate discharge of water condensed.

Examinations of Isa and Aziz [13] show that the serpentine flow field including more than one channel, as illustrated in Figure 17, exhibits the highest performance density compared to pin-type flow field and straight flow field at higher current densities.

2.3.3.4. Fine-mesh Flow Field

Recent developments on commercial automobiles driven by PEM fuel cell technology led to the invention of a fine three-dimensional structured flow field design. Contrary to the designs discussed above, this flow field does not show straight channel formations. Its appearance resembles the scaling of a fish skin. As shown in Figure 18, many small compartments exhibit openings allowing the oxygen to contact the MEA. This structure improves the water management of the MEA compared to other designs [20].
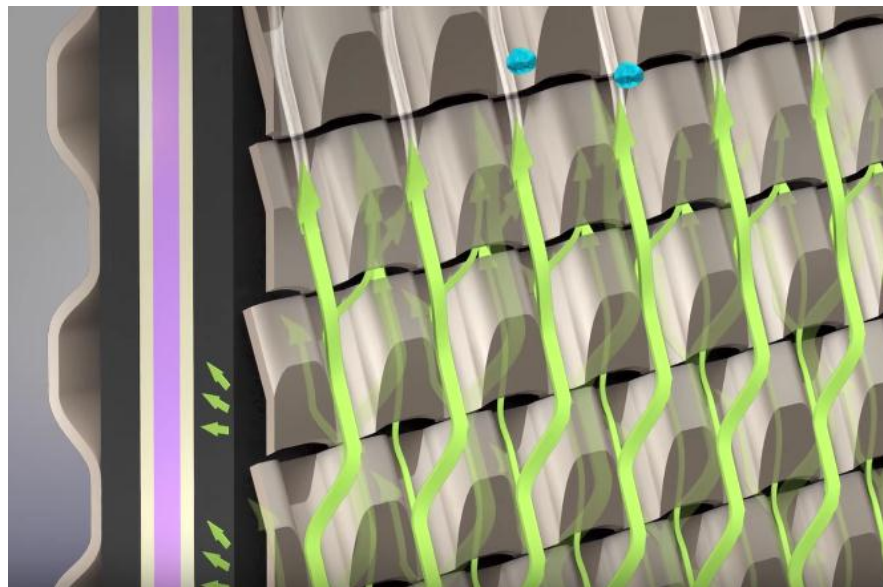

Figure 18: Fine-mesh flow field to distribute air at the cathode GDL. Local openings in the bipolar plate ensure improved water drainage. Invented and used by Toyota® to power the Mirai Model 2016 [21].

The fine-mesh flow field illustrated in Figure 18 is used by Toyota® in its fuel cell aggregate to power the Toyota Mirai Model 2016. Straight channel flow fields used within earlier models show the issue of water steam condensation and accumulation. As a result, GDL pores are blocked by liquid water. Decreased oxygen diffusion to the membrane affects power generation in a negative way [22]. Applied to the cathode side, the three-dimensional fine-mesh flow field improves the drainage of water from the MEA and the bipolar plate channel respectively. The flow conditions within the compartments draw the water from the MEA to the back side of the bipolar plate. The air stream applied takes up the water and removes it from the cell. Thus, flooding is prohibited and

uniform power generation across each cell surface is ensured as oxygen can diffuse to the membrane more effectively [22]. Additionally, the rib area contacting the GDL is decreased compared to straight channel designs. Thus, the oxygen contact area is increased improving the oxygen transport to the membrane further [23].

As discussed above, in a fuel cell stack the bipolar plate needs to fulfill several tasks. Next to reaction gas distribution it is the only element to drain reaction heat off effectively. Therefore, the next chapter presents the use of different heat management systems.

2.3.4. Heat Management

To remove heat generated during operation, a heat management system is required. It ensures that the stack can be operated at an optimum temperature. Too high temperatures can lead to damages of components as the MEA or the seals and therefore lead to malfunctions or to a shortened lifetime of fuel cell components.

Generally, two main concepts of heat management can de distinguished. Heat regulation can either take place outside the active area of the MEA or can occur across the whole active area of the MEA [24]. Figure 19 gives an overview of different heat management concepts.
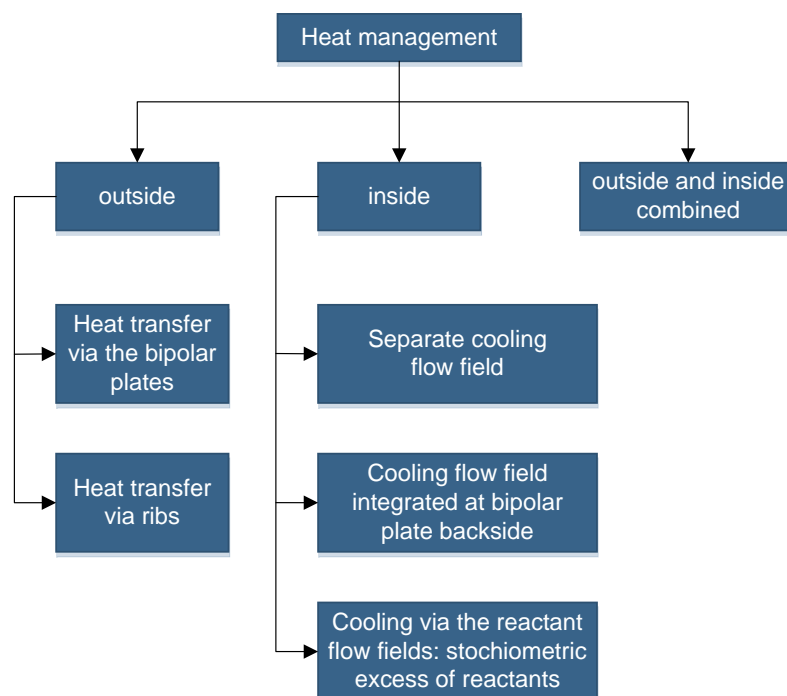

Figure 19: Concepts to realize heat management in a fuel cell stack [24].

The heat drainage outside the active area usually is realized by means of the bipolar plates, as they are the only element within a stack capable of transporting heat in a meaningful way. Firstly, the bipolar plate creates flow field channels accommodating air and hydrogen. These fluid streams

take up heat from the MEA and the bipolar plate and give it off by exiting the stack. When the gas inlet exhibits ambient temperature, a big part of the reaction heat is given off by cooling mechanism.

Secondly, if the bipolar plates ate in contact with ambient air, convection develops and the heat is removed. The surface and therefore the amount of released heat can be increased if the bipolar plates are enlarged in width [24]. This approach creates ribs which increase the area giving off heat to the environment. The merit of this design is represented by its simplicity. A disadvantage is that this system can only be used for the cooling of smaller stacks: The generated heat is proportional to the volume of the stack and the cooling power is proportional to the surface of the stack. Therefore, bigger stacks will eventually exceed their surface's natural cooling capability. Furthermore, this concept can be used only for cooling, but not for heating the stack to operation temperature before its operation starts.

To realize additional cooling channels, the design becomes more complex. The cooling usually takes place within the bipolar plate [14] or by separating a bipolar plate into two monopolar plates. At the backside of these monopolar plates, a separate flow field is engraved for the heat carrier fluid. With such a design, a better control of the temperature gradients across the active area is possible compared to cooling via the outside surface area of the stack. Also, the amount of heat removed per cell is independent of the stack size. The local temperature and the heat transfer can be regulated by the amount of cooling fluid flowing through the system. Furthermore, heated fluid can be used to heat the stack to operation temperature before the startup of the fuel cell stack [24].

2.4. Gaskets

To keep the reactants within the anode and cathode compartment, the fuel cell needs to be sealed. Failing of the sealing system leads to performance losses and safety issues. The clarification of the mechanical, thermic and chemical conditions which seals are exposed to is important [24].

2.4.1. Requirements

The sealing is required to withstand stationary operation conditions, including chemical aggressiveness and operation temperatures up to 80°C. Requirements generally are depending on the position within a stack or fuel cell, as sealing is needed for the MEA, the bipolar plate, the heat management system, the distribution channels of the reactants (for instance when using deep drawn bipolar plates with flow fields on both sides) and for the end plates. In this context, not only leaks to the environment need to be considered, but also internal leaks. Furthermore, the sealing also has to consider tolerances resulting from fuel cell component manufacturing, thermal expansion and offset caused by the fuel cell or stack design [24].

Designing the seals for the MEA needs special accurateness. Besides prohibiting leakage, it shows a defined thickness preventing the MEA from too high pressures. On the other hand, mechanical contact between the bipolar plate and the gas diffusion layer has to be ensured [24]. Therefore, the thickness of the sealing needs to be fitted to the thickness of the MEA.

If a heat management system exists, the sealing has to avoid coolant leakage to the environment but also to internal parts. The protection of the MEA is of high priority, as a contamination with the coolant fluid leads to a failure of the cell. Furthermore, the cooling circuit needs to be prevented from intrusion of materials. Ionic substances lead to an increase of the electrical conductivity of the heat transfer fluid and therefore can cause a short circuit [24]. Also, degeneration of the sealing material needs to be considered in this context.

2.4.2. Sealing Concepts

In regard to sealing concepts, one can distinguish between contacting and non-contacting methods, as well as static and dynamic concepts. In the case of a fuel cell, contacting static sealing is the only case occurring. The function of a seal relies on the fact that it plugs possible leakages, for instance scratches on the surface of adjacent elements [25].

Generally, different types of sealing concepts exist. In the chemical industry, flat gaskets are common. A lot of different materials are available. Other possibilities would be using O-rings or silk-screen-printing [24]. The last two possibilities include the sealing being fixed to the part, for instance the bipolar plate or the endplate, and cannot shift while assembling. On the other hand, such a fixing can also be achieved by using a guiding system for flat gaskets. The advantage of a flat gasket is the possibility to resolve the stack easily without destruction of any parts. In consequence, the parts can be reused again.

To seal the electrochemical cell, flat gaskets are well-established and recommended by commercial manufacturers. To seal the heat management system, flat gaskets as well as O-rings are possibilities to be used [24].

2.4.3. Materials

During the whole operation and times of standstill, the material has to preserve its physical and chemical properties. Thus, the seal is neither allowed to change its shape by swelling or shrinking, nor its hardness or composition may alter [24]. In this context, chemical decay can lead to poisoning of the MEA and therefore to a decrease of the fuel cell performance as well as destruction of the MEA.

A lot of different potentially useable materials are available. The most common sealing materials are elastomers, thermoplastics, carbon and metals.

Elastomers are very flexible, that means they are capable of prohibiting leakages at low contact pressures and at operation temperature changes. The typical installation compression of an elastomer is in between 10 and 30 percent [26]. They show good creeping behavior, but the chemical and mechanical stability is strongly depending on the type of elastomer and the working temperature.

Compared to elastomers, thermoplastics feature a poor recovery behavior concerning stress loads. They barely go back into their original shape after deformation and tend to creep strongly.

Materials made form carbon are characterized by a high chemical and thermic stability and show a good electrical and thermic conductivity [27]. However, while the conductivity in terms of temperature may be advantageous, electrical conductivity is a property not desired in a fuel cell gasket material. Metallic seals show a high affinity to corrosion and therefore are not used in fuel cell stacks [24].

Concerning the chemical stability and the material stiffness to prohibit damage to the MEA, thermoplastics such as PFA (Perfluoroalkoxy alkane), PEEK (Polyether ether ketone) and PI (Polyimide) are possible candidates for sealing materials. Comparing costs and other attributes, PFA based gaskets represent a good choice for the electrochemical cell [24].

2.5. Endplates

The endplates represent an important mechanical element of every fuel cell. Next to supporting the stack with gas connections, they also stabilize the system mechanically and have to take care of adequate contact pressure between the bipolar plates and the MEA.

2.5.1. Requirements

The performance of a fuel cell is strongly depending on the contact pressure between the bipolar plates and the gas diffusion layer of the MEA. The contact pressure is ensured by end plates and tie rods connecting them. According to Bendzulla [24], 59 % of the performance losses of a stack can origin from the contact resistance between the bipolar plates and the gas diffusion layer. Therefore, an accurate design and engineering of the endplates as well as the overall positioning system is of highest importance.

Too low contact pressure of the bipolar plates and the MEA results in leakages. Too high pressure, on the other hand, leads to the compression of the gas diffusion layer, causing a reduced flow cross-section. Thus, the flow resistance is increased locally and the gases are hindered to be distributed homogeneously across the whole active area. Hence, a contact pressure of 4-8 N/mm² is a guideline for PEMFC-systems [24].

Finally, the end plates also need to feature sufficient chemical stability against all reactants [24]. As the endplates are not allowed to deform and because of the high tensions acting on them, steel has proven as suitable material [28].

2.5.2. Concepts of Endplate Designs

The simplest shape of an end plate is achieved by using a flat plate. Alternatively, the plate can be improved with ribs to heighten the stiffness. When using ribs, it has to be taken into account that they increase the surface area emitting heat. Figure 20 gives an impression of how a rib-reinforced end plate can look like. To handle fuel cells with large active areas, curved plates can be used. These can even out the bending of the end plate resulting from the arrangement of the tie rods at the corners and the active cell elements in the middle of a fuel cell [24].
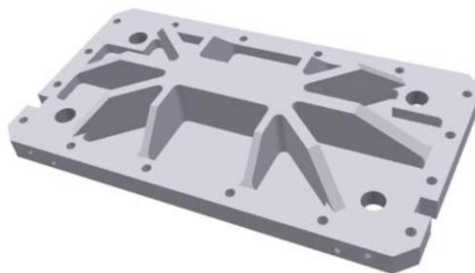
Figure 20: Rib-reinforced endplate to reduce weight but maintain stiffness [24].

The most common method to interlock a fuel cell stack is realized by using tie rods. They can be either outside the bipolar plates and the MEAs or they can go through the cell elements. If the latter is the case, and the tie rods are in contact with the cells, the rods have to be isolated to prohibit a short-circuit [24]. Figure 21 displays the function of tie rods [7]. Plate springs assure contact pressure during operation.
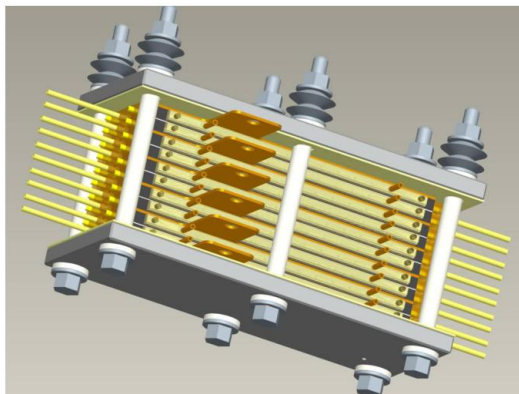

Figure 21: CAD-construction representing a PEM fuel cell stack. Tie rods and plate springs are used to ensure stability and contact pressure [7].

As shown in Figure 21, plate springs are used to balance the different heat expansion values within a stack. As the metallic tie rods show higher heat expansion than the polymeric and carbon based materials, the plate springs ensure that the contact pressure is kept constant despite heat expansion [24].

3. Theory II: Computational Fluid Dynamics – AVL FIRE

Computational Fluid Dynamics (CFD) is a tool of fluid mechanics engineering. By using numerical mathematical methods, the flow behavior is simulated. This approach allows gaining knowledge of fluid depending properties of the investigated issue in addition to laboratory examinations.

The software used in this thesis is AVL FIRE. It was developed for the simulation of fluid behavior and thermodynamic processes occurring in internal combustion engines. For this application, the modelling of two-phase mixtures plays an important role. Nowadays, additional features and modules enable the program to include other systems as well. A specific fuel cell module is integrated, allowing the software user to handle porosities, chemical reactions and electrochemical issues. The focus on multiphase mixtures is important, as the water steam in the cathode channel partially condenses, creating water droplets.

3.1. Pre-Processing

The *pre-processing* includes tasks, which precede the actual calculation of the specific simulation [29]. AVL FIRE offers the *FIRE Workflow Manager* as a graphical user interface for the pre-processing procedure and can be understood as the whole meshing process and setting up the required parameters for the calculation in the *solver-steering-file (SSF)*.

Usually, the meshing can be realized either manually using topology tools of the semi-automated *FAME Hybrid* or fully-automated by means of *FAME Advanced Hybrid*. This tool uses imported CAD-data to generate the mesh by assistance of algorithms [30].
In the case of using FAME Hybrid, AVL FIRE offers the possibility to create standard shapes by the users themselves. Cubes, hexahedrons, cylinders and other shapes can be defined in size and mesh resolution. Depending on the chosen topology, the cells have rectangular- or circle-segment-like shape.

When the shape of the mesh is more complex, for instance because of a special curvature, FAME Advanced Hybrid can be used. In the first step, a CAD-model of the desired geometry needs to be generated and exported as stereolithographic data format. Afterwards, this model can be imported into *AVL FIRE Fame Hexa*. As "Fame" means *Flexible Automated Meshing Environment*, it is a tool to automatically generate meshes usable in AVL FIRE. Hexahedron cells, as shown in Figure 22, are in terms of mathematics the optimum element to model the form of interest. Thus, AVL FIRE Fame Hexa creates computational grids by assembling as many hexahedron cells as possible [31].
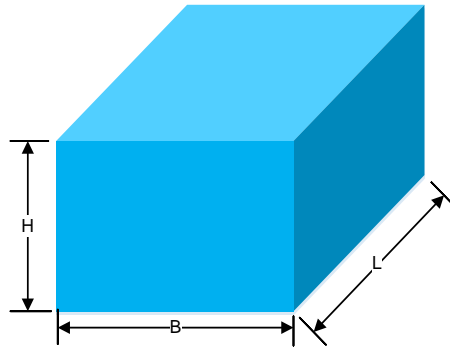
Figure 22: AVL FIRE Fame Hexa mainly uses hexahedron cells to auto-generate meshes.

Before a simulation can be realized, the mesh needs to be combined with a solver-steering-file (SSF). This file includes the simulation control settings required for the solver to run the calculation. In the subsequent chapter, the most important contents are shown to successfully run a fuel cell simulation.

3.2. FIRE-Solver

The solving process is a major part of the CFD-Simulation. By using numerical methods, the mesh characteristics are treated under the consideration of natural laws. The transport equations used for solving rest upon four conservation laws for an observed control volume [32]:

- Mass conservation, represented by the equation of continuity
- Conservation of momentum corresponding to Newton´s second law
- Conservation of angular momentum
- Energy conservation, represented by the 1st Law of Thermodynamics

To run a simulation, the generated mesh needs to be integrated into a solver-file. In FIRE, the so-called solver-steering-file (SSF) includes all information and user defined parameters to perform the numerical solution procedure. To run a fuel cell simulation, extended input information is required. When selecting the *Fuel Cell Module*, FIRE activates all necessary additional modules. Subsequent, the relevant information and additional module input is displayed.

3.2.1. Boundary Conditions

Boundary conditions represent the interface of the mesh model to its environment. All surfaces in contact to the surrounding of the mesh need to be defined. In most cases these interfaces act as spatial separations, for instance as a housing or the walls of a pipe or a vessel. To those, different properties can be attributed, for example as having a certain temperature or being adiabatic.

In most simulation cases, inlet and outlet ports are required. Like wall definition, those also need to be specified via boundary conditions. Different types of properties, for instance inlet or outlet mass flow, static pressure, fixed temperature or turbulence can be prescribed.

To attribute boundary conditions to desired faces of the mesh, *face selections* have to be defined. They represent the amount of the chosen cell surfaces. To each selection properties can be assigned to act as boundary condition.

3.2.2. Fluid Properties

The fluid represents the media whose behavior is simulated in the calculation. The mesh sections generated for simulation are filled with it. Its properties have crucial influence on the calculation of momentum and heat transfer within the model. In FIRE, different preset fluid types can be chosen. For special fluids, fluid properties, for example resulting from experiments, can be edited manually. In both cases the fluid properties are kept constant during the simulation. For selected properties, a formula input option is available to vary the fluid properties for instance in dependence of iteration number, cell center position, cell temperature or cell pressure [32].

Different fluid types may be required to model all relevant elements of a fuel cell, thus it is essential to be capable of choosing the aggregation state of the fluid. For the simulation presented in this thesis, the gaseous, the liquid and the solid state are required properties of calculated media.

3.2.3. Solver Control

FIRE can model the physics mathematically in different ways. The Solver Control defines the parameters important for the stability of the calculation and the speed of convergence. The adjustable contents [32] range from discretization control and differencing scheme to convergence criteria. Also, the nature of conservation equations to be considered in the calculation can be determined.

The option of discretization control allows the user to fit the mathematical discretization model to the mesh used within the simulation. Different approaches can be chosen depending on the quality of the cells and their surfaces to gain a good solver stability.

The equations control allows activating conservations laws for the calculation. Momentum and continuity equations provide solutions for the velocity and pressure fields. The energy equation provides solution for enthalpy corresponding values as for example temperature fields. FIRE offers different types of turbulence models to be chosen. Next to the commonly used *k-ε-model*, *PANS-*, *LES-* or *laminar* approaches, it provides the *k-ζ-f-model*. It was developed by AVL and is set as default model for simulations in FIRE. Furthermore, physical effects as viscous heating, fluid compressibility and pressure work can be selected.

In the context of the numerical solving procedure, *underrelaxation factors* can be manually edited. They ensure a limited change of variable values from the previous iteration ϕ^{k-1} to the next iteration ϕ^k. This practice secures the convergence of the solution procedure. The principle of this approach is shown in Formula 7 [32].

$$\phi^k = \phi^{k-1} + \alpha_\phi * (\phi^{new} - \phi^{k-1})$$

Formula 7: Impact of underrelaxation factors to iteration results.

In the formulation shown above, α_ϕ represents the underrelaxation factor. The actual iteration solution ϕ^{new} is reduced to a value ϕ^k as input for the next iteration step. The smaller α_ϕ is chosen, the more stable the solving procedure. On the other hand, the convergence time increases, as only small differences from one iteration to the next are realized. Large underrelaxation factors lead to strong value variations from one iteration to another and therefore can influence the solver stability in a negative way. Thus, increased oscillations can prolong the overall convergence time or can prevent reaching the desired convergence criteria at all. The ideal choice of a set of underrelaxation factors is always depending on the mesh and SSF-specifications, therefore some testing is necessary to get optimized results.

For the solution of the main conservation equations, the differencing scheme and the linear solver can be chosen. Next to classical differencing schemes as upwind or central differencing, FIRE offers special approaches as *MINMOD* or *AVL SMART*. For the linear solver, FIRE offers three options (*GSTB*, *AMG*, *CGJP*) for each equation to be solved.

A useful tool to evaluate the convergence of a calculation is to set convergence criteria. When predefined values are reached, the CFD solver assumes that steady state is achieved and thus terminates the run. On the one hand, the user can set values for minimal flow residuals to be reached; on the other hand, a maximum iteration number can be prescribed. If the calculation accomplishes these values, the simulation stops. Anyway, it is still the user´s responsibility to judge if the convergence state of a simulation is satisfactory or not [32]. For this task, further tools as the 2D-Log or post processing of 3D results can be included.

3.2.4. Multiphase

Wallis [33] defines a multiphase flow as "...the simultaneous flow of several phases. Two-phase flow is the simplest case of multiphase flow". For the simulation of a fuel cell, FIRE needs to simulate the interaction of different phases. By using the *Euler-Euler-Approach*, for each phase a private velocity and turbulence solution can be received. Only the pressure equation is shared by all phases [34]. The multiphase module allows the user to define different phases being considered in the calculation.

Concerning fuel cells, the multiphase modelling is of special interest regarding their characteristics: On the one hand, the GDL of the MEA consist of a porous solid structure. FIRE can model these parts by implementing a solid phase with the property of being porous.

On the other hand, water generated at the cathode needs to be drained via the channel. By the electrochemical conversion of hydrogen and oxygen, water is produced. PEM fuel cells have operation temperatures typically ranging from 60 °C to 80 °C. The higher the electrical load applied, the more gaseous water is generated. This can eventually exceed the saturation pressure and therefore cause the condensation of water droplets. This two-phase flow exiting the cathode channel needs to be modelled by using the multiphase module too.

3.2.5. Porosities

Porous media are often used in technical applications. Their purpose is usually either to generate a huge surface area, for instance in catalysts, or to achieve a uniform velocity distribution as the GDL in a fuel cell does. These fine-scaled geometrical structures can be barely realized by generating an extra fine resolution of the geometrical mesh. Such an approach would lead to unreasonable mesh resolutions and calculation time. In FIRE, a porous media is simulated by utilizing additional flow resistance to the specified area. This is achieved by adding a momentum sink to the governing conservation equations. To do so, FIRE offers several different flow resistance models as for example *Forchheimer*, *Carman-Kozeny* or *Tube friction* [35].

To ascribe porous properties to a selected region, a *cell selection* needs to be defined. This selection has to include all cells, which should act as porous media.

3.2.6. Species Transport

The Species Transport Module allows the solver to consider stoichiometric reaction balances of chemical species. For the application of a fuel cell, the multi component diffusion is of special interest. The physically correct description ensures that mixtures consisting of more than two chemical components are bound to conserve mass species [36]. This can be achieved by using the *Maxwell-Stefan-Equation* for ideal gases and liquids. Diffusion coefficients put into account are calculated for each species depending on its concentration.

3.2.7. Electromagnetics

For the simulation of a fuel cell, electromagnetic effects have to be considered. Especially the calculation of electric fields and ohmic heating is of interest. The latter is resulting from current flux and ohmic resistance within the bipolar plates, the GDL and the catalyst layers. Furthermore FIRE is capable of calculating ionic fields and ohmic heating in the electrolyte as well as magnetic fields in and around the fuel cell [37]. Thus, the electrical current loading can be determined in dependence of a predefined electrical potential between anode and cathode.

3.3. Post-Processing

To analyze the results of a numerical simulation, FIRE includes a post-processing unit called *IM-PRESS*. It allows the user to animate the results received in different ways. For steady state simulations, the results displayed correspond to a specific iteration number. Required information is stored in a file and can be loaded into the Workflow Manager when the simulation is finished [38].

The main application of IMPRESS is to generate two-dimensional cuts of the simulation results, as shown in Figure 23. Cuts can be realized in x-, y-, and z-direction and be placed to desired coordinate values. Different attributes can be ascribed to the cut to be displayed, for instance absolute or dynamic pressure or velocities in each coordinate direction. The attributes can be presented in different ways, for example as scalar values or as lines of identical value (isolines).
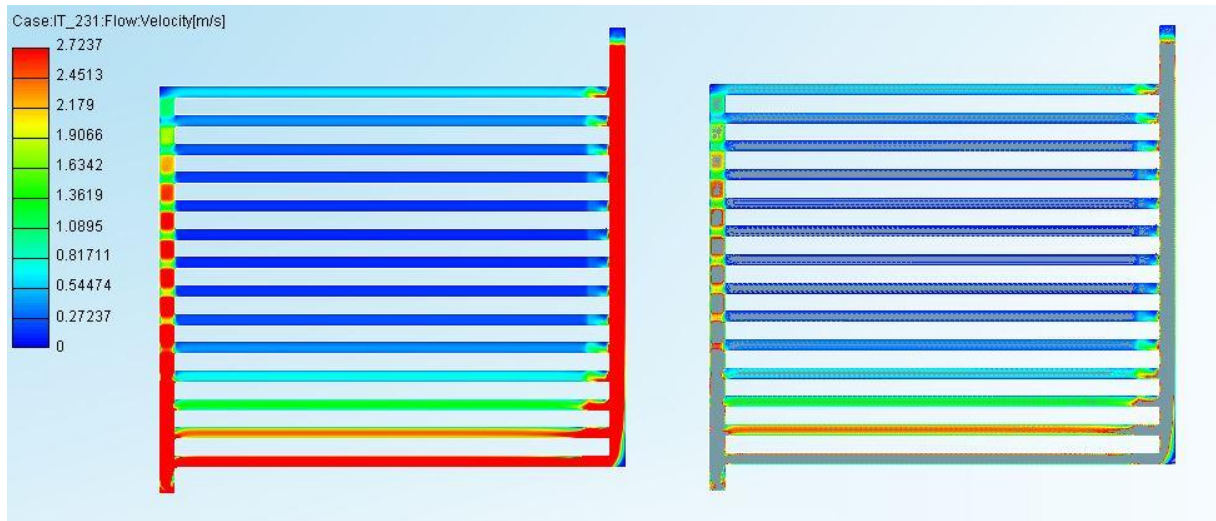
Figure 23: Post-processed image of the bipolar plate channel shown in Figure 12. The velocity in the channel can be displayed as scalar values of the cells (left) or as isolines of constant velocity (right).

As shown in chapter 3.1, the simulation procedure is based on the pre-processing of the mesh. The following chapter describes the experimental approach used in this thesis to model the investigated fuel cell. Besides the experimental proceeding, special focus is put on the generation of the mesh, including geometrical requirements and meshing strategy.

4. Experimental: Simulation of Fuel Cell Operation

To design a fuel cell, it is important to have sufficient understanding of its operation behavior. By using a computer based simulation, conditions during operation can be reproduced. Thus, a simulation is a designing tool to improve the efficiency of the eventual product on the one hand. On the other hand, it allows gaining knowledge of the physics underlying.

4.1. Goals

Within this thesis, the physics during the operation of a single cell, as shown in Figure 24, is examined. In the context of optimized operation behavior, the understanding of fluid and electromagnetic phenomena is necessary. To have a look inside a fuel cell, a simulation containing fluid dynamics, reaction behavior and electromagnetic effects is a proper way to gain knowledge of general physical correlations. In this context, the bipolar plate represents a crucial element. As it is responsible for the distribution of hydrogen and oxygen across the membrane, it determines the local efficiency of the electrochemical reaction and therefore influences the overall efficiency of a fuel cell strongly.
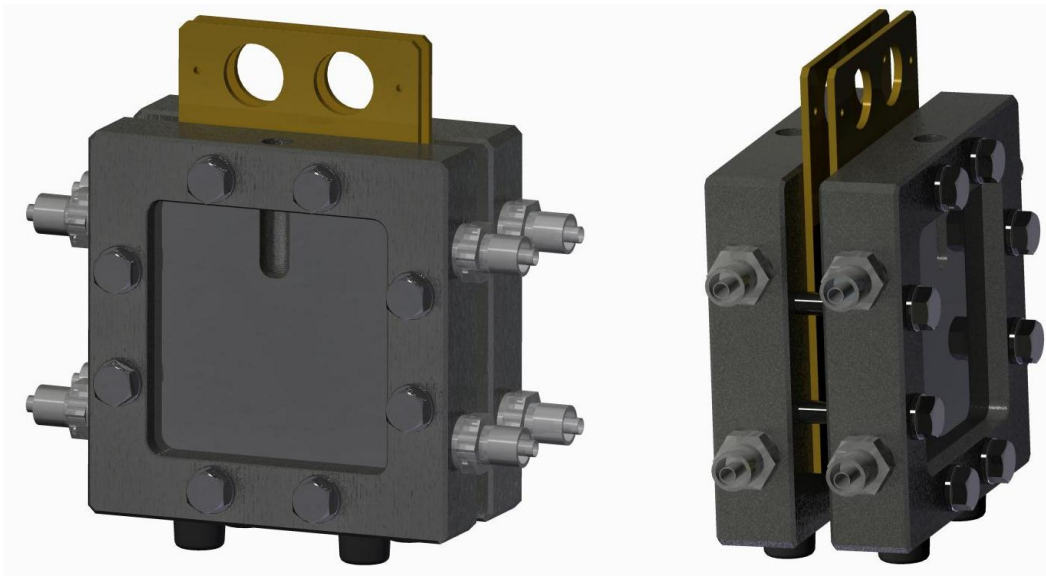
Figure 24: CAD-model of the examined fuel cell.

The cell shown in Figure 24 is a single cell used for laboratory testing of MEAs regarding material degradation. The endplates and the screws are responsible for the mechanical stability of the unit. The endplates feature four connection pins each for gas in- and outlet. The current collectors are coated with gold to keep electric losses low and prohibit corrosion.

To simulate the single cell shown, the software AVL FIRE is used. Its characteristics are discussed in chapter 3. To get a basic understanding of the experimental proceeding, the following chapter is concerned with the operational settings of the fuel cell observed.

4.2. Approach and Operational Settings

To examine the usability of simulation tools for fuel cells, this thesis compares the results of a CFD-simulation with experimental results.

As laboratory tests for the examined fuel cell have been done before, the required infrastructure is available. The main challenge is to generate a CFD-model and reproduce the operation behavior of the fuel cell shown in Figure 24. The overall operation conditions for current performance comparison are shown in Table 1. Continuative investigations concerning spatial distributions of in-cell characteristics refer to different operations conditions shown in Table 15.

Type of fuel cell	PEMFC
Active area	50 mm x 50 mm
Bipolar plate type	Milled from graphite plate
Cell operation temperature	70 °C
Cell operation pressure	1 atm
Anode feed	Hydrogen
Cathode feed	Synthetic air

Table 1: General operation information of the examined fuel cell.

As a PEMFC fuel cell is investigated, it is fed with hydrogen and air. The operation temperature is set to 70 °C whilst the operation pressure is kept at 1 bar. The active area exhibiting 50 mm x 50 mm is obtained by using bipolar plates manufactured from graphite plates.

The following chapters show operation characteristics set fixed for laboratory and computational investigations before any of them is conducted. By using this approach, a proper comparison of both proceedings is ensured.

4.2.1. Inlet Volume Flows

The inlet volume flows on anode and cathode, respectively, represent an important operation condition. These values are considered within the laboratory and the computational examinations both. Table 2 shows the inlet volume flows for anode and cathode. The anode inlet consists of pure hydrogen while the cathode inlet is made of 79 mol% N_2 and 21 mol% O_2. The experiments in the laboratory are conducted with synthetic air exhibiting the composition shown in Table 2.

	Anode	Cathode
Inlet volume flow / Nml min^{-1}	500	1000
Mole fraction H$_2$	1	0
Mole fraction N$_2$	0	0.79
Mole fraction O$_2$	0	0.21

Table 2: Characterization of the inlet volume flows.

Furthermore, the relationship of both inlet flows concerning the flow direction is predefined. The flow fields used for the investigation exhibit overlapping inlet and outlet openings. Also, the flow fields themselves are geometrically symmetric in terms of channel arrangement. Thus, the inlet and outlet tubes can be placed and inverted independently of geometrical restrictions. If the inlet of the anode channels and the inlet of the cathode channels are abreast, a co-flow is at hand: Both gas flows are in the same direction. If the inlet and outlet of either anode or cathode are swapped, hydrogen and oxygen run a contrary route. This operation condition is called counter current flow.
For the investigation and comparison treated within this thesis the fuel cell is operated in co-current flow.

4.2.2. Temperature Conditions

In addition, it is required to highlight the temperature conditions of the examined cell. To enable a stable operation, the cell is kept at fixed temperatures by means of electrical heating elements. During stationary operation realized within laboratory investigation, the cell itself is held at a temperature of 70° C. The inlet mass flows of anode and cathode channel exhibit 5° C higher temperature than the cell itself. This proceeding helps to ensure that the inlet streams possessing high loadings of gaseous water are held above the dew point. The heightened temperature prohibits condensation due to inhomogeneous temperature conditions along the route to the inside of the cell. Table 3 shows the temperature conditions discussed above as well as the humidification of the inlet flows.

	Temperature	Relative humidity
Cell inside	343 K	-
Inlet flows	348 K	0.9 (at 343 K)

Table 3: Temperature conditions of the examined cell. For input in FIRE, the temperature needs to be known in Kelvin. For the humidification of the membrane, the inlet flows exhibit a relative humidity of 0.9 referring to the cell inside temperature of 343 K.

Based on the operation information shown above, laboratory and CFD investigation can be conducted. Firstly, proceedings concerning laboratory examination are discussed; secondly the CFD approach is illustrated.

4.3. Laboratory Examination

Within laboratory examination, the cell is investigated using an existing test stand. At first, the single cell needs to be assembled, especially in terms of the MEA. Subsequently, the cell is installed in the test rig and the operational settings are adjusted. Based upon these preparations, the investigations concerning current and voltage characteristics can be realized.

4.3.1. Preparation

To examine the fuel cell, it needs to be assembled at first. To get the cell ready for the experiments, all parts have to be arranged in the right way. A critical procedure is the assembling of the MEA and its sealing. For the experiments shown within this thesis, a *catalyst-coated membrane* (CCM) is used. Thus, the proceeding is facilitated as the membrane layer already includes the cathode and anode catalyst layer and only the GDLs including a microporous layer need to be mounted upon it. The GDLs themselves are made of carbon paper to ensure a homogeneous gas distribution at the catalyst layers. On one side, the carbon paper is coated with carbon particles mixed with PTFE for water removal next to the catalysts. To seal the fuel cell from the environment, flat gaskets are used. Next to their sealing function, they have to even out the thickness of the MEA and take up excessive compression force. A picture of the sealing is displayed in Figure 25.
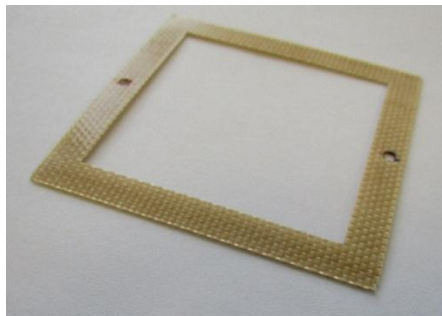
Figure 25: Picture of the sealing used in the laboratory fuel cell investigation. For anode and cathode side a separate sealing is used. The holes are required for proper positioning in the cell.

The types of membrane, GDLs and gasket can be found in Table 4. Furthermore, the thickness characteristics are shown.

Component	Type	Thickness / μm
Membrane	QuinTech CCM-H25-N212	50
Gas diffusion layer	SIGRACET® Gas Diffusion Media, Type GDL 35 BC	325
Gasket	PTFE textile flat gasket	300

Table 4: Characteristics of the MEA components and gasket.

To ensure optimal contact pressure, the endplates of the cell are connected with eight screws of type M6, as visible in Figure 26. Each of them is tightened with a torque of $T_s = 2$ Nm. According to

Formula 8 [39], this torque appliance equals a force triggered by each screw of F_{screw} = 2037.28 N. Eight screws result in a total compression force of F_{com} = 16298.24 N.

$$F_{screw} = \frac{T_s}{d_2/_2 * \tan(\alpha + \rho') + \mu_A * 0.7 * d}$$

Formula 8: Calculation of the axial screw force F_{screw} resulting from applied torque T_s. For M6, the nominal thread diameter d = 6 mm, the effective diameter d_2 = 5.35 mm, the angle of elevation α = 3.4°, the friction angle at the thread ρ' = 9° and the coefficient of sliding friction at the screw head surface μ_A = 0.1 are required for calculation [39].

Assuming a homogeneous pressure distribution on MEA and gasket, the concerned surface area can be evaluated by means of a CAD-model of the flow field. Considering the lands, the flow field shows a contacting area of 1206.11 mm². Furthermore, the contact area of the flat gasket has to be taken into account. It adds further 1589.72 mm² to the overall contact surface area. Therefore, the contacted compression surface area equals A_{com} = 2795.83 mm². Considering Formula 9, the contact pressure of MEA and sealing can be calculated to 5.83 N/mm². The received result is in between the recommended boundary values for the MEA contact pressure, which are given to be between 4 and 8 N/mm² [24], as shown in chapter 2.5.

$$p_{con} = \frac{F_{com}}{A_{com}}$$

Formula 9: The contact pressure p_{con} is calculated by the ratio of the force F_{com} acting on a defined compression surface area A_{com}.

To conduct experiments, the assembled fuel cell as shown in Figure 26 is installed in a test rig [7]. It is required to connect the inlet and outlet nozzles of the fuel cell to the gas feed and exit tubes of the test stand. To keep the operational temperature at the defined level, the regulation of the fuel cell heating needs to be ensured. This requirement is met by using thermocouples and electrical heating elements integrated into the endplates. Furthermore, the current collector plates need to be connected to a potentiostat in order to be able to apply an electrical load. Figure 26 shows the final setup in the test rig used for conducting the experiments.
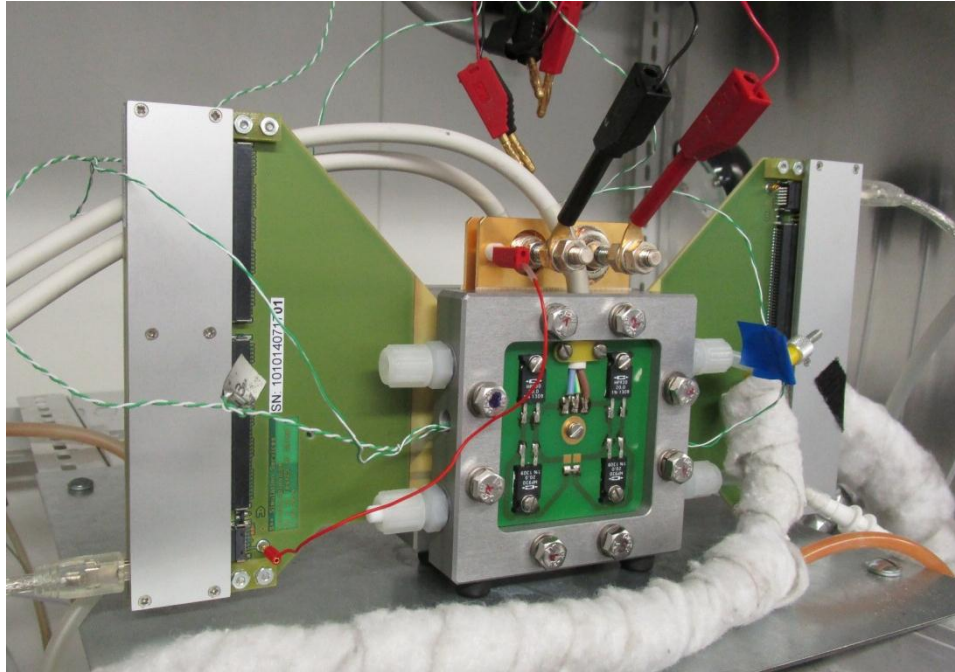
Figure 26: Picture of the examined single cell installed in the test rig. The wing-like extensions belong to a segmented current scan shunt device (S++ Simulation Services, Germany). The supply channels are insulated and additionally heated with pipes including heating media to prohibit condensation of water vapor within the gas supply pipes.

To operate the cell with feed streams with a relative humidity of φ = 0.9 referred to the cell inside temperature, the inlet gas needs to be humidified. This is realized by a bubble column filled with water. By rising from the column bottom to its top, the anode and cathode gases take up water until they reach saturation. To gain the desired humidification inside the cell, the temperature of the bubble columns need to be adjusted correctly. Therefore, the partial vapor pressure p_v for a relative humidity φ = 0.9 referred to the cell inside temperature needs to be calculated. Subsequent, the saturation temperature for p_v can be recalculated to heat the bubble columns by using literature values [40]. To do so, the relationship of partial vapor pressure p_v and saturation vapor pressure p_v', shown in Formula 10, needs to be considered.

$$\varphi = \frac{p_v}{p_v'}$$

Formula 10: The relative humidity represents the ratio of partial vapor pressure to saturation vapor pressure.

Table 5 shows intermediates and results of the calculation proceeding.

Temperature / °C	Relative humidity	vapor pressure p_v / mbar
70	0.9	280.59
67.53	1	280.59

Table 5: The bubble columns of the test rig need to exhibit a water temperature of 67.53 °C to reach a relative humidity of 0.9 at 70 °C cell temperature.

Before experimental measurements can be conducted, the MEA has to undergo activation. This step is required to achieve a steady state within the MEA in terms of water distribution. Therefore,

the cell is operated at a point of constant current. During this phase, usually a rise of the cell performance can be observed, as the conductivity of the membrane increases due to heightened water saturation. For the present experiments, the activation phase was realized by operating the fuel cell overnight at a constant current of 7.5 A. The cell used for temperature and current density distribution comparison was activated overnight at 12.5 A.

4.3.2. Experiments

Initially, working points to be observed are determined. This is achieved by a given voltage-time curve, controlled via potentiostat. The current response is recorded at given voltages. This approach is realized by a regulation loop: The current load applied by the potentiostat is adjusted until the desired voltage output is reached. Figure 27 shows the predefined voltage-time curve used to conduct laboratory examination.
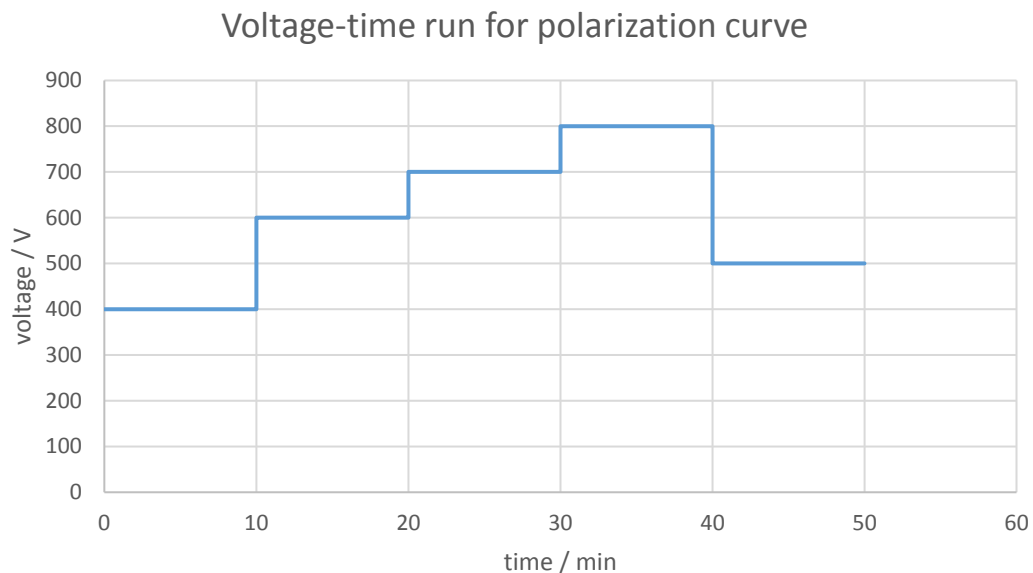
Figure 27: To record voltage-current values, the shown voltage curve is applied. To ensure steady state, the voltage values are held for ten minutes each.

Furthermore, a segmented current scan shunt is used to observe the temperature and current density distribution. The current scan shunt device (S++ Simulation Service, Germany) is placed between cathode flow field and cathode current collector. It consists of 5x5 segments for local temperature measurement and 10x10 segments for local current density measurement. By means of two USB-connections, it records the temperature and current density behavior at pre-determined time intervals.

Based on the laboratory settings discussed above, the experimental approach of the CFD simulation to be compared is shown. The next chapter illustrates these computational proceedings.

4.4. Computational Fluid Dynamics

To reproduce laboratory investigation results, a computational fluid dynamics model is generated in AVL FIRE. The composition and the operational settings are defined. The following chapter discusses the main issues concerning the experimental simulation procedure. Extensive information regarding the mesh assembly as well as the solver settings can be found in the Appendix (Table 21 to Table 44 and Figure 50 to Figure 56).

4.4.1. Mesh

To simulate the operation behavior of the fuel cell shown in Figure 24 by means of AVL FIRE, a functional mesh needs to be generated. The mesh includes all parts of the cell where functionalities of the fuel cell are to be determined in the simulation. Therefore, the mesh stakes off the geometrical region where observations can be made. Furthermore, the mesh needs to be able to simulate all essential functions of the fuel cell to ensure that all physical, chemical and electrical effects are included in the simulation to model real operation conditions as exactly as possible. In this context, it is important to be reconsidering the fact that a computational model is an attempt to reproduce the reality without being able to claim copying it exactly. As not all factors of reality can be captured, assumptions must be made for a simplified model.

4.4.1.1. Geometry Requirements

The geometry of the mesh is primarily defined by the geometry of the bipolar plate, shown in Figure 28. The flow field is of serpentine type with 3 parallel channels. The inlet and outlet is realized via holes pierced through the bipolar plate. The channels show a width of 0.85 mm and a depth of 1 mm. The in- and outlet holes exhibit a diameter of 2 mm. The resulting active area, being in contact to the MEA, is 50 mm x 50 mm.
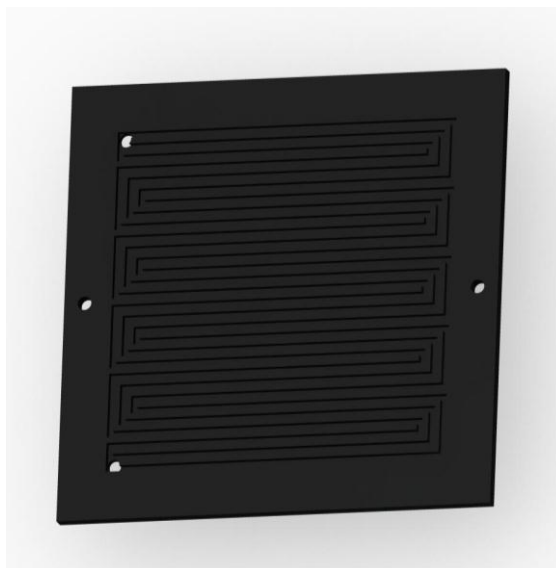
Figure 28: Model of the graphitic bipolar plate used in the fuel cell shown in Figure 24. The inlet and outlet holes have a diameter of 2 mm. Next to the flow field, drillings for the aligning systems can be seen.

To simulate the operation behavior of the cell, the bipolar plate serves as a template to generate the mesh used in AVL FIRE. Available CAD data allows extracting the channel geometry from the bipolar plate model shown in Figure 28. The resulting channel geometry is shown in Figure 29. The ports for hydrogen and air are of cylindrical shape with a height of 8 mm. This results from the fact, that they do not only go through the bipolar plate but also enter the endplates, as shown in Figure 24.
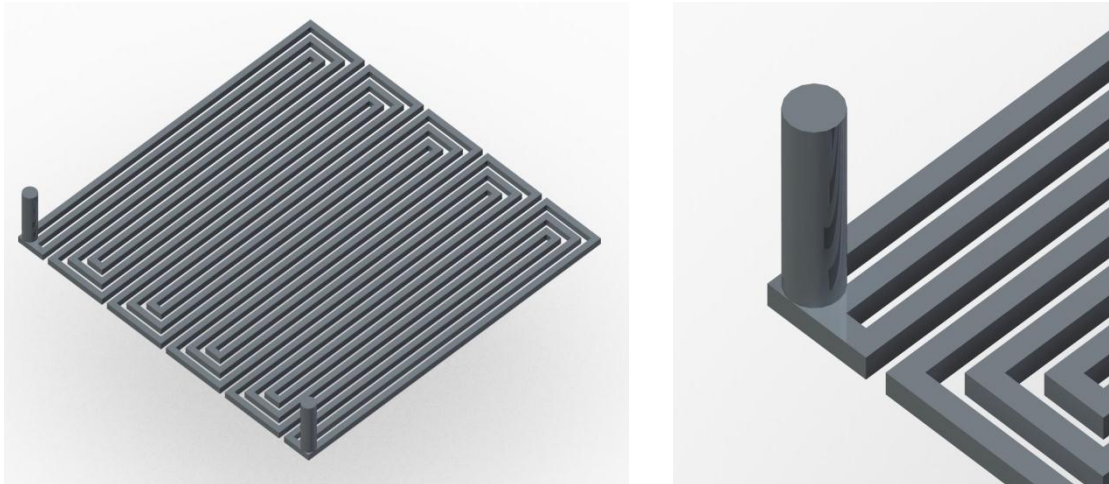
Figure 29: Channel geometry of the bipolar plate shown in Figure 28 (left). The ports for in- and outlet of the gas are modelled as cylinders (right).

The MEA is another crucial part of the simulation and exhibits a total thickness of 700 μm. Within it, the membrane has a thickness of 50 μm and the GDLs 325 μm each. Figure 30 gives an impression of the MEA.
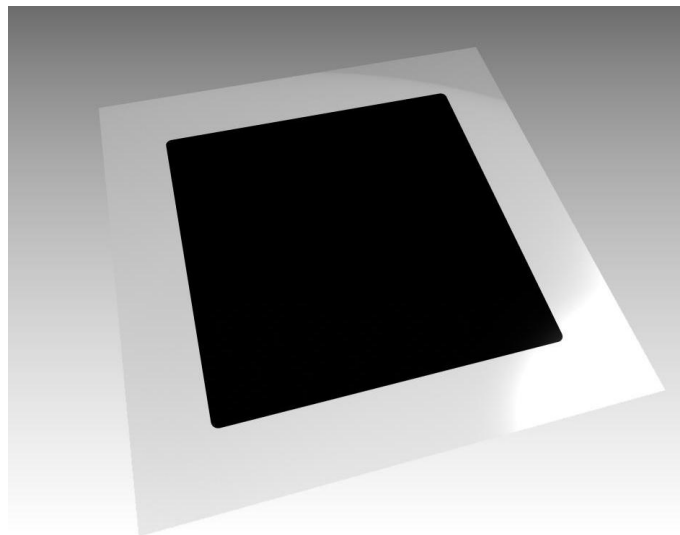
Figure 30: Illustration of the MEA. The membrane is transparent and exceeds the GDL dimensions. The active surface area shows 50 mm x 50 mm and fits the channel geometry precisely.

The geometries shown above contain the basic information to generate a mesh in FIRE. Subsequent the strategy of the meshing process is described. Next to the composition, also the procedure of the meshing is described.

4.4.1.2. Meshing Strategy

To generate the mesh for fuel cell simulation, FAME Hybrid is used. Because of meshing restrictions shown underneath, available CAD data cannot be used to auto-generate the whole mesh or selected parts via FAME Hybrid Advanced. Thus, Topology Meshing Tools of FAME Hybrid are used.

The final mesh consists of three main parts: anode channel, cathode channel and MEA. At the end of this chapter the joining of these elements to the final single cell model is illustrated. The whole meshing process is obliged to some restrictions. They are discussed subsequently and influence the described procedure profoundly.

Meshing Restrictions

When generating the mesh for the single cell simulation, several restrictions have to be considered. As shown subsequent, they influence the meshing strategy as well as the calculation process noteworthy.

1.) For simulation, the Institute of Chemical Engineering and Environmental Technology requires to use an exact copy of the channel geometry as shown in Figure 29. This requirement leads to a maximum cell width of 0.05 mm in two dimensions within the channel mesh.

2.) AVL FIRE´s Fuel Cell Module requires special mesh connections between flow field channel and GDL. It is necessary to connect these parts with a *conform connection* (N. Kosir, personal communication, 26.07.16). Therefore, the cell sizes of the channel mesh and GDL mesh have to exhibit exactly the same size.

3.) AVL FIRE´s tool A*rbitrary Connect* allows connecting faces with unequal mesh shapes and sizes. It is necessary to join the in- an outlet channels to the single cell mesh with this type of connection. It is also helpful to locally increase the cell size to keep the overall cell number low. However, using the "conform connect" command destroys existing arbitrary connections unrecoverable (N. Kosir, personal communication, 12.08.16). Therefore, all arbitrary connections have to be set after the "conform connect" command. This aspect influences the meshing procedure essentially.

Anode and Cathode Channel

The mesh for anode and cathode channel is assembled by using different rectangular elements, as shown in Figure 31. The elements are put into position by using a translation command and joined to a mesh by using the "conform connect" command. As anode and cathode channels exhibit the same geometry, the channel mesh has to be generated only once.
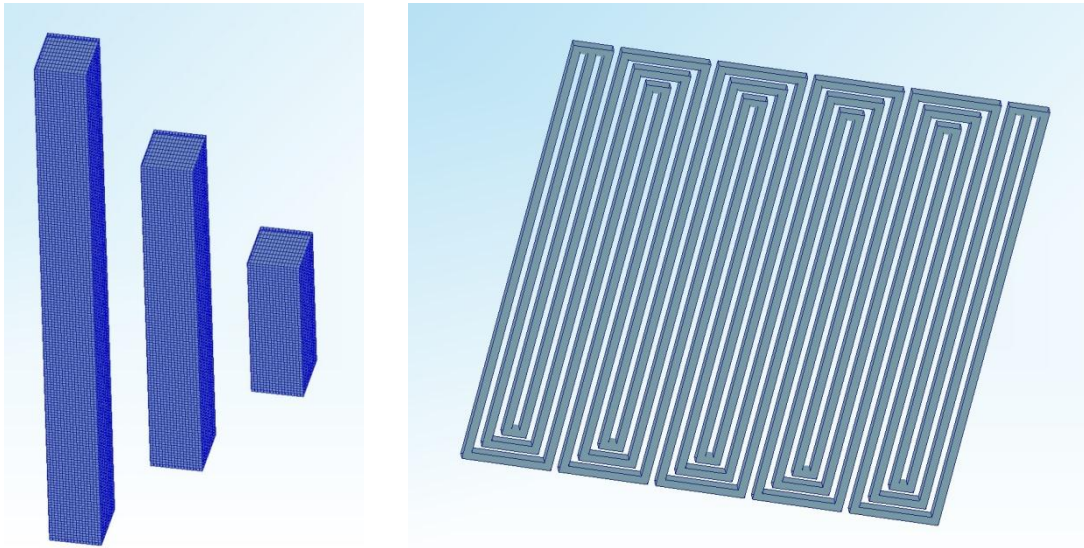
Figure 31: The channel mesh is created by using rectangular elements composed of hexahedron cells (left). The elements are joined together creating the channel geometry (right).

As discussed in the meshing restrictions section above, the geometry of the channel mesh has to fit the geometry of the CAD-model exactly. The channel exhibits a width of 0.85 mm. Therefore, the cell width and depth is restricted to a maximum size of 0.05 mm. To keep the cell number as low as possible, the cell width and depth are set to said value of 0.05 mm. As the cell height is independent of the channel width, it is set to larger values. Practical, a non-uniform distribution via the channel height is realized. The channel height is divided into six cell layers with diminishing cell height in direction to the channel bottom and top. This is realized by the command *Redimension* using a compression factor of 2.5 and choosing the toggle for symmetric distribution. This way, the cell number can be kept low without exceeding the maximum recommended cell aspect ratio of ten [30]. The resulting cell distribution via the channel height is illustrated in Figure 32.
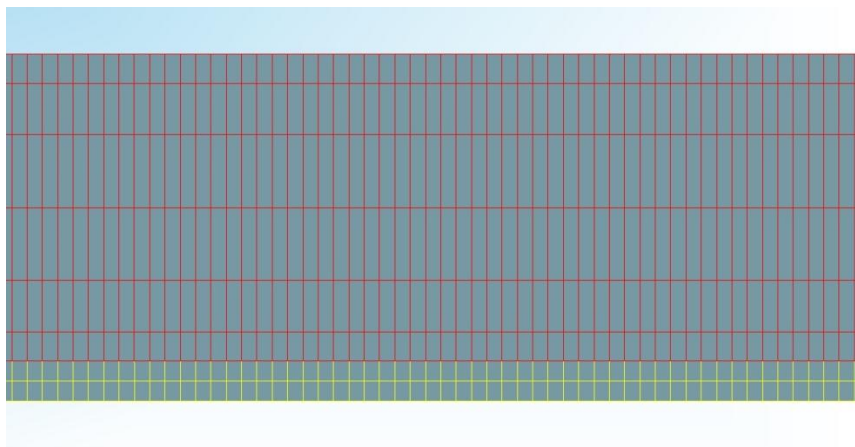
Figure 32: Each channel mesh (red) has to be connected with its intended GDL (yellow) conformal.

Membrane-Electrode-Assembly

The MEA consists of the membrane, the anode GDL and the cathode GDL. As mentioned above, the GDL needs to exhibit the same cell distribution at the interface of the channel as the channel mesh itself. The membrane can have a lower resolution, as it is not in contact with the channel mesh. Thus, the arbitrary connect command can be used. Therefore, the cell width can be enlarged within the MEA to reduce the overall cell number. To realize such a cell distribution, the MEA has to be put together by different layers. Figure 33 gives an impression of the MEA composition.
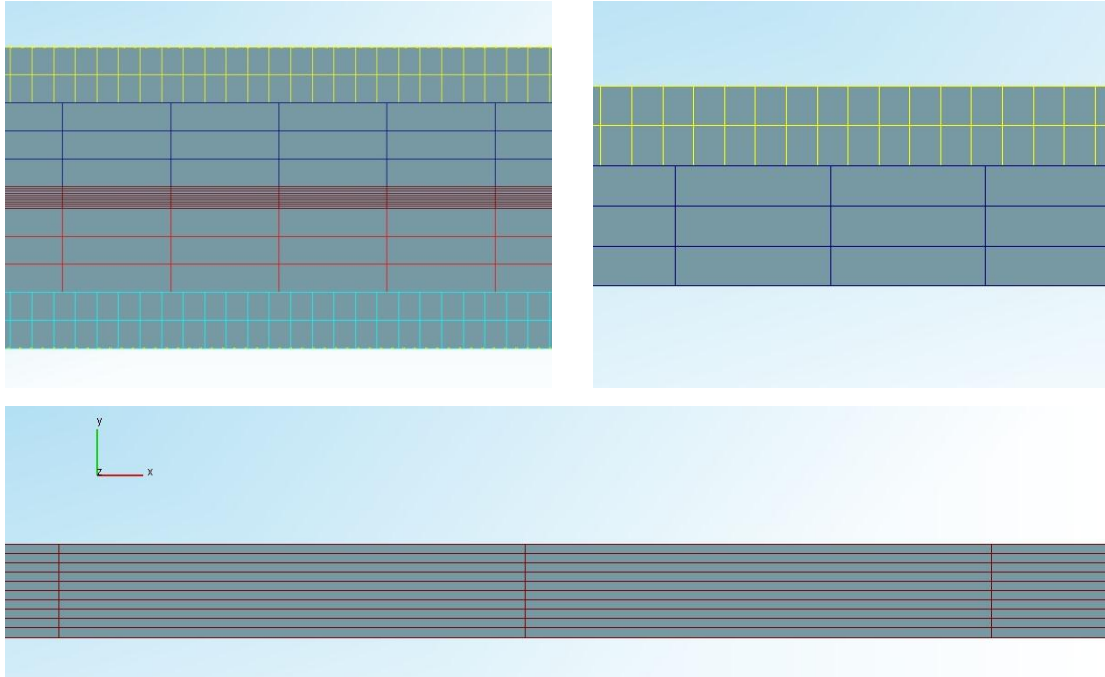
Figure 33: The MEA-mesh consists of five layers (top left). The cathode GDL (top right) as well as the anode GDL are made up of two different layers each, connected by arbitrary connect. This allows the membrane (bottom) to manifest a lower cell resolution in x- and z-direction.

The MEA, as shown in Figure 33 top left, consists of anode GDL, cathode GDL and membrane. In direction of its thickness, the GDL features five cell layers [41], as shown in Figure 33 top right. The two outer layers of the GDL consist of a mesh conform to the channel mesh. The inner three layers of the GDL exhibit the same cell width as membrane. The catalyst layers, as well as the microporous layers, are not modelled by means of a geometrical mesh. They are represented by the interface between the GDL and the membrane. The membrane itself shows ten layers in y-direction [41], as shown in Figure 33 bottom.

As discussed above, the sequence of joining the different elements together to a single mesh is of high importance. Therefore, the next section focuses on this topic in regard to the present fuel cell model.

Connection to Single Cell

To successfully join the MEA, the anode and the cathode channel to a single cell mesh, it is important to execute the two different types of connections in the right sequence. As mentioned above, conform connections have to be done before arbitrary connections. That means that the GDL, consisting of two meshes with different size distribution as shown in Figure 33 top right, is not allowed to be connected via arbitrary connect at initially. Therefore, the anode and the cathode channel have to be connected conformal with the outer layers of the GDL, as shown in Figure 32.

Subsequent, the remaining arbitrary connections can be performed. The residual layers of the anode and cathode GDL can be joined, as shown in Figure 33 top right and the four inlet tubes can be meshed and joined to the channel mesh. Their purpose is to allow the flow pattern to be simulated in a manner closer to real operation before the gas enters the channels. This leads to a more realistic model. These tubes are generated via Topology Tools as cylinders and joined to the mesh by means of arbitrary connect command. The final single cell mesh is shown in Figure 34.

.
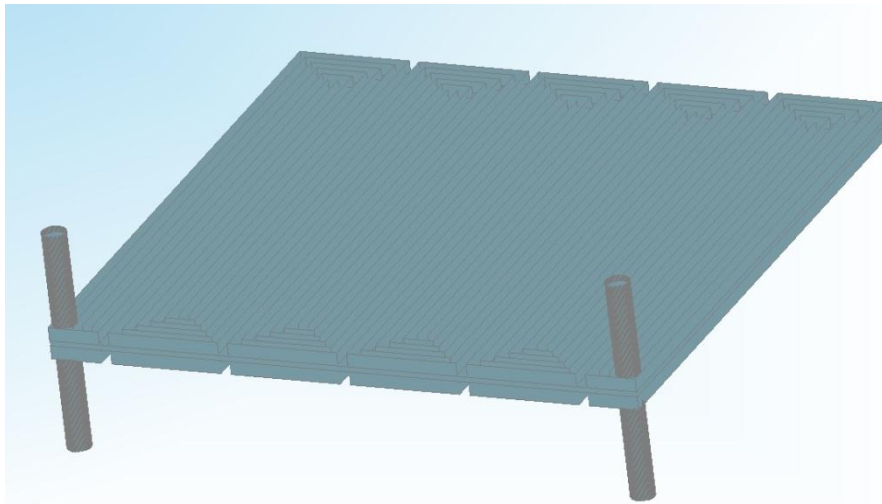
Figure 34: Illustration of the final mesh to simulate the single cell shown in Figure 24. It consists of anode channel mesh, cathode channel mesh, MEA mesh, two inlet and two outlet tubes.

As discussed in chapter 3, the meshing process is followed by setting solver characteristics. Thus, the next section discusses operational settings of the fuel cell examined being adapted to FIRE input requirements.

4.4.2. Operational Settings Adapted to FIRE

To model the fuel cell examined in the laboratory is reconstructed in FIRE as precisely as possible, the operation conditions of the laboratory investigation need to be considered in the CFD calculation. As the working conditions of the test rig cannot be implemented in FIRE directly, they need to be transformed according to FIRE input requirements. The following sub-chapters discuss the operational characteristics requiring adapting in order to model the single cell in FIRE.

4.4.2.1. Inlet Mass Flow

The inlet mass flow of anode and cathode of the CFD simulation are equal to the laboratory experiments. In the laboratory, the inlet is controlled by means of a mass flow controller. The common observation unit for single cell testing is Nml min^{-1}. As FIRE cannot process volume flows, the mass equivalent needs to be calculated. Using the ideal gas equation, Formula 11 can be applied to convert the volume flows to equivalent mass flows.

$$\dot{m}_i = M_i * \frac{p_i * \dot{V}_i}{R * T_i}$$

Formula 11: Calculation of the inlet mass flows $\dot{m}_i$ for component i to be used in AVL FIRE. The molar mass M_i as well as the Temperature T_i and the volume flow $\dot{V}_i$ are depending on the characteristics of the inlet flow of the component i. The general gas constant is represented by R.

For calculation, the pressure and the temperature are assumed to be constant by using the values $p_i = 10^5$ Pa and $T_i = 348$ K. Table 6 summarizes the inlet flows of the examined single cell.

	Anode	Cathode
Laboratory	500 Nml min^{-1}	1000 Nml min^{-1}
CFD	5.807*10^{-7} kg s^{-1}	1.667*10^{-5} kg s^{-1}

Table 6: The inlet flow rates of the CFD calculation are equivalent to those of the laboratory examination. For practical use, the units need to be transformed.

4.4.2.2. Relative Humidity of Inlet Mass Flow

As the feed of anode and cathode is humidified, the initial water content needs to be considered in the CFD solving procedure. For laboratory examination, a humidification of the inlet mass flow of $\varphi_{70°C} = 0.9$ based on 70 °C cell temperature is realized. To prohibit condensation of water, the feed streams are maintained at 75 °C. For implementation in FIRE, the relative humidity needs to be calculated on base of the feed temperature instead of the cell temperature. Therefore, it is necessary to calculate the relative humidity $\varphi_{75°C}$ based on the feed temperature of 75 °C.

The saturation vapor pressure p'_v is depending on the temperature and can be found in literature. Table 7 shows the values of p'_v for the required temperatures [40].

Temperature / °C	Saturation vapor pressure p'_v / mbar
70	311.77
75	385.65

Table 7: The saturation vapor pressure is depending on temperature and overall pressure. The values shown are referenced on atmospheric pressure [40].

Considering Formula 10 and Table 7, the relative humidity $\varphi_{70°C} = 0.9$ implies a partial pressure of vapor $p_v = 280.59$ mbar. In respect to $p'_{v\,75°C} = 385.65$ mbar the relative humidity of the inlet mass flows $\varphi_{75°C} = 0.7276$ has to be implemented.

4.4.2.3. Flow Regime Investigation

As the Fuel Cell Module incorporated in AVL FIRE is not capable of simulating turbulent flow regimes, this issue is discussed subsequently. In this context, the flow regimes occurring within the fuel cell examined are evaluated.

Generally, the flow regime is depending on the Reynolds Number Re as shown in Formula 12. By means of Re, a distinction can be made, whether a flow is laminar, turbulent or in a transition state.

$$Re = \frac{u * d}{\nu}$$

Formula 12: The Reynolds Number Re is used to determine whether a flow is laminar, turbulent or at transition state by means of the velocity u, the diameter d of the cross-sectional geometry and the kinematic viscosity ν of the fluid.

Although the channels of the flow field do not exhibit a circular cross section, the diameter d is used to estimate the turbulence in the flow within the channels. Therefore, d represents the diameter of a tube with the same cross section as the channels of the investigated flow fields. Formula 13 shows the procedure to calculate the required diameter.

$$d = \sqrt{\frac{4 * A_{cross}}{\pi}}$$

Formula 13: The diameter d of a cross-sectional-equivalent tube is depending on the cross section of the channel A_{cross} = 0.85 mm².

As the channels exhibit a height of 1 mm and a width of 0.85 mm, the observed cross section equals 0.85 mm². To match the surface, a cylindrical shape with a diameter d = 1.041 mm is required.

By using Formula 12, the flow regime of the anode and the cathode flow field can be estimated. Table 8 shows the results as well as intermediary results of the calculating procedure. It is assumed that the volume flow splits on each of the three serpentine channels equally. As all three channels exhibit the same number of flow direction shifts and a similar length of flow channels, differences of flow resistances are expected to be negligible. Thus, the volume flows in all three channels are assumed be equal in the present flow regime investigation. Therefore, the calculation is shown for only one of the three channels of the flow field.

	Anode	Cathode
Flow within 3 channels / Nml min⁻¹	500	1000
Flow within 3 channels / m³ s⁻¹	8.33×10^6	16.67×10^6
Flow within 1 channel / m³ s⁻¹	2.78×10^6	5.56×10^6
Cross section of 1 channel / m²	10^{-6}	10^{-6}
Velocity u within 1 channel / m s⁻¹	2.78	5.56
Kinematic viscosity ν / m² s⁻¹ at 75 °C [42]	2.05×10^{-6}	2.05×10^{-6}
Diameter d / m	1.041×10^{-3}	1.041×10^{-3}
Reynolds Number Re	1411.7	2823.4

Table 8: Calculation of the Reynolds Number Re of anode and cathode flow field.

With the assumption of a tubular channel, the anode shows a laminar flow regime and the cathode shows a turbulent flow regime, as the transition from laminar to turbulent is at Re = 2750 [43].

These findings indicate limitations of the fuel cell simulation in AVL FIRE. The Fuel Cell Module required for the solving procedure is capable of solving laminar flow regimes only. Therefore, despite the existence of a turbulent regime, the cathode gas flow is assumed to be laminar within the channels. This is realized by solving the turbulence behavior not with the according model, but by applying the principles of laminar flow.

However, as the Reynolds-Number Re of the regarded cathode flow field (2823.4) does not overshoot the border of turbulence transition (2750) excessively, the assumption can be made that the influence to the simulation results is negligible. Thus, the use of the received CFD simulation results shown subsequently is not considered to be affected significantly by the issue discussed above.

5. Results and Discussion

To compare results of laboratory examination with those of CFD simulation realized in AVL FIRE, different fuel cell operation characteristics are regarded.

On the one hand, a voltage screening is realized, with the conditions discussed in sub-chapters 4.3.1 and 4.3.2. Using this approach, working points on the polarization curve received from laboratory investigations are simulated with FIRE. In this context, the overall voltage-current-interplay is investigated. The results of this comparison can be found in chapter 5.2.

Subsequently, more detailed examination results are shown. Based on the simulation of polarization curve working points, the calculation of local distribution characteristics is realized in AVL FIRE. In this context special emphasis is laid on the reaction current density distribution and the temperature distribution as they are characteristics accessible by laboratory investigation. Their discussion is shown in chapter 5.4. Due to results received from previous polarization curve scanning, altered operation conditions (Table 15) for laboratory results data as well as for the CFD simulation are used. They are shown at the beginning of chapter 5.4. To give meaning to these results, the quality of the received CFD data is discussed first.

5.1. CFD Result Data Quality

To use the CFD simulation results for investigating operation characteristics of the regarding fuel cell, a close look at the resulting data quality is necessary. As the calculation is based on mathematical models to reproduce real operation conditions, a check in respect to physical meaningfulness is of fundamental importance.

In the context of the present simulation, particularly the evaluation of the convergence state is of interest. As the calculation mesh exhibits a large computational size, one general cause of result quality issues can be attributed to a lack of computational power and/or calculation time. As discussed subsequently, this challenge needs to be regraded when evaluating the simulation at hand. Extensive information concerning the convergence of the simulation results presented subsequently can be found in the Appendix (Figure 57 to Figure 71).

Furthermore, the specification of parameters required to model physical processes is a topic to be discussed. The Fuel Cell Module implemented in AVL FIRE shows complex mathematics underlying being fed with a number of physical and electrochemical parameters. Therefore, an approach to improve the physical model will be demonstrated adjacent.

5.1.1. Convergence Characteristics

The quality of the simulation results received by means of AVL FIRE is depending on the reproducibility of the physical geometry, as shown in chapter 4.4.1, as well as on the definition of material parameters as discussed above. Furthermore, the computational power is crucial for the quality to be reached. The computational mesh of the simulation at hand exhibits a noteworthy size of approximately 11 mio. cells, the runtime and hence the computational power turn out to be a practical limitation for the quality of the received CFD results. The simulation characteristics of computational resources available to gain the simulation results are summarized in Table 9.

Characteristic	Description/Value
Mesh cell number	10.911.508
Overall machine memory	504.8 GB
Overall machine CPU´s	32
Number of utilized CPU´s	20
CPU type	AMD Opteron™ Processor 6328
Operating system	Kernel Linux 2.6.32-573.9.1.el6.x86_64

Table 9: Characteristics of the mesh and computational resources.

To evaluate the convergence state of the simulation results, one set is examined. To show the fundamental convergence issues, the discussion is held general. However, for detailed investigation, each set of simulation results needs to be investigated individually. To do so, the Appendix (Figure 57 to Figure 71) of this thesis contains extensive information regarding individual simulation convergence.

Concerning the quality of the FIRE result data shown subsequently, sufficient convergence for specific conclusions can be generally assumed. Especially in terms of reaction current density, the convergence can be regarded as adequate, as Figure 35 shows. Due to the increase of the underrelaxation factor settings (see Appendix, Table 30) compared to the default settings, the required iteration number to assume reaction current density convergence can be found within a range of 800 to 1500 iterations. Thus, the simulation can be regarded as converged in terms of current load.
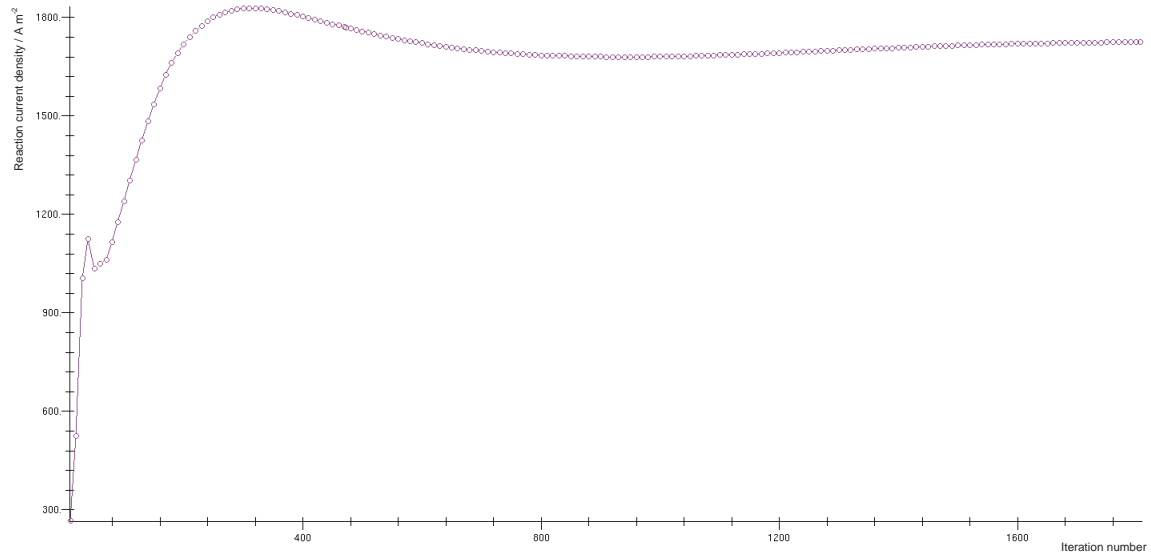
Figure 35: Convergence of the reaction current density / A m⁻² at 70 °C, 800 mV. The reaction current density stays within the same range beginning approximately at iteration number 800. Further convergence behavior can be found in the Appendix (Figure 57 to Figure 71).

Considering the overall convergence of the fuel cell module, the convergence of the fluid water phase is an appropriate parameter to be observed. For evaluation, the total liquid phase mass can be considered (N. Kosir, personal communication, 21.10.16). As Figure 36 depicts, convergence of the total liquid phase mass cannot be assumed for the simulation results at hand. Anyway, the trend towards steady state is obvious. To reach convergence of the liquid water phase it is likely that the simulation requires up to 5000 iterations at least (N. Kosir, personal communication, 21.10.16).
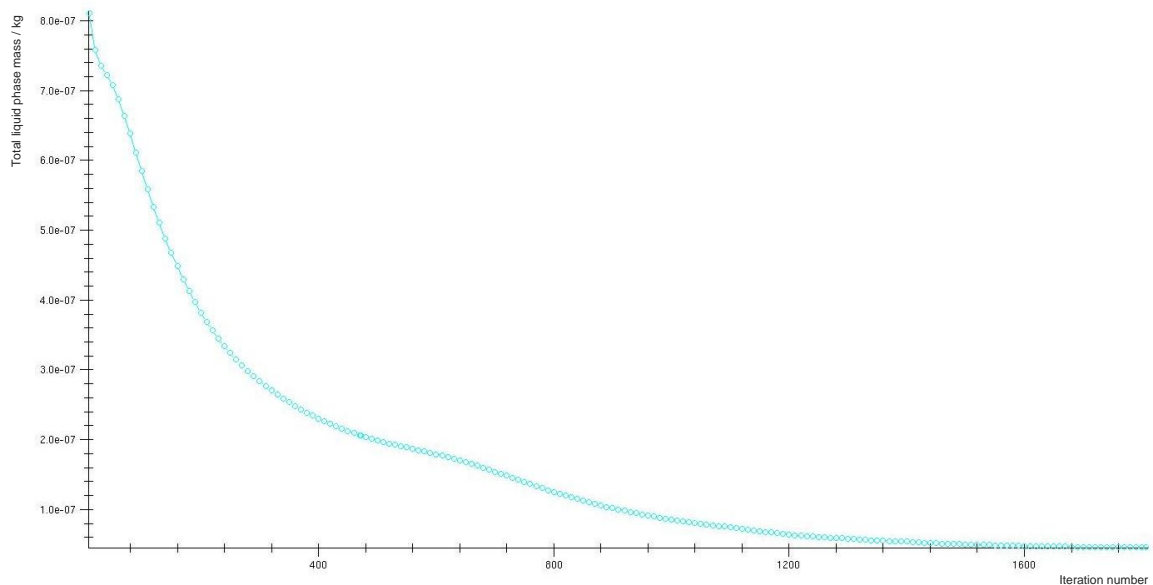
Figure 36: Convergence of the total liquid phase mass / kg at 70 °C, 800 mV. Convergence is not reached yet, but the approach to steady state can be observed. Further convergence behavior can be found in the Appendix (Figure 57 to Figure 71).

The convergence characteristics shown in Figure 35 and Figure 36 require a computational time of 296.6 h. This finding is based on the simulation and hardware characteristics as shown in Table 9.

To reach iteration 5000 in order to improve the liquid phase convergence, an overall calculation time of 821.2 h would be necessary.

The duration of the calculation is based on the extent of the mesh cells. To keep simulation periods low, AVL usually recommends a computational power of one core per 30.000 cells within the simulated mesh (N. Kosir, personal communication, 21.06.16). For the mesh examined, this recommendation would lead to 364 CPUs required. Furthermore, the use of the Fuel Cell Module consumes noteworthy computational resources and therefore prolongs the duration of the simulation additionally, as shown in the Appendix (Figure 65 and Figure 71).

Additionally to the issues discussed above, the quality of the results depends on the definition of correct electrochemistry parameters as well. Thus, the next chapter examines this topic.

5.1.2. Quality Improvements

As shown within the following chapters, the simulation results received by means of AVL FIRE do not fit the results of the laboratory investigations accurately. One explanation may be that the operation behavior of the modelled fuel cell cannot be reproduced exactly by using FIRE.

As geometrical requirements were met, as well as operation conditions, the causes for differences are likely to be found within the solver steering-file of FIRE. For instance, the Fuel Cell Module offers to adjust parameters and properties for electrochemistry modelling. The electrochemical reaction behavior within the simulation is determined thereby. Those parameters are therefore some of the most important for a reliable simulation. However, as they are strongly depending on the used type of fuel cell and materials, the parameters are to be defined by the user.

The electrochemical parameters of the cathode reaction layer are practically used as fitting parameters [37]. FIRE users at AVL fit these parameters to align the simulation with laboratory test results to use the received set of parameters for further modelling (N. Kosir, personal communication, 21.10.16). The parameters in question are shown in Figure 37. As no fitting values were available when conducting the examination presented within this thesis, default values suggested by FIRE were used to execute the simulation.
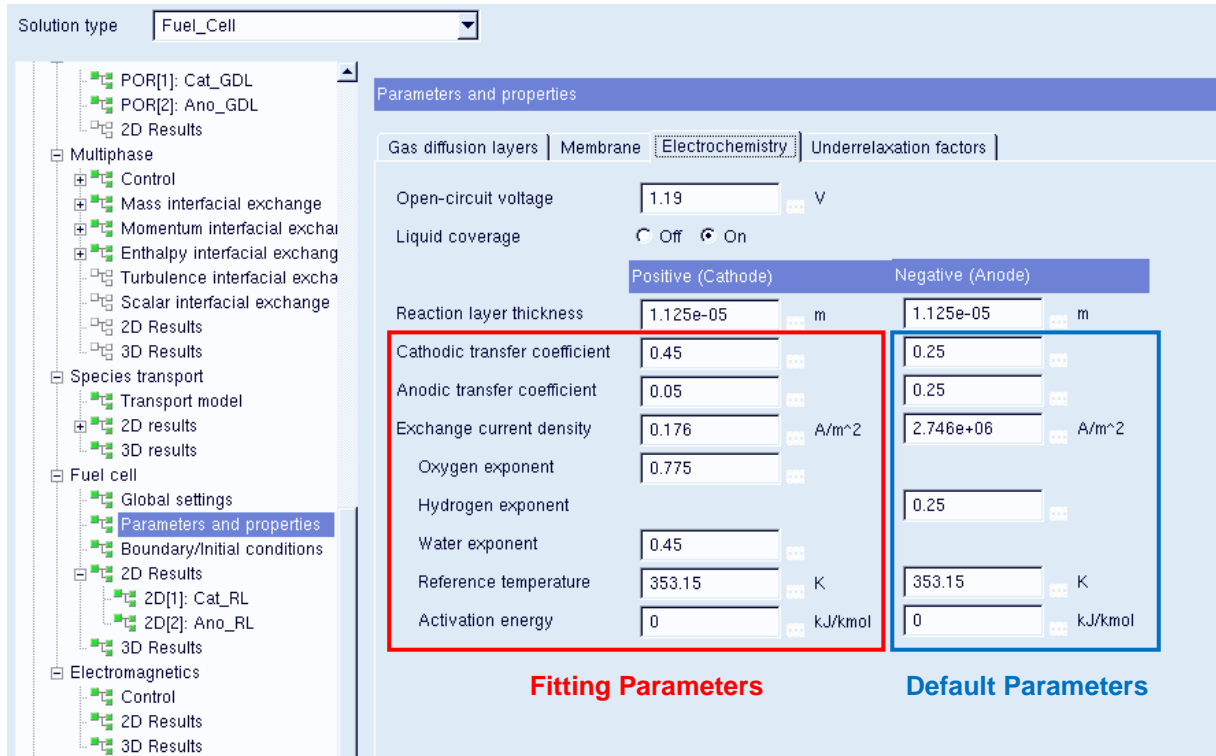
Figure 37: Electrochemical parameters are used for fitting to align the FIRE simulation to experimental results. While the cathode parameters are fitted, the anode parameters stay set default.

The values set for the parameters shown above have crucial influence on the results concerning the reaction current density. As Formula 14 illustrates, the reaction current density i_r is depending on the anodic transfer coefficient k_a and the cathodic transfer coefficient k_c.

$$i_r = i_0 * \left[\exp\left(\frac{n_e * k_a * F}{R * T} * \eta_{act} \right) - \exp\left(-\frac{n_e * k_c * F}{R * T} * \eta_{act} \right) \right] + i_{r,cross}$$

Formula 14: Calculation of the reaction current density i_r in FIRE by means of the Butler-Volmer equation including the effect of gas crossover across the membrane [37]. The anodic transfer coefficient k_a and the cathodic transfer coefficient k_c are supposed to act as fitting parameters.

Furthermore, the reaction current density is calculated by means of the exchange current density i_0. The determination of the exchange current density i_0 itself is based on the hydrogen partial pressure exponent b_{H_2}, the oxygen partial pressure exponent b_{O_2} and the water partial pressure exponent b_{H_2O} as Formula 15 shows.

$$i_0 = i_{0,ref} * \left(\frac{p_{O_2}}{p_{ref}} \right)^{b_{O_2}} * \left(\frac{p_{H_2}}{p_{ref}} \right)^{b_{H_2}} * \left(\frac{p_{H_2O}}{p_{ref}} \right)^{b_{H_2O}} * f_1 * \exp\left[-\frac{E_{act,i_0}}{R} * \left(\frac{1}{T} - \frac{1}{T_{ref,i_0}} \right) \right]$$

Formula 15: Calculation of the exchange current density i_0 [37]. The hydrogen partial pressure exponent b_{H_2}, the oxygen partial pressure exponent b_{O_2}, the water partial pressure exponent b_{H_2O} act as fitting parameters. The same is true for the activation energy E_{act,i_0} of i_0 as well as the reference value of the exchange current density $i_{0,ref}$ and reference temperature T_{ref,i_0}.

The activation energy E_{act,i_0} and the reference temperature T_{ref,i_0} need to be included in Formula 15 as well in order to determine i_0.

To complete the statements of Formula 14 and Formula 15, Table 10 lists all parameters required for the calculation of the exchange current density i_0 and the reaction current density i_r. Further information regarding the calculation can be found in [37].

Symbol	Name	Dimension
i_r	Reaction current density	A m^{-2}
i_0	Exchange current density	A m^{-2}
$i_{0,ref}$	Reference exchange current density	A m^{-2}
k_a	Anodic transfer coefficient	-
k_c	Cathodic transfer coefficient	-
n_e	Charge transfer number, n = 2 for PEMFC	-
F	Faraday constant, F = 96487	As mol^{-1}
R	Universal gas constant, R = 8.314	J mol^{-1}K^{-1}
T	Temperature	K
η_{act}	Activation overpotential	V
$i_{r,cross}$	Crossover current density	A m^{-2}
p_{O_2}	Partial pressure of oxygen	Pa
p_{H_2}	Partial pressure of hydrogen	Pa
p_{H_2O}	Partial pressure of water	Pa
p_{ref}	Reference pressure, p_{ref} = 101325	Pa
b_{O_2}	Oxygen partial pressure exponent	-
b_{H_2}	Hydrogen partial pressure exponent	-
b_{H_2O}	Water partial pressure exponent	-
f_1	Factor for liquid coverage effect on reaction rate	-
E_{act,i_0}	Activation energy for i_0 determination	J mol^{-1}
T_{ref,i_0}	Reference temperature for $i_{0,ref}$ determination	K

Table 10: List of symbols required to describe Formula 14 and Formula 15 [37].

As shown, AVL FIRE requires an extensive set of different parameter to model fuel cell reaction characteristics. Detailed investigation of FIRE´s ability to reproduce laboratory results is bound to the development of such a set of parameters. However, this enterprise would exceed the scope of the thesis at hand.

However, to examine the quality of CFD simulation results present a comparison to laboratory results is required. The following chapter investigates the calculation of a polarization curve by means of AVL FIRE using the mesh discussed in chapter 4.4.

5.2. Polarization Curve Investigation

As shown in chapter 2.1.3, a polarization curve model can be used to characterize the operation behavior of a fuel cell. Within this thesis, the enterprise is tackled to investigate the usability of AVL FIRE for fuel cell operation modelling. Therefore, the polarization curve of a single cell is recorded in a laboratory setup, as shown in chapter 4.3. The results of this investigation are presented in Table 11. They are received by conducting the experimental settings shown in chapter 4.3.

Laboratory examination results	
Voltage / mV	**Current / A**
450.172	15.218
534.406	11.267
622.384	8.066
709.469	4.612
798.841	1.789

Table 11: Results of the polarization curve recording by means of single cell laboratory examination. The investigated voltages are set according to Figure 27.

The trend of the values shown above goes along with the characteristics of the polarization curve: Higher current loadings lead to decreased voltages. The fact that the voltage values deviate from those defined in Figure 27 can be led back to the electrical regulation used in the laboratory settings.

The values shown in Table 11 are used as reference for comparison with the results (shown in Table 12)from the simulation discussed in chapter 4.4. For comparison, the simulation of three different working points is conducted. In order to accomplish this, the calculation time has to be kept short. Therefore, the calculations are terminated when sufficient convergence of the reaction current density can be assumed. An exception is the 600 mV simulation series. Due to an issue, which is likely to occur in the automated mesh decomposition process (C. Großegger, personal communication, 17.10.16), the calculation ended before sufficient convergence is reached. According to the convergence trend, a decreased current value is likely to be the outcome of a converged calculation status of the 600 mV series. Further details and properties of the simulation can be found in the Appendix (Figure 57 and Figure 58).

Simulation results	
Voltage / mV	**Current / A**
600	40.015
700	19.790
800	4.313

Table 12: Results of the single cell simulation by means of AVL FIRE. For the CFD examination, the voltage needs to be specified in the solver-steering-file while the current is calculated.

Figure 38 plots the current voltage relations of the laboratory examinations and the AVL FIRE-simulation (shown in Table 11 and Table 12).
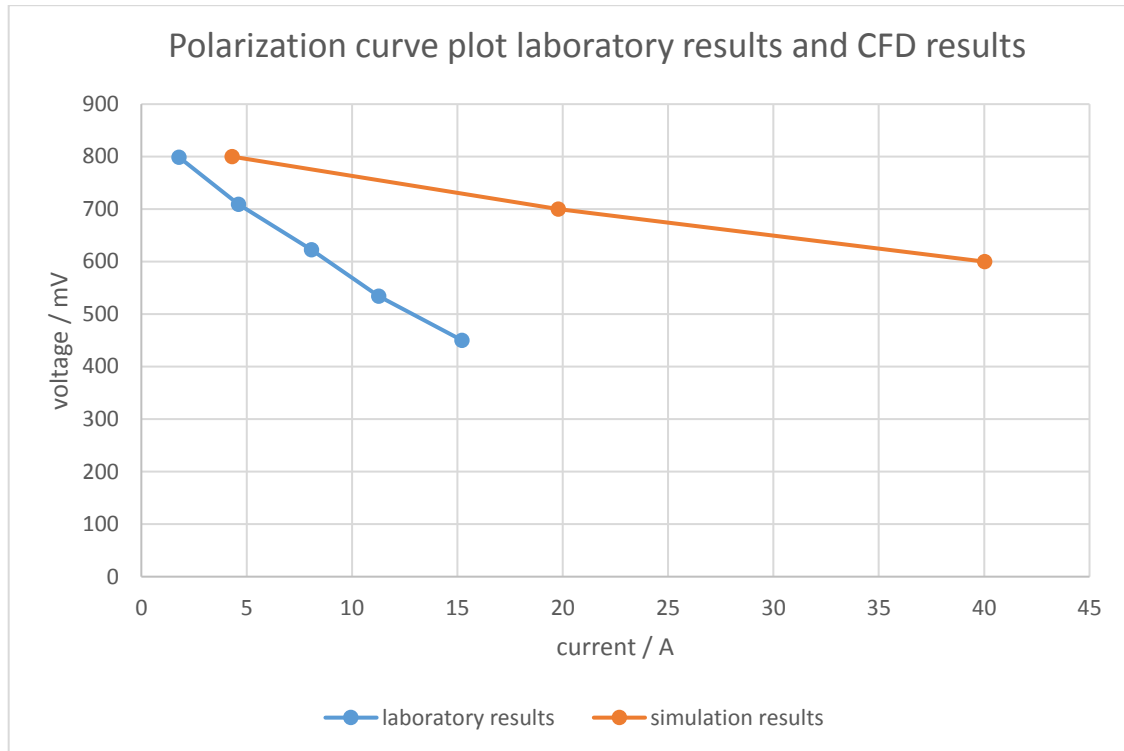
Figure 38: Comparison of polarization-curve working points. The blue dots indicate the results received from laboratory examination, the orange dots represent the results of the CFD-simulation by means of AVL FIRE.

It is obvious that not all laboratory working points have equivalent CFD simulation results. This circumstance arises from the fact that the simulation requires extensive computational power due to its mesh properties, as shown in chapter 4.4. Therefore, only three calculations to be compared to the laboratory examination are conducted.

The tendency of the simulation results shown in Figure 38 reveals that higher voltages improve the comparability. Table 13 illustrates the derivation of both examinations in respect to current loading

Voltage / V simulation/laboratory	Current loading / A simulation I_{sim}	Current loading / A laboratory I_{lab}	Derivation $d = \frac{I_{sim}}{I_{lab}} - 1$
600 / 622.384	40.015	8.066	396.1%
700 / 709.469	19.790	4.612	329.1%
800 / 798.841	4.313	1.789	141.1%

Table 13: Comparison and derivation of simulation results and laboratory results concerning polarization curve modelling.

As Table 13 shows, the laboratory results differ from those obtained from simulation. The causes for this are assumed to be found within the SSF-file of the FIRE-simulation. As shown in chapter 5.1.2, a fitting of electrochemical reaction parameters is required to adjust the simulation to laboratory examinations.

Furthermore, the performance during the single cell measurement was unexpectedly low and thus might not be fully representative of the state-of-the-art fuel cell systems. The results were, however, not validated during the realization of this thesis. Therefore, results from preceding measurements were used for the comparison of the spatially resolved current and temperature profiles.

The simulation results presented are used within the next chapter to examine the influence of current loading to electrochemical and electrical heating. The focus is on qualitative relations.

5.3. Electrochemical Heating due to Current Load

Subsequently, the reaction current density is presented in relationship to the reaction heat. Table 14 shows the CFD simulation results of the investigated fuel cell in respect to heating phenomena. As can be seen, heating due to ohmic resistances in a fuel cell is usually lower than heating due to the electrochemical reaction. Especially at low current, the ohmic heating can be neglected. In higher current regions, the ohmic heating needs to be considered as well, as resistance losses increase due to heightened current densities within the resisting elements.

Electrochemical reaction heat behavior due to simulation results.				
Voltage / mV	Current / A	Ohmic heating / W	Electrochemical reaction heat / W	Specific reaction heat / W A^{-1}
600	40.015	4.92	31	0.775
700	19.790	1.08	14.7	0.723
800	4.313	0.08	2.95	0.684

Table 14: Excess of ohmic and electrochemical heating due to the applied current for the simulated fuel cell. The electrochemical reaction heat increases with the applied load, as the specific reaction heat / W A^{-1} in the last row shows.

The heating issue increases with heightened fuel cell strain as a consequence of the results shown in Table 14. Besides the increase of the specific reaction heat, the ohmic heating becomes a challenge to be considered too.

Due to the findings in chapter 5.2 the quantitative values shown in Table 14 need to be considered with care. However, they represent a lead for further examination on the one hand and depict relationships of heating phenomena on the other hand.

5.4. Comparison of Spatial Distribution

The examination of fuel cells by means of laboratory techniques is usually bound to interfaces of the cell to its environment. In order to obtain a more fundamental understanding on the local conditions, special measurement devices and complex examination settings are required. Thus, the survey of a CFD fuel cell model in respect to its inside operation conditions is of special interest.

Furthermore, the comparison of simulation results and accessible laboratory investigation results allow giving answer whether AVL FIRE is an adequate tool to examine fuel cell operation behavior.

Thus, a comparison of spatial distributions can be found subsequently. The results of the laboratory investigation are received by means of a segmented current can shunt type S++ device as presented in chapter 4.3. The simulation results are obtained by cutting the computational mesh at the area of interest. The resulting pictures show the single cell elements exhibiting characteristic values. The resolution of the simulation results is equal to the mesh resolution in terms of cell number and distribution.

5.4.1. Experimental Base of Comparison

For the comparison of spatial distribution characteristics, the approach described in chapter 4.3 is adapted. As discussed in chapter 5.2 and shown in Figure 38, the chosen laboratory settings do not represent FIRE simulation results accurately, particularly when investigating lower voltages. Therefore, the operation parameters of the laboratory investigations are changed to receive comparable results. Table 15 shows the characteristics of the laboratory investigation used for the following comparison. The identification of laboratory results shown subsequently is not a part of the master thesis at hand.

Cell operation temperature	80 °C
Cell operation pressure	1 atm
Anode feed	Hydrogen, pure
Cathode feed	Synthetic air: 20.9 mol% Oxygen 79.1 mol% Nitrogen
Anode inlet flow	500 Nml/min
Cathode inlet flow	1000 Nml/min
Temperature anode and cathode feed	85 °C
Dew point anode and cathode feed	80 °C

Table 15: Single cell investigation parameters for comparison of spatial distribution characteristics.

The single cell components for this investigation are listed in Table 16.

Component	Type	Thickness / µm
Membrane	Nafion® XL	27.5
Gas diffusion layer	SIGRACET® Gas Diffusion Media, Type GDL 24 BC	325
Gasket	PTFE textile flat gasket	220

Table 16: Component specifications of the single cell investigation used for the comparison of spatial distribution characteristics.

To get a base for comparability of laboratory and simulation distribution results, one voltage point is selected. All results shown subsequently refer to this operation condition. This approach ensures that the conversion of hydrogen as well as oxygen is comparable. Furthermore, the generation of water and therefore humidity conditions are similar. For the present discussion, 812 mV at the laboratory examination and 800 mV at the CFD-simulation are observed, as Table 17 shows.

	Voltage / mV	Current / A
Laboratory examination	812	2.6
CFD-simulation	800	2.95

Table 17: The comparison of the laboratory results and the CFD simulation is based on the equivalence of voltage.

Table 17 shows that those values are more adequate to compare results than using the results from the laboratory investigations shown in Table 11. The comparison of overall current at a voltage of 812 mV in Table 17 shows that the laboratory examination exhibits a slightly lower performance than the simulation by means of FIRE. The current value received from the CFD investigation shown in Table 17 differs 13.3 % from the result of the laboratory investigation.

When comparing the simulation results shown in Table 17 to the results shown in Table 11, one can find that the simulation performs better at low temperatures: 2.95 A at 80 °C and 4.3 A at 70 °C. The cause for this phenomenon is likely to be found within the calculation approach of the reaction current density as shown in Formula 14 and Formula 15. A simple point of view is presented in chapter 5.3. As the conversion of hydrogen and oxygen generating water is exothermic, surrounding temperature influences the reaction equilibrium.

5.4.2. Current Density Distribution

The results of the laboratory current density distribution investigation are shown in Figure 39. The S++ current scan shunt features 100 measurement points recording the local current densities. The inlet of hydrogen and air can be found at the rear corner. The current density increases in direction of the gas outlet. Its maximum is located within the lower half of the geometry profile near the gas outlet. Furthermore, the measurement points along the edge show decreased current density.
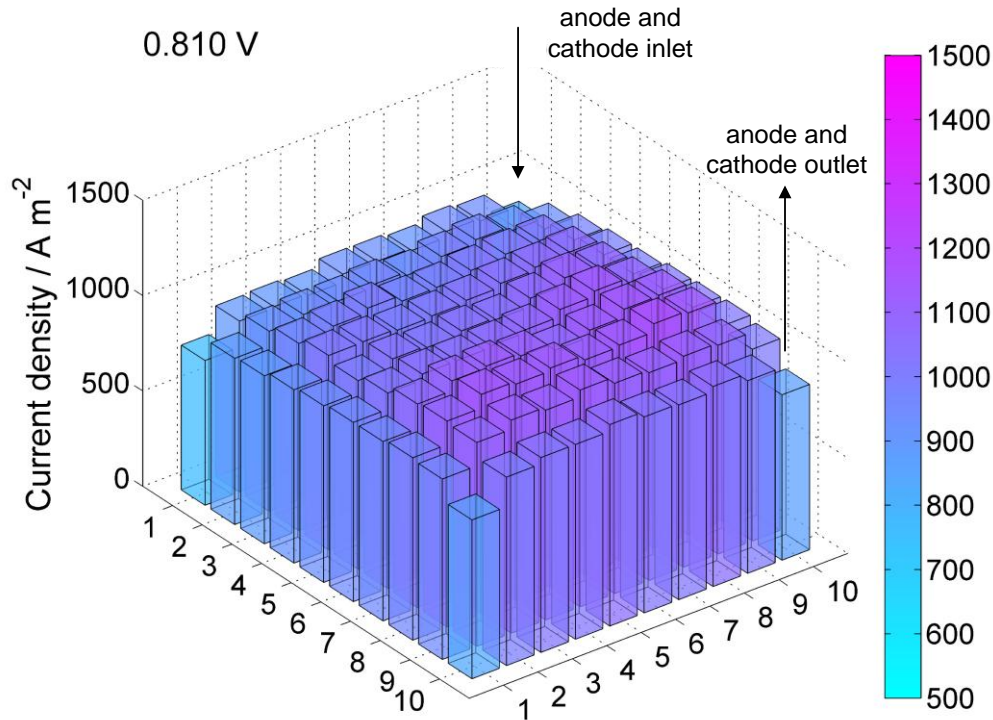
Figure 39: Current density distribution from laboratory examination. The region near the outlet shows the highest current densities. The measurement points along the edges show decreased current density.

As general characteristic of Figure 40, the homogeneity of the distribution can be noted. No special runaway values are visible and the value distribution shows only small gradients.

Figure 40 shows the simulation results of AVL FIRE in terms of spatial distribution of reaction current density. As can be seen, the distribution looks similar to Figure 39 at first sight. But contrary to laboratory results, the highest reaction current densities occur within the first half of the geometrical profile behind the gas inlets. Anyway, both profiles show a good comparability in terms of distribution intensity. The distributions are both comparably homogenous and each shows a maximum with slightly increased current density and recorded values of both investigations can be found to be within a range of 1000 A m^{-2} and 1200 A m^{-2}.
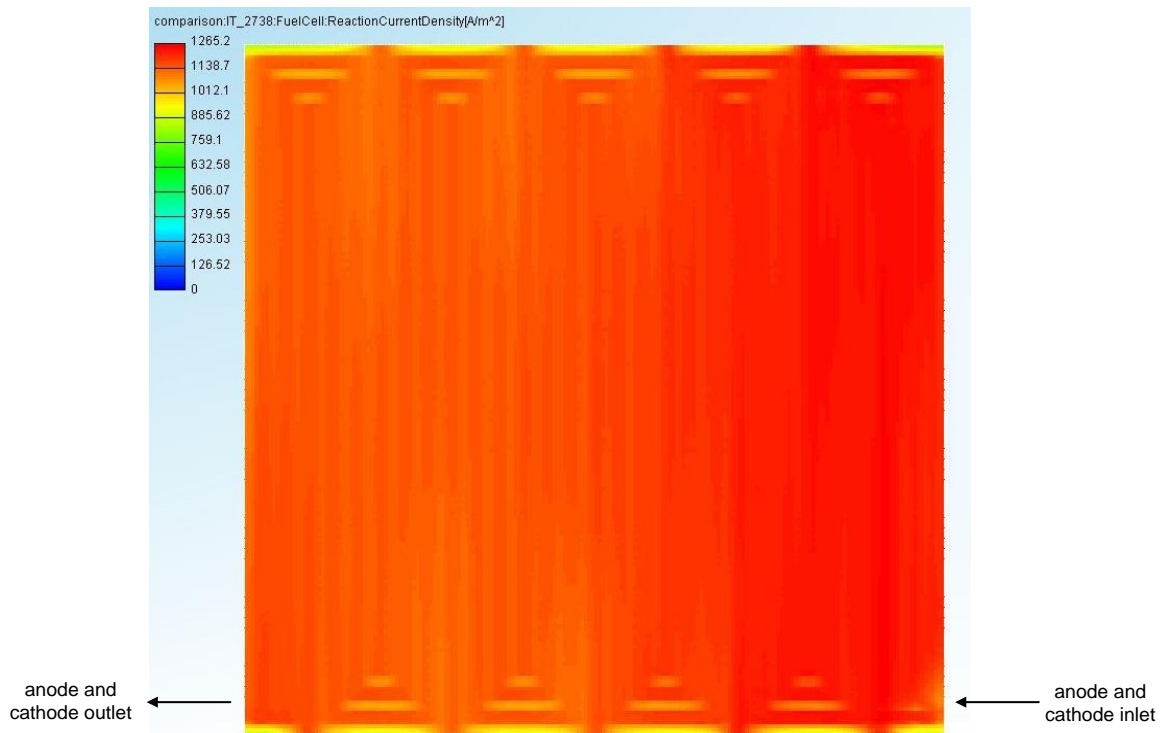
Figure 40: Reaction current density received from CFD simulation. The cut position is located at the anode side of the membrane surface. The color bar is scaled to start at zero like the scaling in Figure 39.

To improve the resolution, the minimum value of the color bar is increased. Thus, differences barely notable in Figure 40 are highlighted. Figure 41 shows improved resolution in terms of current density distribution.

Most eye-catching in Figure 41 is the fact that the current density distribution shows the highest values close to the inlet of hydrogen and air. This finding is contrary to the laboratory results. Subsequently, chapter 5.4.4 discusses extensively the causes for this relationship. However, the simulation results obtained by means of the procedure shown within this thesis predict a decay of the current density distribution from the inlet to outlet region of the flow field.

Furthermore, the areas along the edges show lower current densities as well. Actually they exhibit the lowest values within the whole geometrical profile. As this behavior can be found in Figure 39 too, one can expect that its cause can be found in the experiment arrangement.
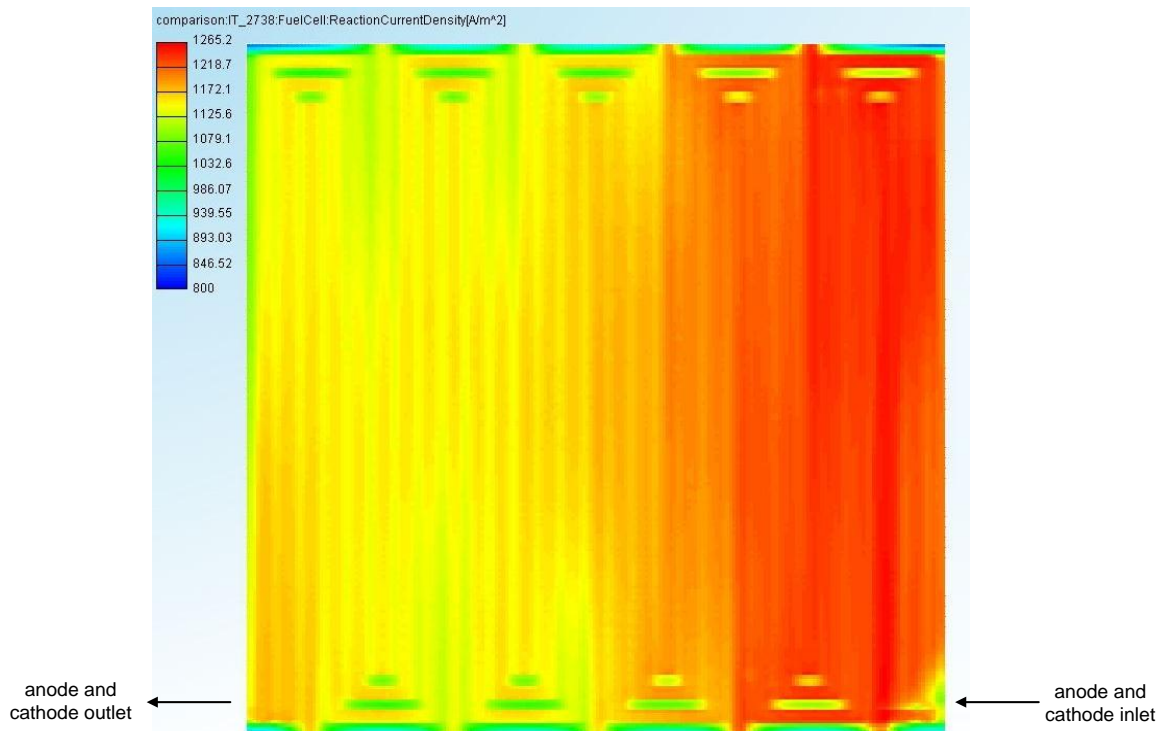
Figure 41: Reaction current density received from CFD simulation. The cut position is located at the anode side of the membrane surface. The color bar is scaled to start at 800 A m⁻².

As the comparison above shows, the current density distributions received from laboratory investigation is reproducible by means of AVL FIRE along the general flow pattern. However, the simulation results indicate that the area of highest reaction current density can be found closer to the gas inlet than the gas outlet. The noteworthy interpretation challenge of the CFD simulation results is the convergence status of the calculation. As discussed in chapter 5.1.1, increased calculation time and computational power most probably lead to higher validity of the simulation results.

5.4.3. Temperature Distribution

The temperature distribution recorded at the laboratory investigation is illustrated in Figure 42. The S++ current scan shunt exhibits 25 measurement areas to record local temperatures. The distinction of differing temperatures is supported by the color bar. Due to electrical regulation, the set temperature of 80 °C was not fulfilled completely during measurement. Anyway, the distribution that is shown does not lose any of its meaningfulness.
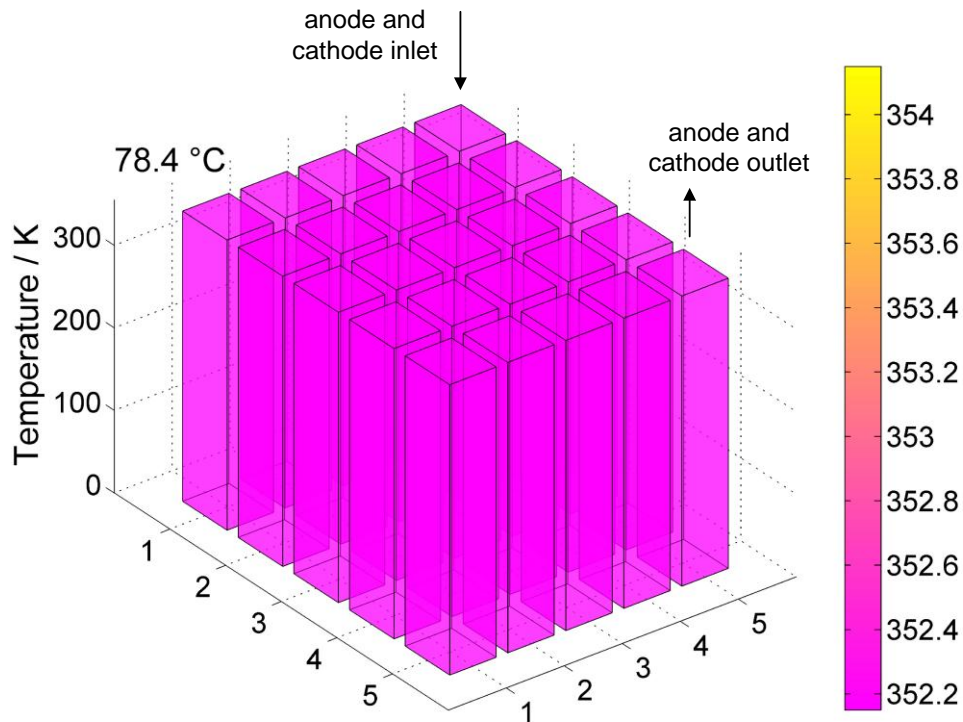
Figure 42: Temperature distribution from laboratory investigation. As the temperature evaluation by means of the color bar shows, the temperature is generally constant across the whole observed cross section.

As visible, the measuring points do not record noticeable temperature differences. The even temperature distribution is due to the fact that the investigated single cell exhibits electrical heating support across the whole observed area. Therefore, the temperature profile can be regarded as meeting the expectations.

In terms of simulation results, Figure 43 shows similar results compared to the laboratory investigation in Figure 42. The temperature distribution exhibits even characteristics across the observed geometrical region. When having a closer look one can find that the short traverse channels exhibit a lesser temperature. Equally to the current density distribution discussion above, this characteristic is depending on the simulation iteration number. Thus, it is probably to de identified as a convergence issue.
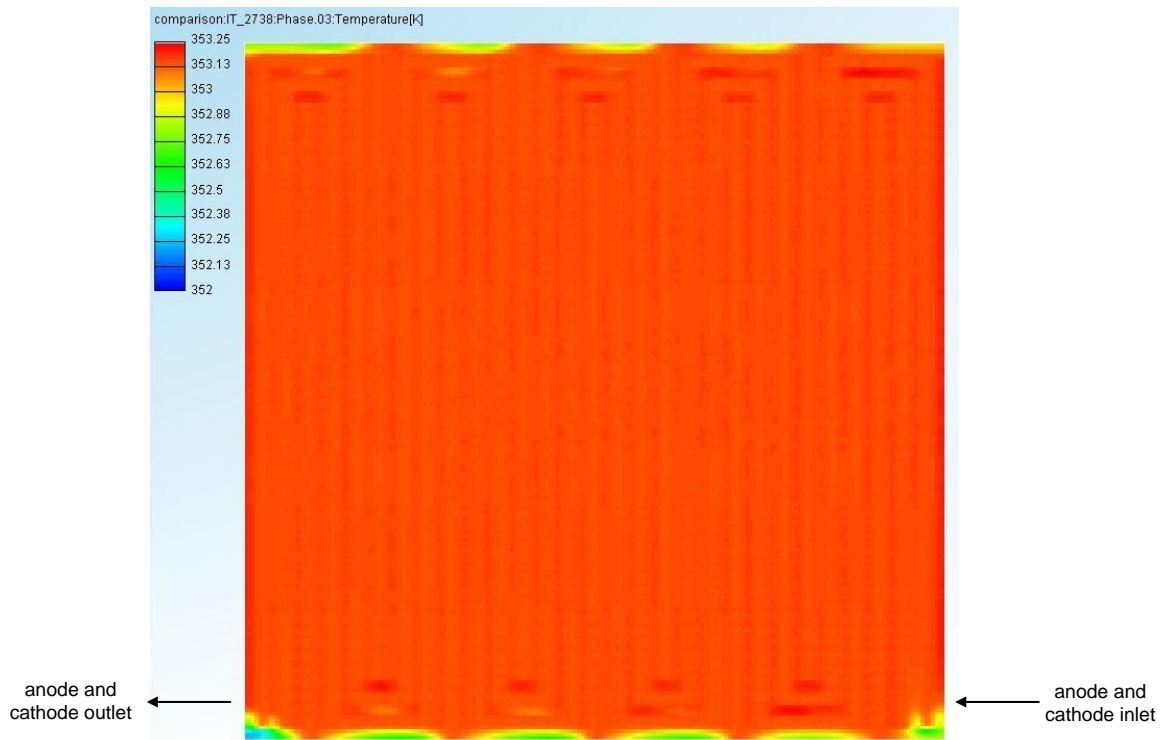
Figure 43: Temperature distribution received from CFD simulation. The cut presented is located in the middle of the membrane. The comparison to Figure 42 shows that both illustrations exhibit an even temperature distribution.

Due to the simulation setup, the results received were expected. As all channel walls are set to a constant temperature, they act as continuous temperature regulation elements. By means of this approach the function of the bipolar plate is modelled in a reasonable way.

When refining the resolution of the temperature scale, more details become apparent. Figure 44 shows a maximum temperature of 353.15 K. This value is decreased by 0.1 K compared to Figure 43.

The white regions visible in Figure 44 mark areas where the local temperature is exceeding the maximum value of 353.15 K. Regarding these areas, the pattern of the flow field´s channel rows can be recognized. Figure 44 shows, that not only the heat input due to the isothermal channel walls is influencing the temperature profile. Also, the heat resulting from the electrochemical reaction needs to be considered. Most reaction heat is generated in the regions where most reactants are available.
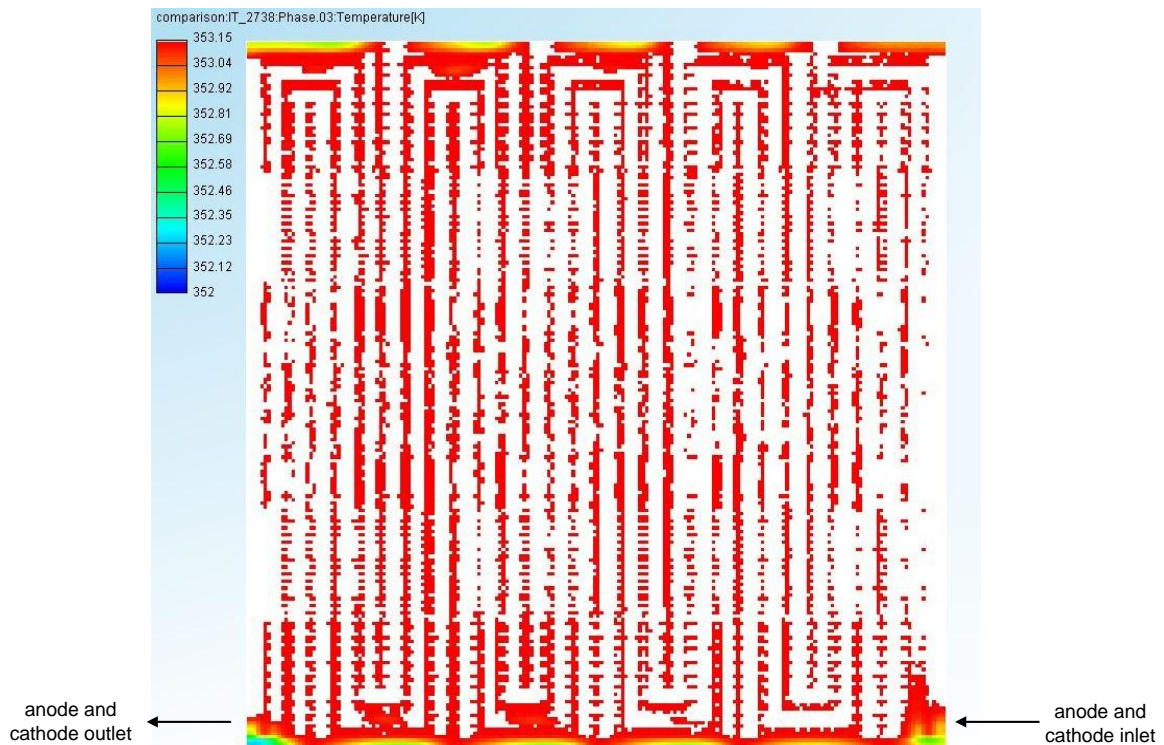
Figure 44: Temperature distribution received from CFD simulation. The temperature scale is optimized so that white color marks the areas exceeding the temperature scale maximum. The exceeding areas illustrate the channels of the flow field. The cut is located in the middle of the membrane.

Figure 43 and Figure 44 represent geometrical cuts in the middle of the membrane geometry. To observe the temperature not within solids only, Figure 45 shows the temperature distribution of the anode channel gas media. The cut is located at half channel height. When regarding Figure 45 with respect to the color bar´s temperature assignment one can find that the temperature within the channel is held within a range of several tenths of one Kelvin most widely. Significant temperature changes of the hydrogen gas on its way through the channels cannot be found.

The differences visible are likely to results from convergence issues as discussed above, in particular the lowered temperature within the short traverse channels. Comparing the temperatures of the outermost traverse channel in Figure 45 to Figure 43, one can find that the temperature within the membrane is lower than within the anode gas channel. Thus, the heat flux originates from the traverse channel elements and moves to membrane regions, which are most likely acting as temperature sinks due to convergence issues. However, also the channel areas with locally increased temperature are assumed to result from convergence issues.
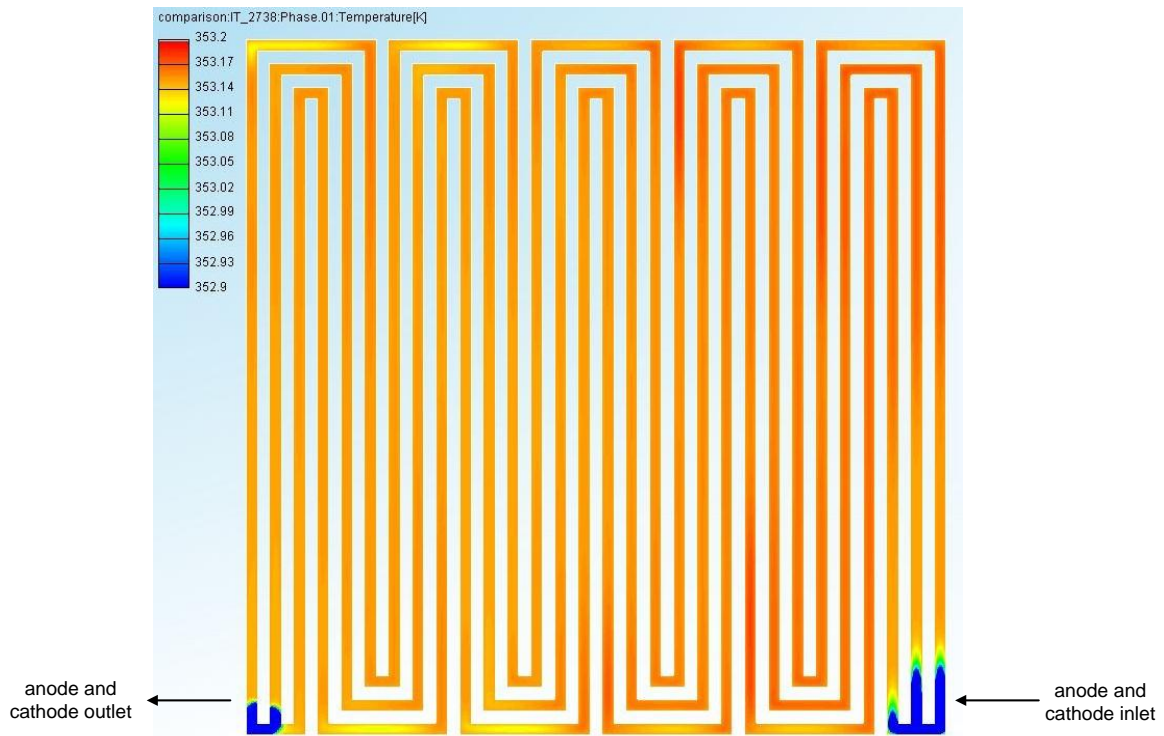
Figure 45: Temperature distribution of the anode channel gas media. The cut is located at the half channel height.

Furthermore, Figure 45 shows that the channel inlet and outlet exhibit lower temperatures despite of the inlet temperatures being set to 85 °C. Although the cause is not exactly known, a geometrical meshing characteristic could be responsible for this phenomenon. As shown in the Appendix (Figure 51), the inlet tubes are connected to the channel geometry by means of the ZHF1 face selection. It exhibits a wall section representing the bipolar plate land at the inflow region. Due to the decrease of cross sectional area for the inlet gas, a nozzle effect may be resulting. When the media passes this obstacle, the expansion may cause a local temperature drop by several tenths of Kelvin, depending on the pressure difference [44]. Convergence as well as boundary condition modelling issues cannot be excluded, as prolonged simulation duration leads to a decrease of the temperature differences. However, the sharpness of the cooler area increases. Thus, it is likely that these cooler sections exist at an improved convergence state too. However, the discrepancies shown in Figure 45 remain within the range of one Kelvin.

As discussed above, the temperature distribution of the laboratory investigation and the CFD simulation show similar characteristics. This fact results from the external heating elements both approaches feature. Furthermore, the simulation shows phenomena likely caused by the numerical simulation approach and probably vanishing at improved convergence state. However, fine resolved simulation results are difficult to compare to the laboratory results presented, as the temperature resolution is limited to 5x5 measurement segments.

5.4.4. Discussion of Comparison Discrepancies

In regard to current density distribution and temperature distribution, the role of the fuel cells environment needs to be considered. The CFD simulation exhibits ideal environment conditions while the fuel cell operated in the laboratory is exposed to real surroundings. Therefore, the laboratory results are subject to ever present disturbance resulting either from test settings or atmospheric conditions.

In this context the heating of both approaches needs to be noted: The fuel cell examined in the laboratory is heated by electrical heating elements. They are regulated by means of an electric control circuit. This implies sensitivity to disturbances and inertance due to bipolar plate mass. Contrary, the cell simulation in FIRE exhibits a flow field of constant temperature. Thus, operation disturbances because of temperature variation influences are reduced for the bigger part.

Furthermore, the simulated fuel cell shows constant and exactly defined inlet gas flows. The fuel cell in the laboratory is fed with gas flows exhibiting mostly the characteristics predefined. However, in an experimental setup, a full monitoring is not possible. Therefore, phenomena in the inside of the fuel cell can occur, influencing particularly the peak shift of the current density distribution. Furthermore, the inability of FIRE´s Fuel Cell Module to model turbulent flow regimes may also be accountable for the local current maxima differences of laboratory investigation and CFD simulation results as shown in chapter 4.4.2.3. Moreover, material properties of laboratory tests are not fully available and thus might not be portrayed correctly in the FIRE simulation, as discussed in chapter 5.1.2. Particularly the membrane characteristics are responsible for the electrochemical reaction. Summarized, the differences of both examinations can also result from a control mismatch of both approaches compared to each other.

In the end, also the location of data record may be crucial. The laboratory results are received by means of a current scan shunt which is placed in between the cathode flow field plate and the endplate of the fuel cell assembly. Cross current fluxes within the bipolar plate may lead to an altered current density record compared to the MEA inside. Investigations of the current scan shunt used assume that changes of local current density distribution within the range of 5 % can occur (R. Kraume, personal communication, 16.04.14). Considering absolute current density values in the range of 1000 A m^{-2} to 1200 A m^{-2}, an error up to 50 A m^{-2} or 60 A m^{-2}, respectively can occur.
On the contrary, the investigation of the simulated fuel cell´s characteristics is located within the geometrical mean of the membrane. Due to conduction resulting in evening effects, it is likely that both recording approaches show differences caused by their respective nature. However, the gradients of the current density distribution of both investigation approaches are low compared to the maximum values. Apart from the location of the current density maxima, the current density distributions of both examinations are homogeneous and well comparable.

As the comparison of the results is reasonable and discrepancies are discussed, further results of the CFD simulation will be presented subsequently. As no laboratory results for the respective parameters are available, they represent a prediction of operation conditions occurring within a fuel cell run in the laboratory.

5.4.5. Reactants Mole Fraction

Next to the current density and temperature distribution, the distribution of the mole fraction of each reactant is investigated. Their distribution is of special interest as their presence is required for the electrochemical reaction to take place. Uneven distribution would lead to different local reaction conversion due to a lack of reaction partners.

When having a look at the mole fractions in this context, one has to be clear about the fact that they represent the partial pressure of the species observed. Due to connection given by the ideal gas equation and the fact that the examined fuel cell is operated at 1 bar, the mole fraction of a species is equivalent to its partial pressure.
Furthermore, the humidification of the inlet gases needs to be considered. As the water molecules are mixed up with the dry inlet gas, they represent a part of the gaseous molecules mixture. Thus, the mole fraction of the observed species is lowered in respect to the relative humidity of the gas flow.

5.4.5.1. Anode Flow Field

The anode flow field is fed with hydrogen. Figure 46 shows the distribution of hydrogen within the anode channel. As discussed above, the hydrogen mole fraction of the gaseous phase is reduced due to the humidification with water molecules. When having a look at Figure 46, one can find that the partial pressure of hydrogen within the channels does show a slight tendency of increasing while running through the channels.
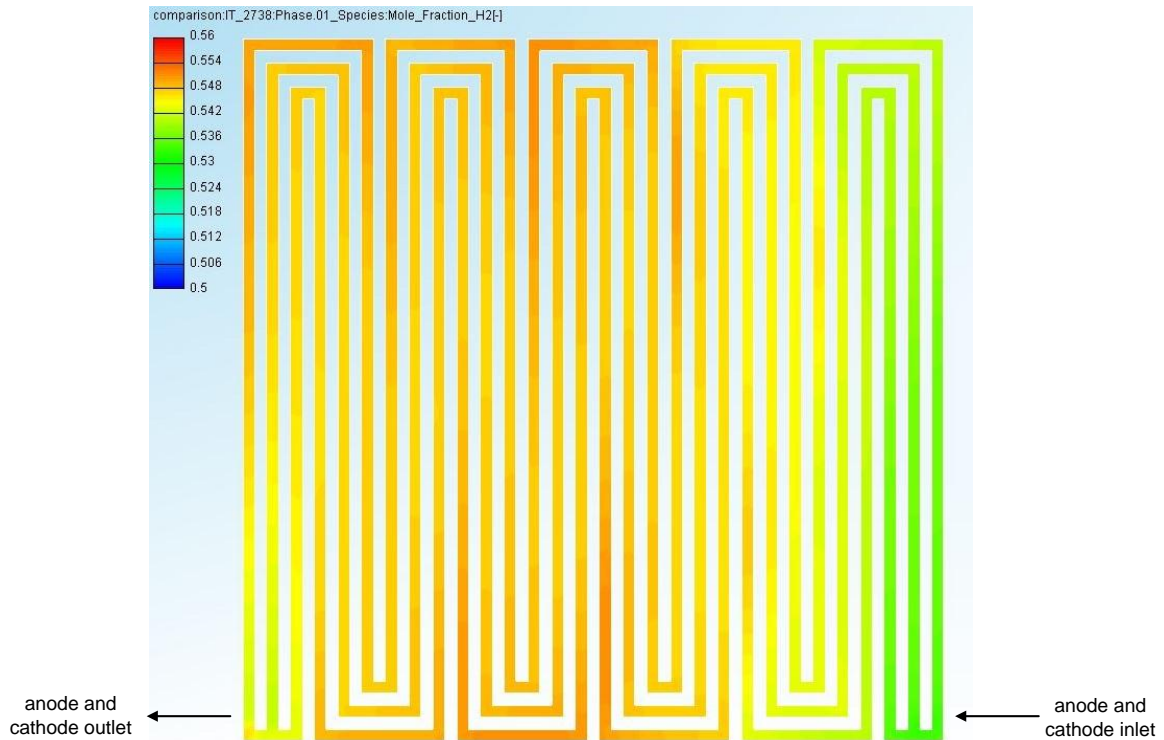
Figure 46: Distribution of the hydrogen mole fraction of the gaseous phase within the anode channel. Simulation results suggest that hydrogen mole fraction increases on its way through the anode flow field.

Anyway, the simulation results suggest that an increase of hydrogen concentration in the gas flow along the flow field channels is present. As no absolute molecule flow can be displayed in FIRE, another approach is used to investigate this phenomenon. The only other significant species appearing within the anode channel is represented by gaseous water. Due to this fact, a relationship between the water content within the anode channel and the obvious increase of hydrogen partial pressure can be assumed. Thus, the mole fraction of gaseous water is illustrated in Figure 47.

As Figure 47 shows, the partial pressure of gaseous water due to feed stream humidification is increased close to the flow field inlet. Leaving the inlet region, its concentration goes down to a lower level, showing fluctuations. These fluctuations are assumed to represent numerical convergence issues. However, the decrease of water after entering the flow field is significant. In this context, the increase of hydrogen mole fractions is obvious: Decreased amount of water is equal to increased hydrogen content, as only these two species are present within the gaseous phase of the anode channel and thus a sum of 1 for all species needs to be conserved.
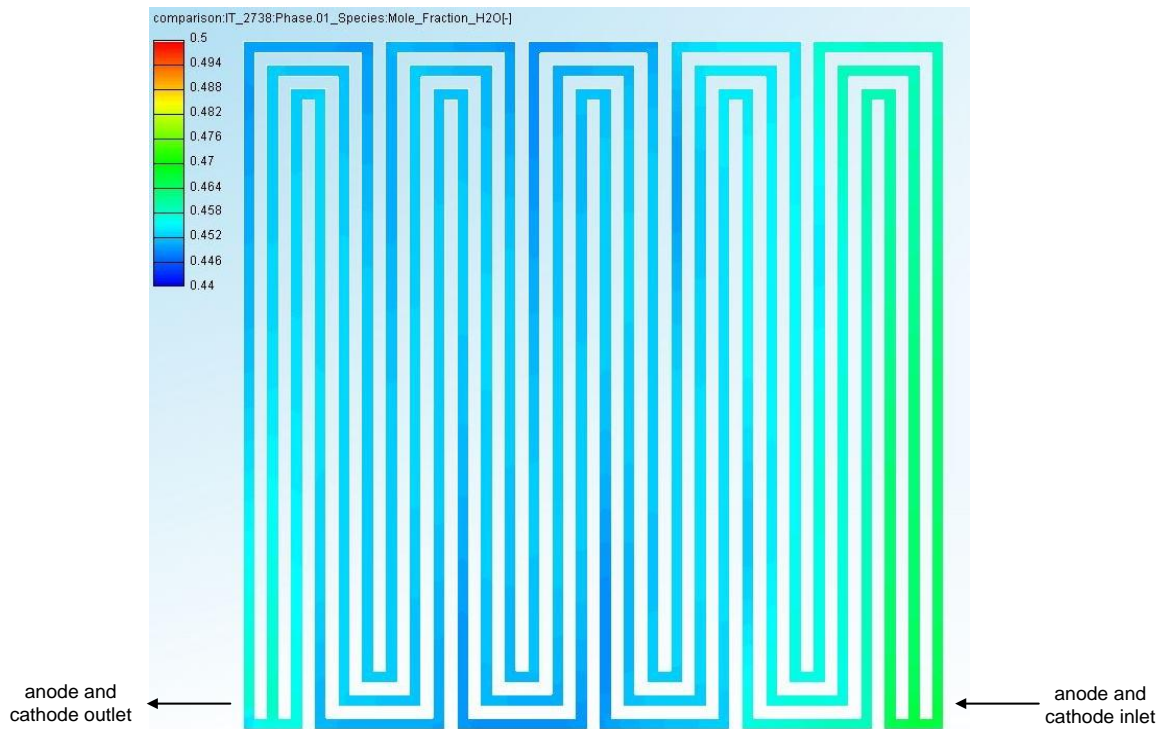
Figure 47: Distribution of the water mole fraction of the gaseous phase within the anode channel. Simulation results suggest that water mole fraction decreases on its way through the anode flow field.

Due to extended convergence, information shown in the Appendix (Figure 75 and Figure 76) the hypothesis is at hand that the decrease of water represents a convergence issue. As the total amount of water is not converged yet, the decrease of water in the feed stream may be led back to an increase of water within the membrane. Assumptions are that if the total water amount reaches steady state in terms of numerical convergence, the membrane water content shows steady state too. Then, the membrane does not take up water from the humidified feed stream any more. Thus, the water partial pressure is not reduced within the anode flow channel and therefore the hydrogen content does not increase on its way through the flow field.

5.4.5.2. Cathode Flow Field

The cathode flow field is fed with synthetic air consisting of 21 mol% oxygen and 79 mol% nitrogen. Due to humidification with water, these values are lowered. Figure 48 shows the distribution of oxygen mole fraction within the cathode channel. Contrary to Figure 46, a clear decrease of oxygen mole fraction can be found, which is reasonable. Thus, the simulation results suggest a decrease of oxygen concentration along the flow field channels.

However, when regarding Figure 48, focus needs to on the color bar. As visible, the differences shown are small. They are kept within the range of 1 % of mole fraction. Anyway, the simulation

results predict a slight decrease of oxygen. Assumptions are that this is caused by the consumption of oxygen due to the electrochemical reaction.

Furthermore, the oxygen distribution shows convergence issues same as the hydrogen distribution discussed above. The areas illustrating locally increased oxygen mole fractions are likely to decrease in intensity or to vanish at higher iteration numbers.
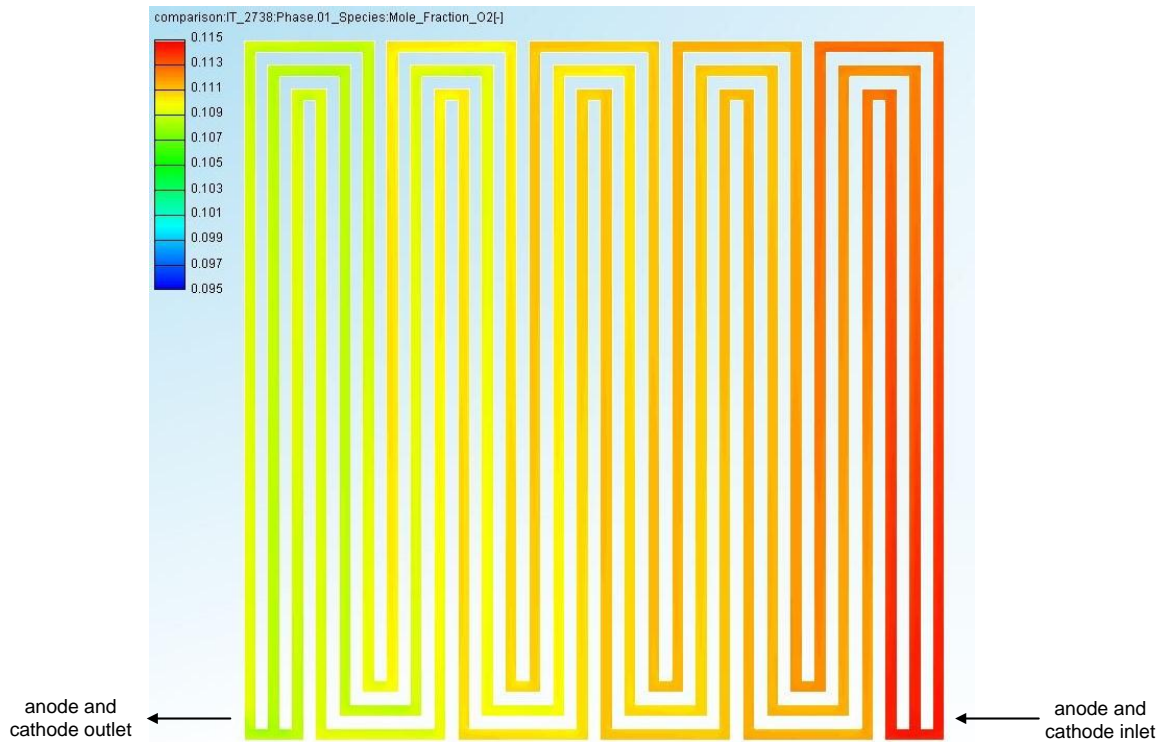
Figure 48: Distribution of the oxygen mole fraction of the gaseous phase within the cathode channel. Simulation results suggest a decrease of oxygen due to the electrochemical reaction.

As discussed within the anode flow field section, the total water amount does not show sufficient convergence; therefore statements are afflicted with uncertainty. However, Figure 49 supposes the water content of the cathode channel gas tends to decrease on its way through the flow field. Especially the lower half of the flow field exhibits decreased water content. The fact that gradients are still high is likely to rest on the water convergence issues mentioned above. However, trends lead to the assumption that the membrane is still taking up gaseous water. This phenomenon is equivalent to the description in chapter 5.4.5.1 discussing the anode gas flow.

In this context, it is important to be noted that no condensation of water does occur in relevant extent, neither at the anode side nor at the cathode side. Due to the water absorption of the membrane one can suppose that steady state of the cell simulated is not reached yet. This assumption is supported by the convergence of the total amount of liquid water in the Appendix (Figure 76).
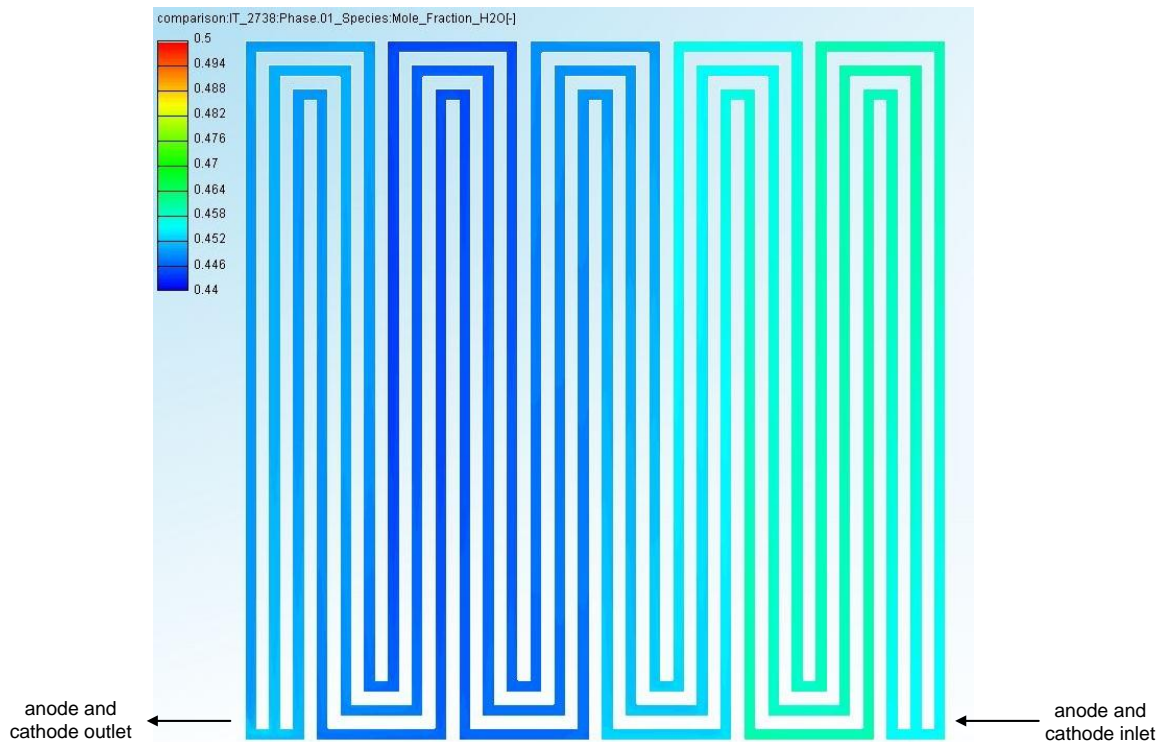
Figure 49: Distribution of the gaseous water mole fraction of the gaseous phase within the cathode channel. The simulation results suggest a decrease of gaseous water on the gas flows way through the cathode flow field.

Considering the fact that the amount of nitrogen within the channel is not affected, the conclusion of the findings presented above is clear: The overall decay of oxygen illustrated in Figure 48 is not depending on convergence issues. Thus, the simulation results support the assumption that a decrease of oxygen within the cathode channel flow due to electrochemical consumption is present. Anyway, the absolute differences to be observed are small.

Summarized, the distributions of water mole fractions in both anode and cathode channel show no sufficient convergence yet. Thus, statements concerning the trend of the hydrogen concentration within the anode flow field are not plausible. However, results observing the oxygen concentration within the cathode flow field suppose that an oxygen decrease due to electrochemical reaction consumption is present. This consumption influences the variation of oxygen amount within the flow field in the range of 1 mol%.

Thus, the results gained investigating the reaction current density by means of AVL FIRE may be depending on this relationship. However, the influences of decreasing reaction partner concentration within the anode and cathode channel are expected to have minor influence concerning the reaction current and overall fuel cell performance, as the decrease is very low in this specific case. Effects resulting from surrounding restrictions and disturbances, as discussed in chapter 5.4.4, are expected to influence results from laboratory and CFD simulation more strongly.

6. Conclusion

The aim of this thesis is to validate single cell modelling by means of AVL FIRE. Even though the meshing process is complex and extensive, the numerical simulations show satisfying results for multiple parameters. However, an adaption to the special operation conditions of the fuel cell examined is a necessity for extended use.

As shown within this thesis, the meshing of the fuel cell investigated is strongly influencing the results of the calculation. Not only mesh geometry and the arrangement of the fuel cell parts but also the mesh size and cell distribution need to be regarded as critical factors. This is particularly the case when computational resources are low. The calculation progress in terms of iteration numbers strongly affect the quality of results received. Furthermore, electrochemical reaction parameters need to be considered. As the calculation depends on these parameters, ideally a set of parameters is available for different MEA constructions to improve validity of the simulation results. The task to develop a reliable set of material and electrochemical parameters is critical. Extensive investigations concerning the parameters' impact on the mathematical model underlying are expected to be a complex enterprise.

However, the quality of the experimental procedure and materials used for the laboratory investigation are influencing the comparability as well. As shown within this thesis, two different laboratory testing series exhibit different comparability to FIRE simulation results. Further investigations concerning the quality of CFD approaches are wise in order to improve the comparability with laboratory examination results.

The qualitative comparison of spatial distribution characteristics within the fuel cell observed shows conformity regarding basic fuel cell issues. Striking is the match of overall reaction current density. Contrary to this finding is the distribution of reaction current densities. While the CFD simulation suggests higher reaction current densities next to the anode and cathode inlet, the laboratory investigation shows reverse results. Furthermore, current distribution recorded during laboratory examination shows more homogeneity than the CFD simulation results. In this context, the environment of the fuel cell needs to be taken into account. While the CFD simulation is conducted by means of ideal conditions, the laboratory examination has to face influences of real operation conditions. Also the location of measurement may influence the results. The CFD simulation accesses the catalyst layer itself while laboratory examination can only take hold of the distribution after the flow field plate and therefore records an altered current density distribution due to cross current fluxes within the bipolar plate. Nevertheless, differences are kept low and both investigations show current densities within a range of 1000 A m^{-2} to 1200 A m^{-2} for the bigger part.

The examined temperature distributions show very similar results. This conclusion is based on the fact that both the CFD simulation as well as at the fuel cell examined in the laboratory exhibit continuous heating elements. While the channel wall temperature of the FIRE model is set fixed, the cell investigated in the laboratory contains electrical heating across the flat side of the bipolar plate.

The investigation of the reactant flows shows different findings. On one hand, the anode flow field channel exhibits gaseous water content convergence issues. Thus, statements concerning the influence of reaction consumption on hydrogen content distribution lack meaningfulness. On the other hand, the oxygen partial pressure shows a decrease in the cathode flow field. Gaseous water content convergence issues are present too, but the nitrogen content of the air acts as damping media, reducing influences to the oxygen mole fraction. Therefore, CFD simulation results support the decrease of oxygen within the cathode flow field due to electrochemical reaction consumption. Still, the impact is kept within the range of 1 mol% and therefore the effect on the overall fuel cell performance is assumed as being not significant.

AVL FIRE represents an extensive tool to model PEM fuel cell operation conditions. Next to temperature characteristics, also current density distribution within the MEA is modelled. Additional parameters like hydrogen and oxygen mole fraction as well as water mole fraction are calculated based on the modelled operating conditions.

References

[1]   T. Hamacher, "Wasserstoff als strategischer Sekundärenergieträger," in *Wasserstoff und Brennstoffzelle*, 2014, pp. 5–10.

[2]   J. Randers, "2052 - eine globale Prognose für die nächsten 40 Jahre," Chelsea Green Publishing, 2012, pp. 315–319.

[3]   V. Hacker, "Lecture Notes Fuel Cells and Energy Storage, Institue of Chemical Engineering and Environmental Technology, University of Technology Graz," 2016.

[4]   J. Garche, C. Dyer, P. Moseley, Z. Ogumi, D. Rand, and B. Scrosati, *Encyclopedia of Electrochemical Power Sources*. Elsevir B.V., 2009.

[5]   T. Seilnacht, "Brennstoffzellen als Energiewandler," 2016. [Online]. Available: http://www.seilnacht.com/Lexikon/bzellen.html.

[6]   V. Hacker, A. Schenk, S. Mitsushima, A. Takuto, and K. Ota, "Advanced Studies of Polymer Electrolyte Fuel Cells," 2016, pp. 86–103.

[7]   B. Hebenstreit, *Entwicklung und Charakterisierung eines Brennstoffzellenstapels*. Technische Universität Graz, 2007.

[8]   Lilium Energy, "Lilium Energy - Hydrogen Fuel Cells," 2016. [Online]. Available: http://liliumco.com/fuel_cells.php.

[9]   M. Klingele, M. Breitwieser, R. Zengerle, and S. Thiele, "Direct deposition of proton exchange membranes enabling high performance hydrogen fuel cells," 2015. [Online]. Available: http://pubs.rsc.org/en/content/articlehtml/2015/ta/c5ta01341k.

[10]   L. Cindrella, A. M. Kannan, J. F. Lin, K. Saminathan, Y. Ho, C. W. Lin, and J. Wertz, "Gas diffusion layer for proton exchange membrane fuel cells-A review," *J. Power Sources*, vol. 194, no. 1, pp. 146–160, 2009.

[11]   X. Li and I. Sabir, "Review of bipolar plates in PEM fuel cells: Flow-field designs," *Int. J. Hydrogen Energy*, vol. 30, pp. 359–371, 2005.

[12]   H. Dolmetsch, D. Holznagel, E. Keller, R. Kilgus, and W. Klein, "Metalltechnik Fachbildung - Der Werkzeugbau," Verlag Europa Lehrmittel, 2007, pp. 72–87.

[13]   M. I. M. Isa and A. A. Aziz, "Optimized flow field bipolar plate design in Proton Exchange Membrane Fuel Cell," *2012 10th IEEE Int. Conf. Semicond. Electron.*, 2012.

[14]   Can, "PEM-Brennstoffzellen mit spritzgegossenen Bipolarplatten aus hochgefülltem Graphit-Compound," 2008, pp. 1–59.

[15]   V. Hacker, M. Bodner, and A. Schenk, "Integration of a Membrane Reactor with a Fuel Cell for Inclusion in Integrated Membrane Systems and Processes," in *Integrated Membrane Systems and Processes*, John Wiley & Sons, 2016, p. 298.

[16]   B. Her, S. Hsieh, and J. Chen, "Channel-to-Rib Width Ratio Effects of Flowfield Plates in the Performance of a Micro-PEM Fuel Cell Stack," *NSTI-Nanotech 2009*, vol. 3, pp. 103–106,

2009.

[17] Y.-G. Yoon, W. Y. Lee, G.-G. Park, and C.-S. Kim, "Effects of channel and rib widths of flow field plates on the performance of a PEMFC," *Int. J. Hydrogen Energy*, vol. 30, pp. 1363–1366, 2005.

[18] W. Kümmel, "Stationäre Strömung inkompressibler Fluide," in *Technische Strömungsmechanik - Theorie und Praxis*, Teubner Verlag, 2007, pp. 94–153.

[19] J. Khinast, "Zur Mehrphasigkeit - Stoffübergang an festen überströmten Grenzflächen," in *Vorlesungsskriptum Stoffübertragung, Institut für Prozess und Partikeltechnik, Technische Universität Graz*, 2014, pp. 80–113.

[20] N. Konno, S. Mizuno, H. Nakaji, and Y. Ishikawa, "Development of Compact and High-Performance Fuel Cell Stack," *SAE Int. J. Altern. Powertrains*, vol. 4, 2015.

[21] YouTube, "2016 Toyota Mirai FCV - Fuel Cell Stack," 2014. [Online]. Available: https://www.youtube.com/watch?v=KoOXviTSAtA.

[22] H. Yumiya, M. Kizaki, and H. Asai, "Toyota Fuel Cell System," in *International Electric Vehicle Symposium and Exhibition*, 2015, no. December 2014, pp. 1–8.

[23] T. Yoshida and K. Kojima, "Toyota MIRAI Fuel Cell Vehicle and Progress Toward a Future Hydrogen Society," *Electrochem. Soc. Interface*, pp. 45–49, 2015.

[24] A. Bendzulla, "Von der Komponente zum Stack : Entwicklung und Auslegung von HT-PEFC-Stacks der 5 kW-Klasse," *Schriften des Forschungszentrums Jülich*, vol. 69, 2010.

[25] W. Haas, "Grundlehrgang Dichtungstechnik," *Universität Stuttgart*, pp. 1–3, 2016.

[26] W. Gohl and K. Spies, "Dichtungen für ruhende Flächen," in *Elastomere - Dicht- und Konstruktionswerkstoffe*, expert Verlag, 2003, pp. 231–249.

[27] K. Rinortner, "Dichtungen - wärmeableitend und leitfähig," 2016. [Online]. Available: http://www.elektronikpraxis.vogel.de/waermemanagement/articles/522198/.

[28] M. Wannert, "Stabile Algorithmen für die Magnetotomographie an Brennstoffzellen," *Schriften des Forschungszentrums Jülich*, vol. 64, p. 44, 2010.

[29] ubuntuusers, "CFD-Strömungssimulation," 2016. [Online]. Available: https://wiki.ubuntuusers.de/CFD_-_Strömungssimulation/.

[30] AVL List GmbH, "AST Documentation: Workflow Manager," *AVL FIRE Version 2014.2*, 2016.

[31] AVL List GmbH, "Flexible Automated Meshing Environment," *AVL Homepage AVL FIRE*, 2016. [Online]. Available: https://www.avl.com/fire2/-/asset_publisher/gYjUpY19vEA8/content/avl-fire-fame.

[32] AVL List GmbH, "FIRE Solver, AST Documentation," 2016.

[33] G. B. Wallis, *One-dimensional two-phase flow*. Mcgraw-Hill, 1969.

[34] AVL List GmbH, "Eularian Muliphase," *AVL FIRE Version 2014.2*, pp. 4–1, 2016.

[35] AVL List GmbH, "Porosity Module," *AVL FIRE Version 2014*, 2014.

[36] AVL List GmbH, "Species Transport Module," *AVL FIRE Version 2014*, 2014.

[37] AVL List GmbH, "Electrification/Hybridization," *AVL FIRE Version 2014.2*, 2016.

[38] AVL List GmbH, "IMPRESS 3D for FIRE," *AVL FIRE Version 2014.2*, 2016.

[39]   A. Böge and W. Böge, "Maschinenelemente - Schraubverbindungen," in *Handbuch Maschinenbau*, 2009, pp. I66–I89.

[40]   "Tabellensammlung Chemie/Stoffdaten Wasser," 2016. [Online]. Available: https://de.wikibooks.org/wiki/Tabellensammlung_Chemie/_Stoffdaten_Wasser.

[41]   AVL List GmbH, "FIRE Basic Training Course, Module Tutorial Electification/Hybridization: Fuel Cell," *AVL Adv. Simul. Technol. Softw. Train.*, 2014.

[42]   A. Leder, "Grundlagen der Strömungsmechanik - Vorlesungsumdruck mit Tabellen und Diagrammen sowie Übungsaufgaben und Praktikumsanleitungen," p. 7.

[43]   K. Avila, D. Moxey, M. Avila, A. de Lozar, and B. Hof, "Onset of Turbulence in Pipe Flows," 2011. [Online]. Available: http://homepages.warwick.ac.uk/~masax/Research/ critical_point_pipe_flow/critical_point_pipe_flow.html.

[44]   J. P. Joule and W. Thomson, "On the thermal effects experienced by air in rushing through small apertures," *Philos. Mag.*, vol. 4, no. 284, pp. 481–492, 1852.

List of Abbreviations

AMG	Algebraic multigrid method
CAD	Computer aided drawing
CCM	catalyst-coated membrane
CFD	computational fluid dynamics
CGJP	conjugated gradient algorithm
Cl	catalyst layer
FAME	Flexible Automated Meshing Environment
GDL	gas diffusion layer
LES	Large eddy simulation
MEA	membrane electrode assembly
mio.	Million
PANS	partially averaged Navier-Stokes
PEEK	Polyether ether ketone
PEM	Polymer electrolyte membrane
PEMFC	Proton exchange membrane fuel cell, Polymer electrolyte membrane fuel cell
PFA	Perfluoroalkoxy alkane
PI	Polyimide
PTFE	Polytetrafluoroethylene
SSF	Solver steering file

List of Figures

List of Tables

List of Formulae

Appendix

Laboratory Equipment

Hardware
Test rig; Institute of Chemical Engineering and Environmental Technologies - Fuel Cell Group
Zahner electrochemical workstation IM6ex
Zahner power potentiostat PP240
S++ current scan shunt 10x10

Table 18: Hardware used for the laboratory investigation of the observed fuel cell.

Software
LabVIEW 2012
Thales software package

Table 19: Software used for the laboratory investigation of the observed fuel cell.

Laboratory Operation Conditions Summary

Laboratory operation conditions summary	
Type of fuel cell	PEMFC
Active area	50 mm x 50 mm
Bipolar plate type	Milled from graphite plate
Cell operation pressure	1 atm
Anode feed	Hydrogen, pure, 500 Nml min^{-1}
Cathode feed	Synthetic air, 1000 Nml min^{-1} 20.9 mol% Oxygen 79.1 mol% Nitrogen
Polarization curve investigation	
Cell operation temperature	70 °C
Temperature anode and cathode feed	75 °C
Relative humidity of anode and cathode feed	0.9 at 70 °C
Membrane	QuinTech CCM-H25-N212
Gas diffusion layer	SIGRACET® Gas Diffusion Media, Type GDL 35 BC
Gasket	PTFE textile flat gasket
Spatial distribution investigation	
Cell operation temperature	80 °C
Temperature anode and cathode feed	85 °C
Dew point anode and cathode feed	80 °C
Membrane	Nafion® XL
Gas diffusion layer	SIGRACET® Gas Diffusion Media, Type GDL 24 BC
Gasket	PTFE textile flat gasket
Operational voltage	800 mV

Table 20: Operation conditions of the fuel cell polarization curve investigation as well as the spatial distribution investigation.

CFD Mesh - Selections Description

To copy the single cell mesh shown in this thesis in AVL FIRE, the required selections are shown. Their use ensures a converging calculation.

Face Selections

	Selection name	BC type	Phase ID	Inherent characteristics	Temperature	Mole fractions
Inlet & outlet boundary conditions	Ano_In	Inlet/Outlet - *mass flow*	1	5.807e-7 kg s^{-1}	348.15 K	H2: 1.00
			2	0	-	-
			3	0	-	-
	Cat_In	Inlet/Outlet - *mass flow*	1	1.667e-5 kg s^{-1}	348.15 K	O2: 0.21 N2: 0.79
			2	0	-	-
			3	0	-	-
	Ano_Out	Inlet/Outlet - *static pressure*	1	101325 Pa	-	H2: 1.00
			2	-	-	-
			3	-	-	-
	Cat_Out	Inlet/Outlet - *static pressure*	1	101325 Pa	-	O2: 0.21 N2: 0.79
			2	-	-	-
			3	-	-	-

Table 21: Face selections required to define inlet and outlet boundary conditions at the fuel cell mesh.

	Selection name	BC type	Velocity u, v, w	Temperature/Heat Flux	Field/Potential	Contact resistance
Wall boundary conditions	FC_BP	Wall - *Thermal: Temperature Electric: Field*	0 m s^{-1}	343.15 K	0 V m^{-1}	0 Vm² A^{-1}
	Ano_BP_GDL	Wall - *Thermal: Temperature Electric: Potential*	0 m s^{-1}	343.15 K	0 V	0 Vm² A^{-1}
	Cat_BP_GDL	Wall - *Thermal: Temperature Electric: Potential*	0 m s^{-1}	343.15 K	x V*	0 Vm² A^{-1}
	ZHF1	Wall - *Thermal: Heat Flux Electric: Field*	0 m s^{-1}	0 W m^{-2}	0 V m^{-1}	0 Vm² A^{-1}
	ZEF	Wall - *Thermal: Heat Flux Electric: Field*	0 m s^{-1}	0 W m^{-2}	0 V m^{-1}	0 Vm² A^{-1}

 * voltage depending on the working point

Table 22: Face selections required to define wall boundary conditions at the fuel cell mesh.

	Selection name	Description
Arbitrary connection within anode and cathode GDL	arbi_ano_fine_2	Counterpart of *arbi_gdl_anode_2.* Interface within the anode GDL. Belongs to the fine mesh part of the anode GDL.
	arbi_cat_fine_2	Counterpart of *arbi_gdl_cathode_2.* Interface within the cathode GDL. Belongs to the fine mesh part of the cathode GDL.
	arbi_gdl_anode_2	Counterpart of *arbi_ano_fine_2.* Interface within the anode GDL. Belongs to the coarse mesh part of the anode GDL.
	arbi_gdl_cathode_2	Counterpart of *arbi_cat_fine_2.* Interface within the cathode GDL. Belongs to the coarse mesh part of the cathode GDL.
Arbitrary connection between serpentine flow field mesh and inlet tubes	arbi_channel_ano_in	Counterpart of *arbi_cyl_ano_in.* Interface between the serpentine flow field mesh and the inlet flow tube of the anode inlet.
	arbi_channel_ano_out	Counterpart of *arbi_cyl_ano_out.* Interface between the serpentine flow field mesh and the inlet flow tube of the anode outlet.
	arbi_channel_cat_in	Counterpart of *arbi_cyl_cat_in.* Interface between the serpentine flow field mesh and the inlet flow tube of the cathode inlet.
	arbi_channel_cat_out	Counterpart of *arbi_cyl_cat_out.* Interface between the serpentine flow field mesh and the inlet flow tube of the cathode outlet.
	arbi_cyl_ano_in	Counterpart of *arbi_channel_ano_in.* Interface between the serpentine flow field mesh and the inlet flow tube of the anode inlet.
	arbi_cyl_ano_out	Counterpart of *arbi_channel_ano_out.* Interface between the serpentine flow field mesh and the inlet flow tube of the anode outlet.
	arbi_cyl_cat_in	Counterpart of *arbi_channel_cat_in.* Interface between the serpentine flow field mesh and the inlet flow tube of the cathode inlet.
	arbi_cyl_cat_out	Counterpart of *arbi_cyl_channel_out.* Interface between the serpentine flow field mesh and the inlet flow tube of the cathode outlet.

Table 23: Face selections required to define arbitrary connections to join the final fuel cell mesh.

Cell Selections

	Selection name	Description
Fuel Cell Module essential parts	Anode_Channel	Channel cell selection for the region definition of the anode input of the Fuel Cell Module
	Cathode_Channel	Channel cell selection for the region definition of the cathode input of the Fuel Cell Module
	Ano_GDL	Gas diffusion layer cell selection for the region definition of the anode input of the Fuel Cell Module
	Cat_GDL	Gas diffusion layer cell selection for the region definition of the cathode input of the Fuel Cell Module
	membrane	Membrane cell selection for the region definition of the Fuel Cell Module

Table 24: Cell selections required to define the essential parts of the fuel cell mesh for use within the Fuel Cell Module.

	Selection name	Description
Output	Ano_RL	Layer cell selection within the anode GDL for the anode output of 2D-Results.
	Cat_RL	Layer cell selection within the cathode GDL for the cathode output of 2D-Results.

Table 25: Cell selections required for output of electrical values (for instance reaction current density) of the fuel cell simulation.

CFD Mesh - Selections Illustration

For reverse engineering of the single cell mesh shown in this thesis in AVL FIRE, subsequently the assignment of the used selections to the mesh is shown.

Face Selections
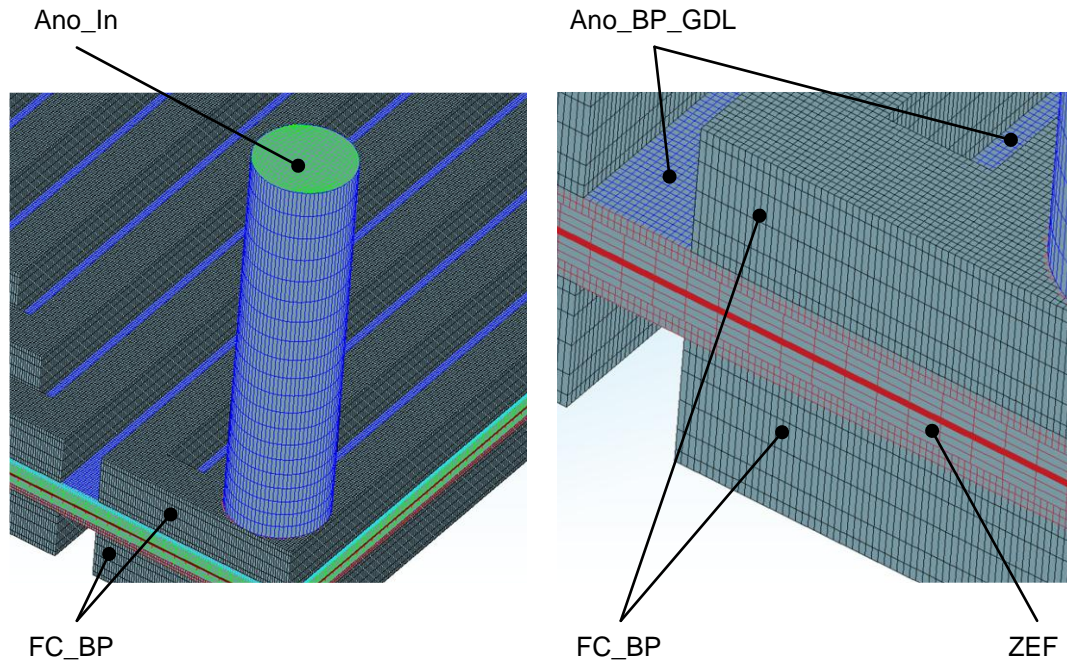
Figure 50: *Ano_In* (green) represents the inlet and outlet boundary conditions (left). *FC_BP* (black) is the channel surface resulting from the bipolar plate flow field. The electrical contact of MEA and bipolar plate is illustrated by *Ano_BP_GDL* (blue). It is the equivalent of *Cat_BP_GDL*. All layers of the MEA are enclosed by *ZEF* (red) (right).

ZHF1   ZHF1
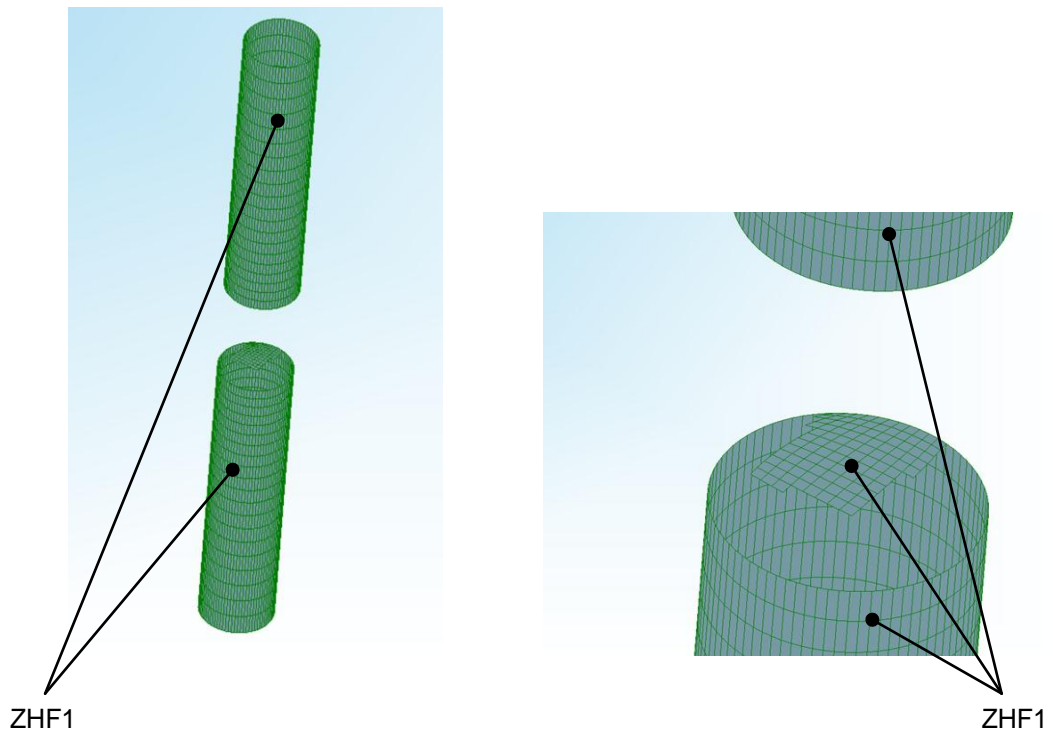
Figure 51: The inlet and outlet tubes are wrapped by *ZHF1* (green). When designing the interface of the tubes to the serpentine flow field, those cell faces which do not connect to the inner of the flow field need to be considered (right).

Cat_GDL   arbi_cat_fine   arbi_gdl_cathode
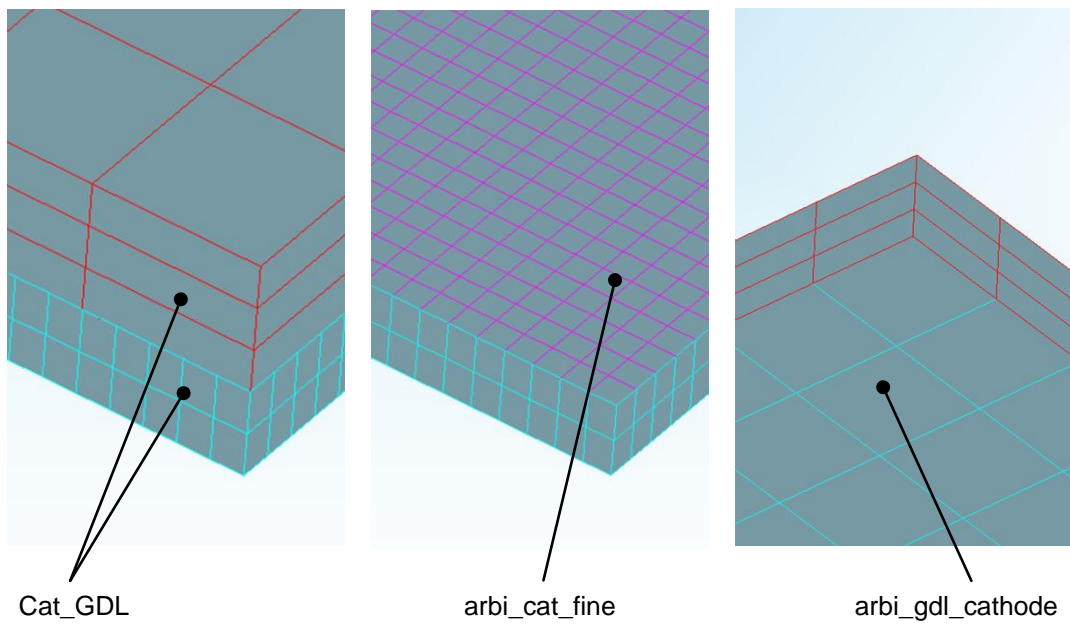
Figure 52: To assemble the two meshes of the *Cat_GDL* cell selection (left), two face selections are required. The fine mesh (light blue) exhibits *arbi_cat_fine* (magenta) (middle). The coarse mesh (red) needs to feature *arbi_gdl_cathode* (light blue) (right). The equivalent is true for *Ano_GDL* cell selection.

arbi_channel_ano_in   arbi_cyl_ano_in
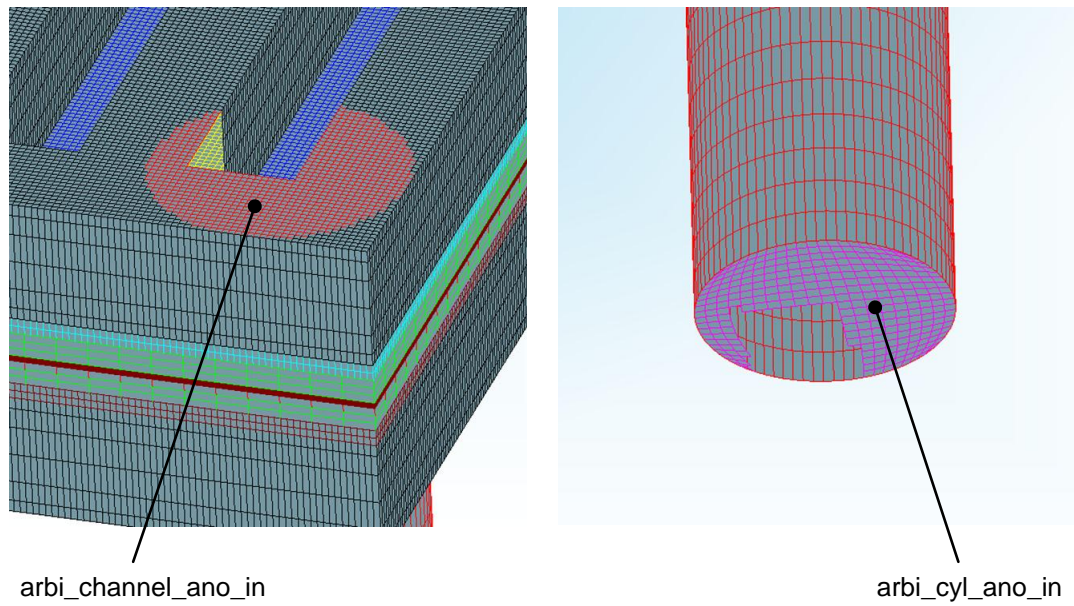
Figure 53: To join the inlet and outlet tubes to the serpentine flow field by means of Arbitrary Connect, the serpentine flow field mesh needs to exhibit face selections. At the anode inlet, *arbi_channel_ano_in* (red) is on the flow field mesh (left). The counterpart, *arbi_cyl_ano_in* (magenta), needs to be the inlet tube meshes (right). The equivalent is true for the remaining inlet tube connections.

Cell Selections
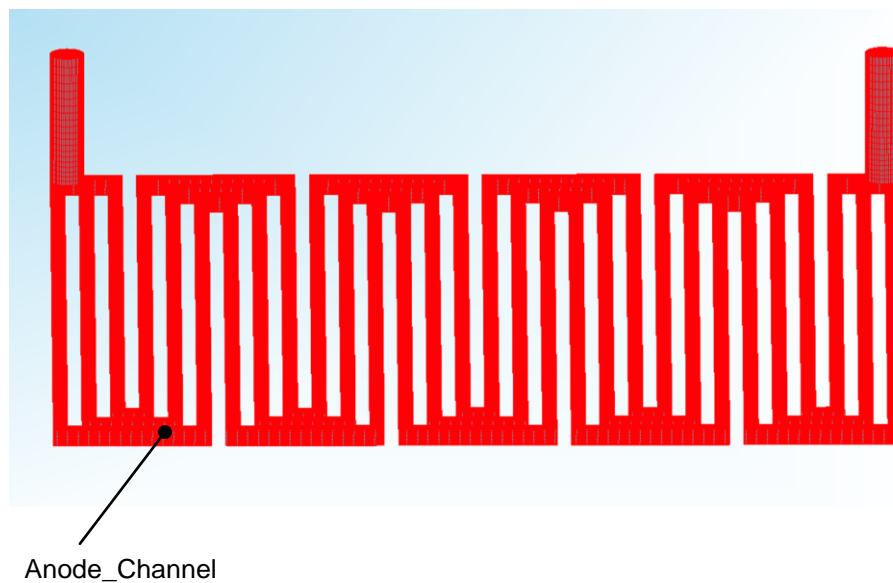
Anode_Channel

Figure 54: The *Anode_Channel* (red) cell selection consists of the serpentine flow field mesh as well as inlet and outlet tubes. The equivalent is true for the *Cathode_Channel* cell selection.
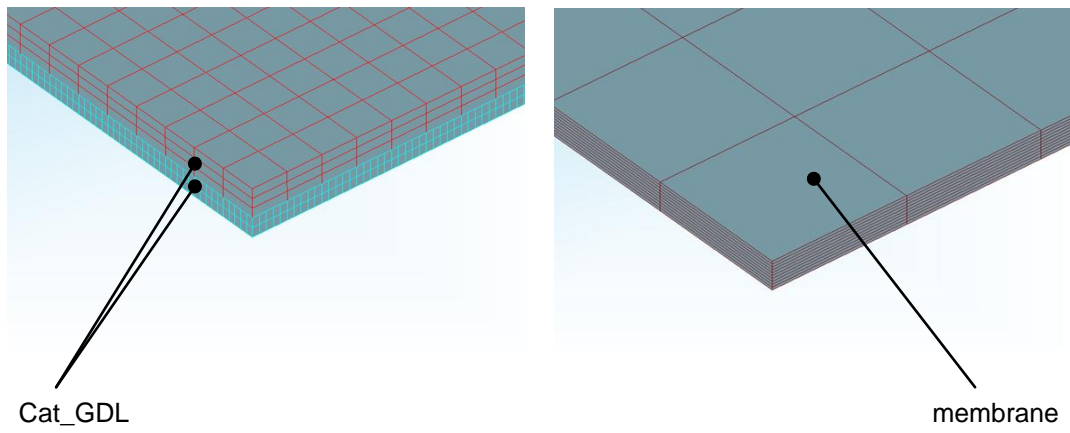
Cat_GDL   membrane

Figure 55: The *Cat_GDL* cell selection consists of two layers (light blue and red) joined by *Arbitrary Connect* (left). The equivalent is true for the *Ano_GDL* cell selection. The *membrane* (dark red) is a single layer (right)

Ano_RL   Ano_RL
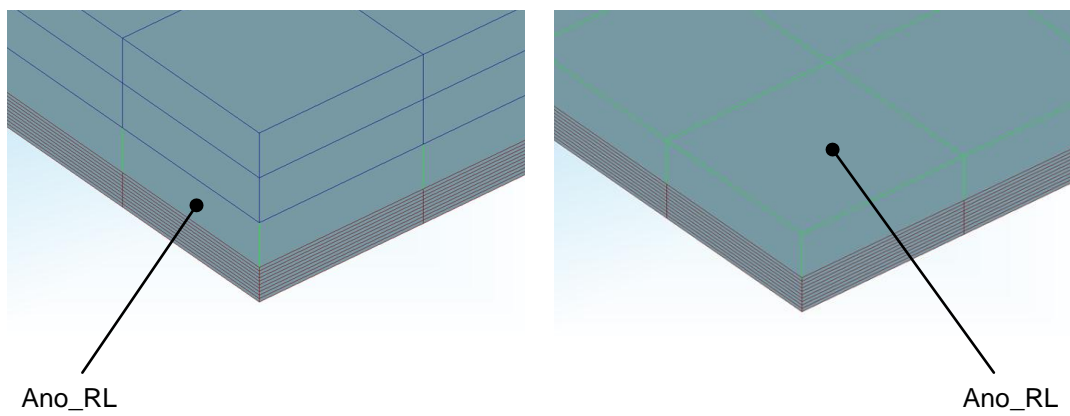
Figure 56: For extended output, a result cell selection layer needs to be included in the GDL. It is the first cell layer of the GDL next to the membrane. The *Ano_RL* cell selection is shown in green.

CFD Calculation - Solver Settings

Subsequent, the used solver settings for the examined fuel cell are presented. They are based on proposed settings of AVL for a fuel cell simulation [41] and adjusted to the case at hand.

Fluid Properties

	Phase ID		
	1	**2**	**3**
Aggregate state	Gas	Liquid	Solid
Density / kg m^{-3}	Ideal Gas	Database	2250
Molecular weight / kg kmol^{-1}	Database	Database	-
Specific heat / J kg^{-1}K^{-1}	Database	Database	720
Dynamic viscosity / Ns m^{-2}	Database	Database	-
Thermal conductivity / W m^{-1}K^{-1}	Database	Database	150.6 / isotropic
Electrical conductivity / A V^{-1}m^{-1}	-	-	500 / isotropic
Dielectric constant / -	-	-	0
Diffusion coefficient / m² s^{-1}	Database	Database	-
Thermodynamic database flag	Internal	-	-
Transport database flag	Internal	-	-

Table 26: The properties of O_2, N_2, H_2 as well as H_2O can be found in the FIRE database. The properties of the GDL material need to be defined manually.

Initial Conditions

	Phase ID		
	1	**2**	**3**
Pressure / Pa	101325	101325	101325
Temperature / K	343.15	343.15	343.15
Turbulent kinetic energy / m² s^{-2}	0.001	0.001	0.001
Turbulent length scale / m	0.001	0.001	0.001
Turbulent dissipation rate / m² s^{-3}	0.00519615	0.00519615	0.00519615
Velocity u, v, w / m s^{-1}	0	0	0
Volume fraction / -	1	1	1
Scalar	0	0	0
Mole fraction / -	O_2: 0.21 N_2: 0.79	H_2O: 1	-

Table 27: For fast convergence, the initial conditions are picturing the average cell condition at steady state.

Solver Control

Discretization	
Calculation of boundary values	Extrapolate
Calculation of derivatives	Least square sit
Variable limits	No
Cell quality check	No
Cell face adjustment - equation	No
Cell face adjustment - geometry	No
Realizability constraints	No
Artificial compressibility	No
Decoupled domains	No

Table 28: The discretization properties adapt the numerical characteristics to the individual challenge.

Activate Equations	
Momentum & Continuity	Yes
Volume fraction	Yes
Turbulence	Laminar
Energy	Yes
Enthalpy	Total enthalpy
Viscous heating	Yes
Pressure work	Yes
Scalar	No
Pressure reference cell	4989294
Two stage pressure correction	No
Compressibility	Weakly compressible
Wall treatment	Hybrid wall treatment
Heat transfer wall model	Standard wall function

Table 29: As the fuel cell module in FIRE cannot handle any turbulence model, laminar flow is assumed. The pressure reference cell is set at the *Ano_Out* boundary condition.

Underrelaxation factors			
	Phase ID		
	1	**2**	**3**
Momentum	0.2	0.2	0.6
Pressure	0.1	-	-
Turbulent kinetic energy	0.4	0.4	0.8
Turbulent dissipation rate	0.4	0.4	0.8
Energy	0.4	0.2	0.6
Mass source	1	-	-
Viscosity	1	1	1
Scalar	0.8	0.8	0.8
Species transport equations	0.8	0.8	-
Volume fraction	0.8	0.8	1
Electric potential	-	-	1

Table 30: The underrelaxation factors result from several experiments for speed optimization. To reach finer final residual convergence, the underrelaxation factors need to be decreased, especially in terms of momentum.

Differencing scheme	
Momentum	MINMOD Relaxed
Continuity	Central Differencing
Turbulence	Upwind
Energy	Upwind
Scalar	Upwind
Volume fraction	Upwind

Table 31: The setup of the differencing schemes is aligned to the recommended properties of AVL [41].

Linear solver				
	Linear solver type	**Min iteration**	**Max iteration**	**Tolerance**
Momentum	GSTB	0	50	0.1
Continuity	AMG	0	3000	0.005
Turbulence	GSTB	0	50	0.1
Energy	GSTB	0	50	0.1
Scalar	GSTB	0	500	0.1
Volume fraction	GSTB	0	500	0.005
Electric potential	AMG	0	500	0.00001

Table 32: The setup of the linear solvers is aligned to the recommended properties of AVL [41].

Porosity

Mesh requirements fulfilled	Yes
Porosity type	Undirected porosity
Volume fraction	0.78
Hydraulic diameter / m	0.0001
Relative turbulent length scale	0.01
Turbulence fixed	Yes
Pressure drop model	Forchheimer
Superficial velocity	Yes
Zeta value / m^{-1}	X=0, Y=0, Z=0
Alpha value / 1 m^{-2}	X=4.29*10^{11} Y=4.29*10^{11} Z=9.346*10^{13}
Relative permeability model	Muskat/Meres
Saturation exponent	3
Heat exchanger	Off
Capillary effects	On
Contact angle / °	122
Surface tension / N m^{-1}	0.072
Capillary pressure model	Leverett
Tortuosity model	Bruggeman
Bruggemann exponent	1.5
Knudsen diffusion	Off

Table 33: The porosity properties are vital for the characteristics of the GDL. The presented settings are true for the cell selections *Cat_GDL* and *Ano_GDL*.

Multiphase

Control	
Number of phases	3
Partial Elimination Algorithm (PEA)	No
Minimum volume fraction	$1*10^{-6}$

Phase specification		
Phase number	Porosity phase	VF equation not solved?
1	No	No
2	No	No
3	Yes	No

Table 34: For the present fuel cell simulation, three phases are required. Phase number 3 is porous as it represents the GDL of the MEA.

Mass interfacial exchange	
	Interface 1
Activation	Active
Continuous phase	1
Dispersive phase	2
Species	On
Model flag	Abramzon-Sirignano

Momentum interfacial exchange	
	Interface 1
Activation	Two-fluid
Continuous phase	1
Dispersive phase	2
Model flag	Gas-Liquid1

Table 35: Mass and momentum exchange is possible between the continuous phase 1 (gas phase) and the dispersive phase 2 (liquid phase).

Enthalpy interfacial exchange			
	Interface 1	**Interface 2**	**Interface 3**
Activation	Two-fluid	Two-fluid	Two-fluid
Continuous phase	1	1	2
Dispersive phase	2	3	3
Model flag	Abramzon-Sirignano	Wakao	Wakao

Table 36: Within the simulation, enthalpy can be exchanged between all three phases.

Species Transport

	Phase ID		
	1	**2**	**3**
Phase with species transport	Yes	Yes	Yes
Transport model	General	General	General
Number of species mass fractions	4 (O_2, N_2, H_2, H_2O)	4 (O_2, N_2, H_2, H_2O)	1 (H_2O)
Do not solve equation for species number	-	-	1
Scalar equation residual output	1	1	0
Multi-component diffusion	On	On	OFF

Table 37: To enable species transport within a phase, a transport model needs to be chosen and its properties to be defined.

Fuel Cell

Global settings	
Cell type	PEMFC
Membrane dimension	3D

Definition of regions		
Membrane	*membrane*	
	Positive (Cathode)	**Negative (Anode)**
Channel	*Cathode_Channel*	*Anode_Channel*
Channel inlet	*Cat_In*	*Ano_In*
Channel outlet	*Cat_Out*	*Ano_Out*
Gas diffusion layer	*Cat_GDL*	*Ano_GDL*
Electric inlet/outlet	*Cat_BP_GDL*	*Ano_BP_GDL*
Bipolar plate	-	-

Table 38: The Fuel Cell module requires the regions of the examined fuel cell to be defined. This is ensured appropriate cell selections.

Parameters and properties - Gas diffusion layer		
	Positive (Cathode)	**Negative (Anode)**
Anisotropic electrical conductivity	Yes	Yes
Electrical conductivity X / A $V^{-1}m^{-1}$	8486	8486
Electrical conductivity Y / A $V^{-1}m^{-1}$	8486	8486
Electrical conductivity Z / A $V^{-1}m^{-1}$	848.6	848.6
Anisotropic thermal conductivity	Yes	Yes
Thermal conductivity X / W $m^{-1}K^{-1}$	45.5	45.5
Thermal conductivity Y / W $m^{-1}K^{-1}$	45.5	45.5
Thermal conductivity Z / W $m^{-1}K^{-1}$	4.55	4.55

Table 39: The electrical and thermal conductivity of the GDL are assumed to be anisotropic. In-plane, the conductivities are assumed to be decreased for 90 %.

Parameters and properties - Membrane	
Sulfonic acid group concentration / kmol m^{-3}	1.9
Water diffusion coefficient / m^2 s^{-1}	2.683*10^{-11}
Reference temperature / K	298.15
Activation energy / kJ kmol^{-1}	19809
Ionic conductivity / A V^{-1}m^{-1}	5.368
Reference water concentration	20.0088
Critical water concentration	0
Percolation exponent	1
Reference temperature / K	298.15
Activation energy / kJ kmol^{-1}	9712.8
Electro-osmotic drag coefficient	0.108182
Reference temperature / K	298.15
Activation energy / kJ kmol^{-1}	7418
Thermal conductivity / W m^{-1}K^{-1}	0.67
Water sorption isotherm	FIRE
Critical relative humidity	0.97
Gas crossover	On
Henry constant / Pam^3 mol^{-1}	O_2: 19337.68 N_2: 19337.68 H_2: 4549.6 H_2O: 0
Diffusion coefficient in water / m^2 s^{-1}	O_2: 9.73083*10^{-11} N_2: 9.73083*10^{-11} H_2: 2.08768*10^{-10} H_2O: 0
Water convection	Off

Table 40: To characterize the membrane, several properties need to be defined.

Parameters and properties - Electrochemistry		
Open-circuit voltage / V	1.19	
Liquid coverage	On	
	Positive (Cathode)	Negative (Anode)
Reaction layer thickness / m	1.125*10^{-5}	1.125*10^{-5}
Cathodic transfer coefficient	0.45	0.25
Anodic transfer coefficient	0.05	0.25
Exchange current density / A m^{-2}	0.176	2.746*10^{6}
Oxygen exponent	0.775	-
Hydrogen exponent	0	0.25
Water exponent	0.45	-
Reference temperature / K	353.15	353.15
Activation energy / kJ kmol^{-1}	0	0

Table 41: To simulate the electrochemistry within the MEA, several properties need to be characterized.

Parameters and properties - Underrelaxation factors	
Volume fraction in GDL	0.01
Reaction current density	0.01
Membrane water flux	0.01

Table 42: For the simulation of the reaction mechanism enhanced underrelaxation factors are required.

Boundary/Initial conditions	
Cathode inlet velocity via stoichiometry	No
Anode inlet velocity via stoichiometry	No
Inlet H2O mass fractions via relative humidity	Yes
Cathode: Relative humidity	0.7276
Anode: Relative humidity	0.7276
Initial H2O mass fractions via relative humidity	Yes
Cathode: Relative humidity	0.7276
Anode: Relative humidity	0.7276

Table 43: Fuel cell characteristic parameters, such as gas inlet or relative humidity, can be defined in several ways. In the shown simulation, the inlet velocities are defined via the inlet mass flow of the global boundary conditions. The relative humidity is specified according to chapter 4.4.2.

Electromagnetics

	Phase ID		
	1	2	3
Electric potential	Off	Off	On
Magnetic potential	Off	Off	Off
Conductivity threshold / A Vm^{-1}	$1*10^{-6}$	$1*10^{-6}$	$1*10^{-6}$
Thermoelectric effects	Off	Off	Off

Table 44: To consider electromagnetic effects, the electric potential occurring in phase 3 needs to be considered.

Convergence of Polarization Plot Working Points Simulation

600 mV

Subsequently, the iteration behavior for the examined fuel cell at 600 mV is shown. The simulation was stopped by FIRE due to failure during the mesh decomposition process (C. Großegger, personal communication, 17.10.16) at iteration number 710. Due to this, the iteration behavior is regarded as not sufficient. Therefore, the iteration behavior shown is limited to the reaction current density, as it is used for the comparison to the laboratory examination results, as well as to the electrochemical reaction heat.

Figure 57: Reaction current density convergence behavior for 600 mV. The course of the reaction current density / A m^{-2} along the iteration number can be seen. At the last iteration, the reaction current density showed a value of 16006 A m².

Figure 58: Electrochemical reaction heat / W at 600 mV.

700mV

Subsequently, the iteration behavior for the examined fuel cell at 700 mV is shown. The simulation was finished manually at iteration number 1813.

Figure 59: Reaction current density convergence behavior for 700 mV. The course of the reaction current density / A m⁻² along the iteration number can be seen. At the last iteration, the reaction current density showed a value of 7916 A m⁻².

Figure 60: Electrochemical reaction heat / W at 700 mV. As expected, the reaction heat convergence is similar to the reaction current density convergence.
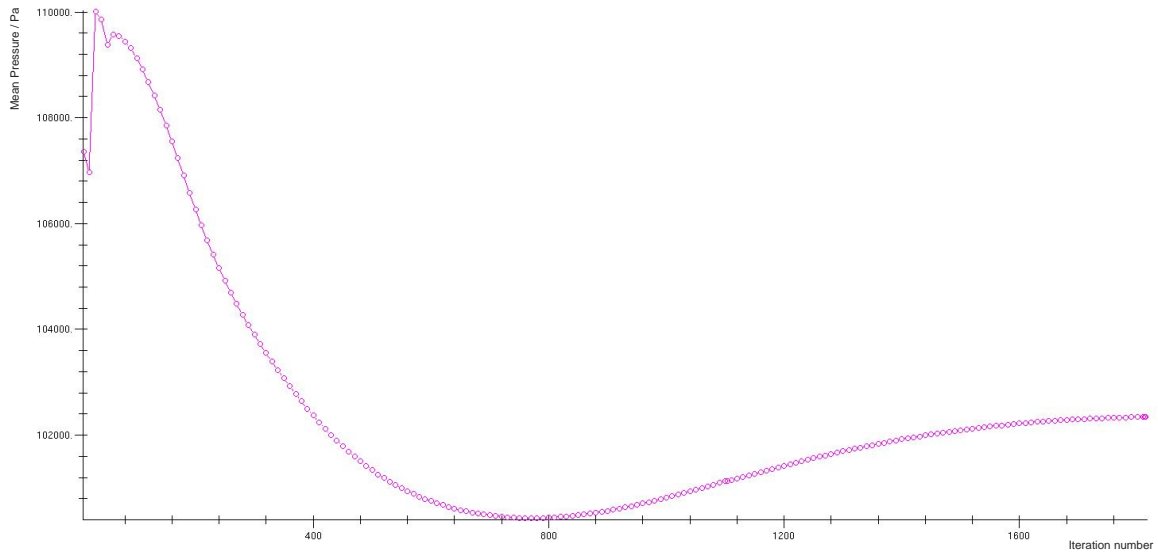
Figure 61: Pressure convergence behavior for 700 mV. The mean pressure / Pa within the fuel cell can be observed.
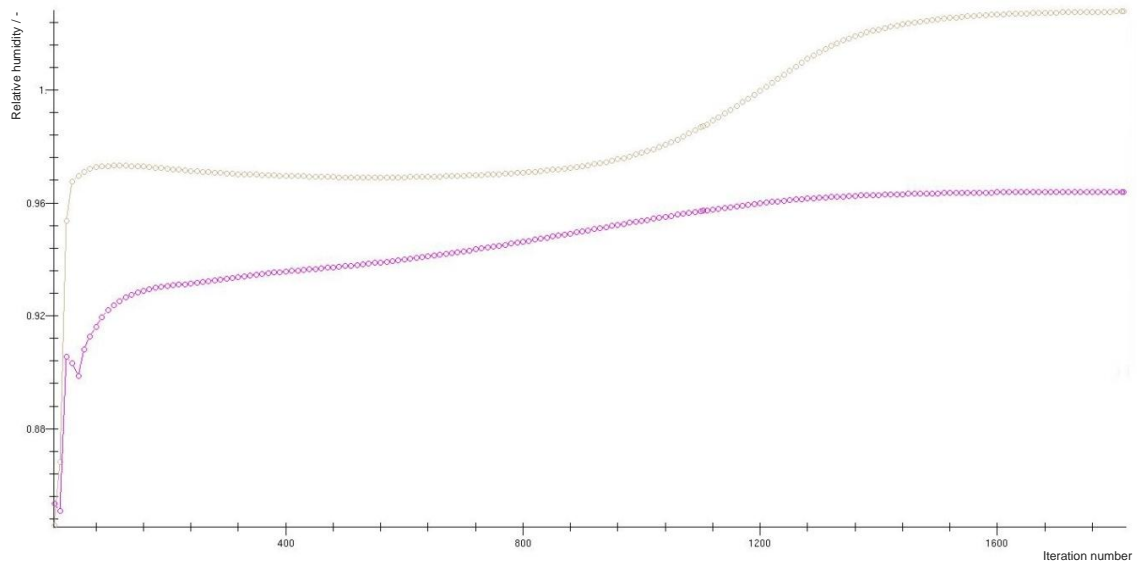
Figure 62: Relative humidity of the gas diffusion layer for the anode (magenta) and the cathode (light brown) at 700 mV. The observation takes place at the *Ano_RL* and *Cat_RL* cell selections. As shown above, they are defined as the cell layer of the anode and cathode GDL next to the membrane mesh. The relative humidity of the *Ano_RL* is shown in magenta, the relative humidity of the *Cat_Rl* is shown in light brown.

To discuss the raise of the *Cat_RL* relative humidity exceeding the value of 1, knowledge about FIRE´s mathematical descriptions to calculate the local relative humidity is required. The observed GDL section is modelled as a porous media, which may affect the definition of the relative humidity. However, the rise of the *Cat_RL* relative humidity can be found to be related to the total liquid water mass as shown in Figure 63. Enhanced investigations require prolonged calculation time until the fuel cell reaches quasi-steady state behavior concerning the liquid water phase.
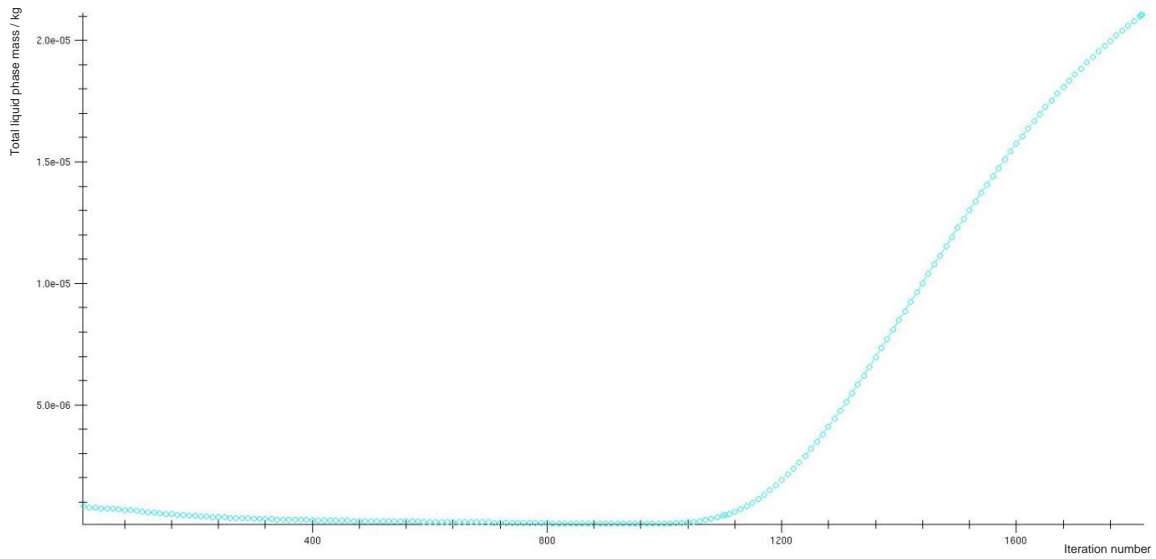
Figure 63: Total mass of liquid water phase / kg at 700 mV within the fuel cell.

As discussed above, more iterations are required until quasi-steady state is reached in order to investigate the causes of the liquid water phase behavior. However, based on information concerning the condensation rate as shown in Figure 64, further relations become obvious. Therefore, one can assume that the rise of relative humidity within the cathode GDL is depending on the condensation of gaseous water within the fuel cell.

Figure 64: Condensation rate / kg s^{-1} of gaseous water to liquid phase at 700 mV.

```
********************************************************************************************
*                                                                                         *
*    RUNTIME ANALYSIS AT END OF CALCULATION                                               *
*                                                                                         *
********************************************************************************************
*    Total MPI Timings              Count      Total CPU Time       Average WCT           *
********************************************************************************************
*    ACCIF_EXCHANGE                  44411               0.57              0.03           *
*    CpTempCalc                     176680            1682.94             90.74           *
*    Energy                          66240         1100779.62          58868.01           *
*    File IO                        122460           34681.75           3851.23           *
*    Mesh time update                22080             164.89              9.19           *
*    Momentum                        44160          726421.06          38877.21           *
*    Other                              20         4277288.50         286733.47           *
*    Pressure                        22080         4059484.25         246790.33           *
*    TherChem                      1991580          627586.25          33617.12           *
*    VolFrac                         44160          300886.75          16225.39           *
********************************************************************************************
*    Total Execution                    20        11130981.00         685300.81           *
********************************************************************************************


********************************************************************************************
*                                                                                         *
*    RUNTIME ANALYSIS AT END OF CALCULATION                                               *
*                                                                                         *
********************************************************************************************
*    Total MPI Timings              Count      Total CPU Time       Average WCT           *
********************************************************************************************
*    ACCIF_EXCHANGE                  28532               0.29              0.01           *
*    CpTempCalc                     113320             915.40             47.80           *
*    Energy                          42480          705464.62          36629.62           *
*    File IO                         81160           34107.59           4834.21           *
*    Mesh time update                14160             124.94              6.68           *
*    Momentum                        28320          457122.47          23761.99           *
*    Other                              20         2326438.25         135283.09           *
*    Pressure                        14160         1483934.50          90550.74           *
*    TherChem                      1281980          379793.47          19739.12           *
*    VolFrac                         28320          188431.02           9801.65           *
********************************************************************************************
*    Total Execution                    20         5576948.50         320742.19           *
********************************************************************************************
```

Figure 65: Runtime analysis for the calculation at 700 mV. As the calculation has been interrupted and restarted once, two separate analyses exist. The Average Wall Clock Time (Average WCT) shows the calculation time required / s. The sum of both total executions is 1006072 s. This value correlates to 279.5 h or 11.6 d. As can be seen the most calculation time is required for "Pressure" (approx..34 %) and "Other" (approx. 42 %). The calculations realized by the Fuel Cell Module containing the electrochemical reaction mechanisms are categorized as "Other". Experimentation and optimization of the underrelaxation factors in question may lead to diminished calculation time.

800mV

Subsequently, the iteration behavior for the examined fuel cell at 800 mV is shown. The simulation was finished manually at iteration number 1806.
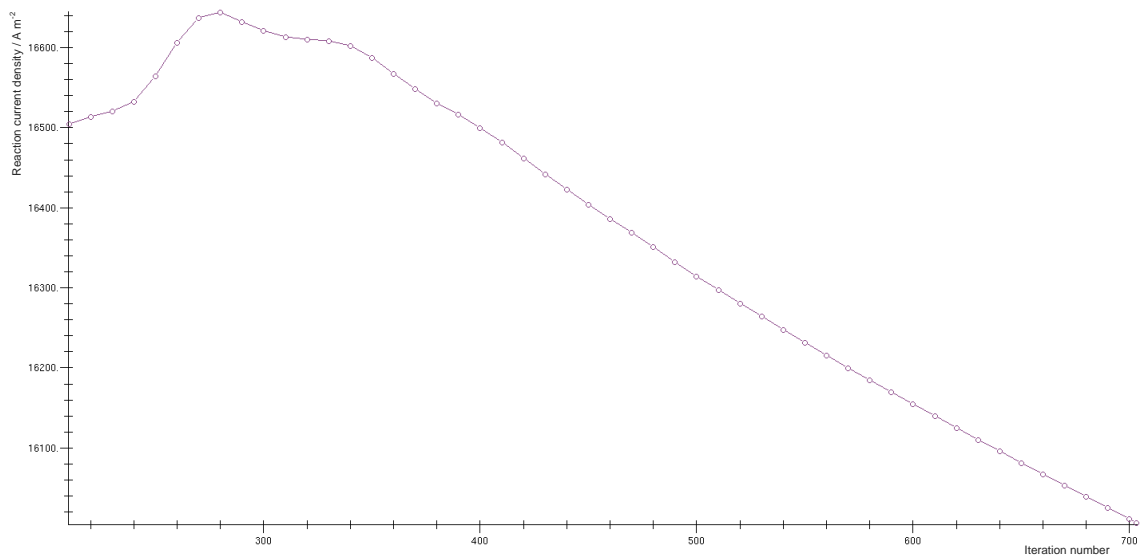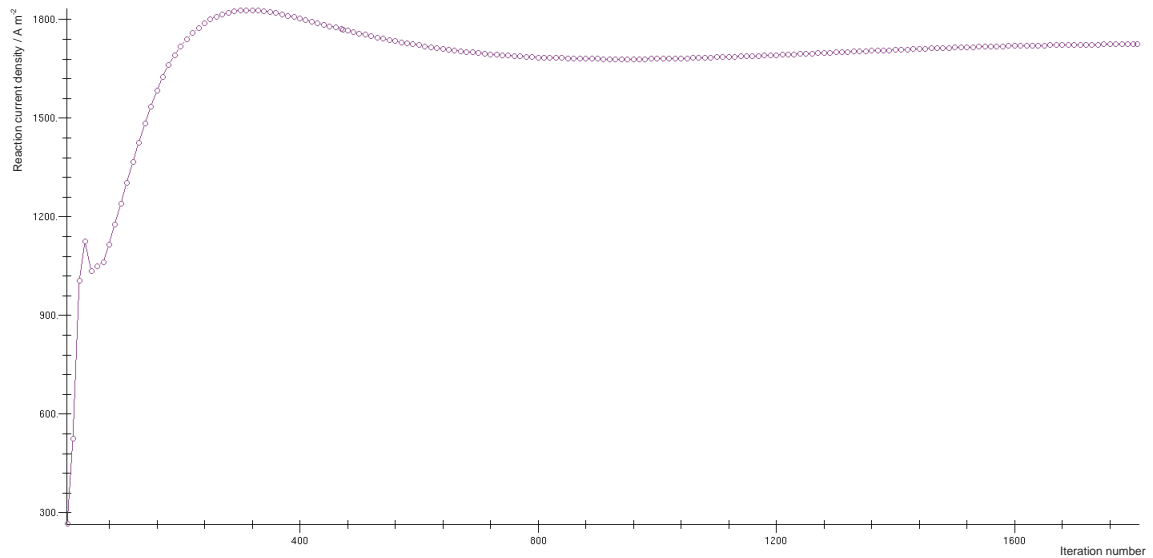

Figure 66: Reaction current density convergence behavior for 800 mV. The course of the reaction current density / A m^{-2} along the iteration number can be seen. At the last iteration the reaction current density showed a value of 1725 A m^{-2}.
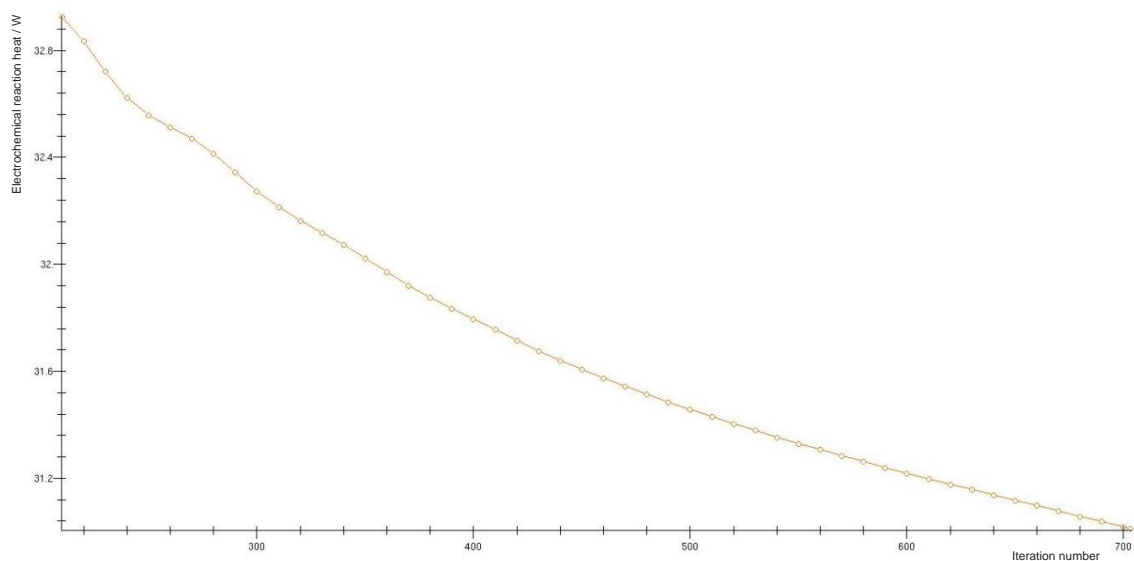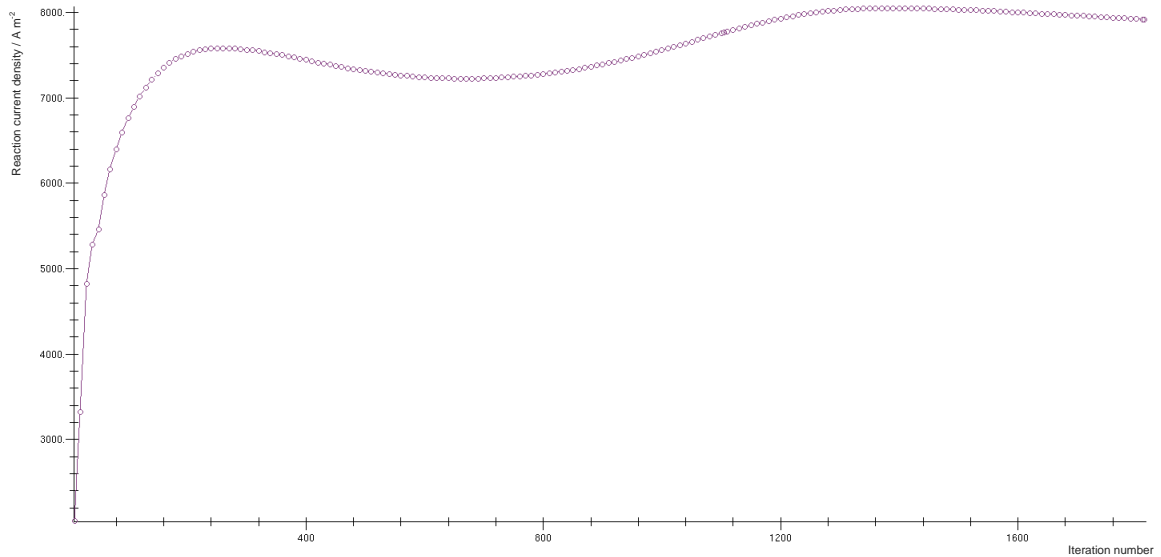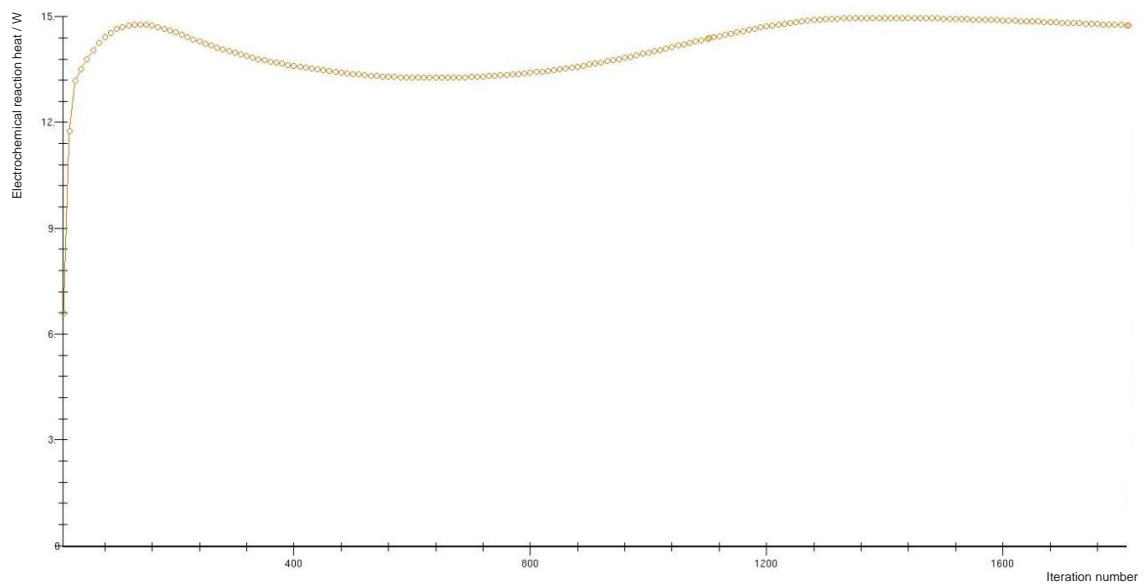

Figure 67: Electrochemical reaction heat / W at 800 mV. As expected the reaction heat convergence is similar to the reaction current density convergence.
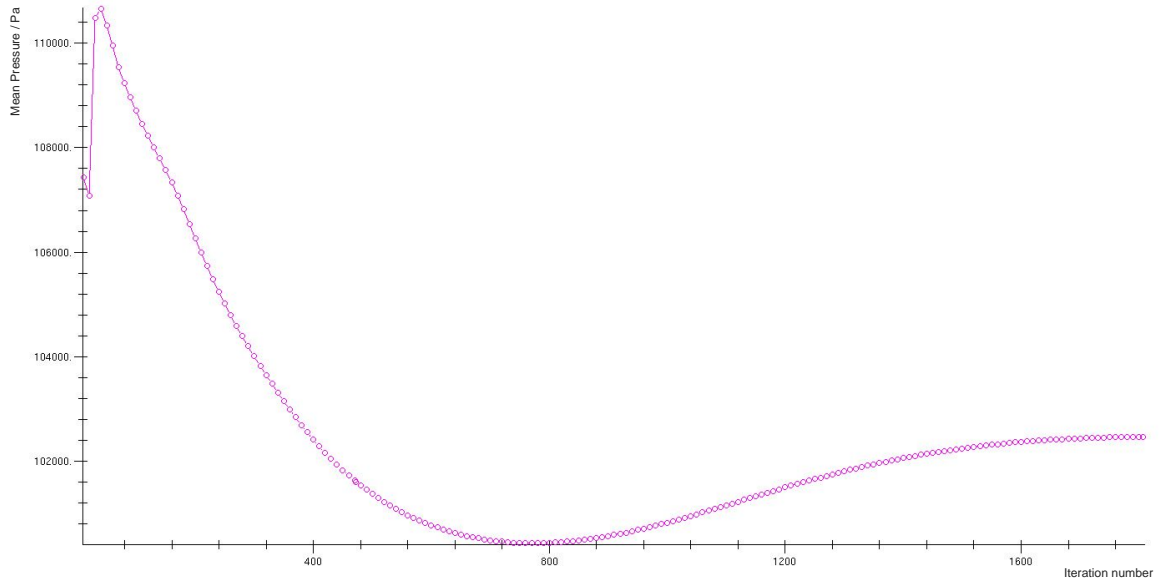
Figure 68: Pressure convergence behavior for 800 mV. The mean pressure / Pa within the fuel cell can be observed.
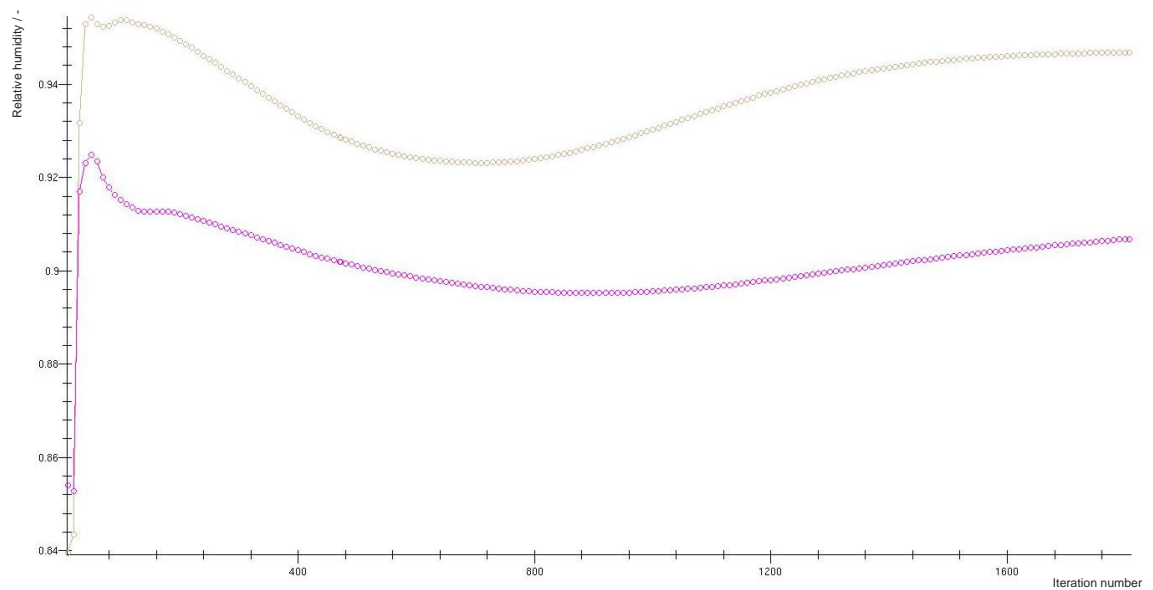
Figure 69: Relative humidity of the gas diffusion layer for the anode (magenta) and the cathode (light brown) at 800 mV. The observation takes place at the *Ano_RL* and *Cat_RL* cell selections. As shown above, they are defined as the cell layer of the anode and cathode GDL next to the membrane mesh. The relative humidity of the *Ano_RL* is shown in magenta; the relative humidity of the *Cat_RL* is shown in light brown.
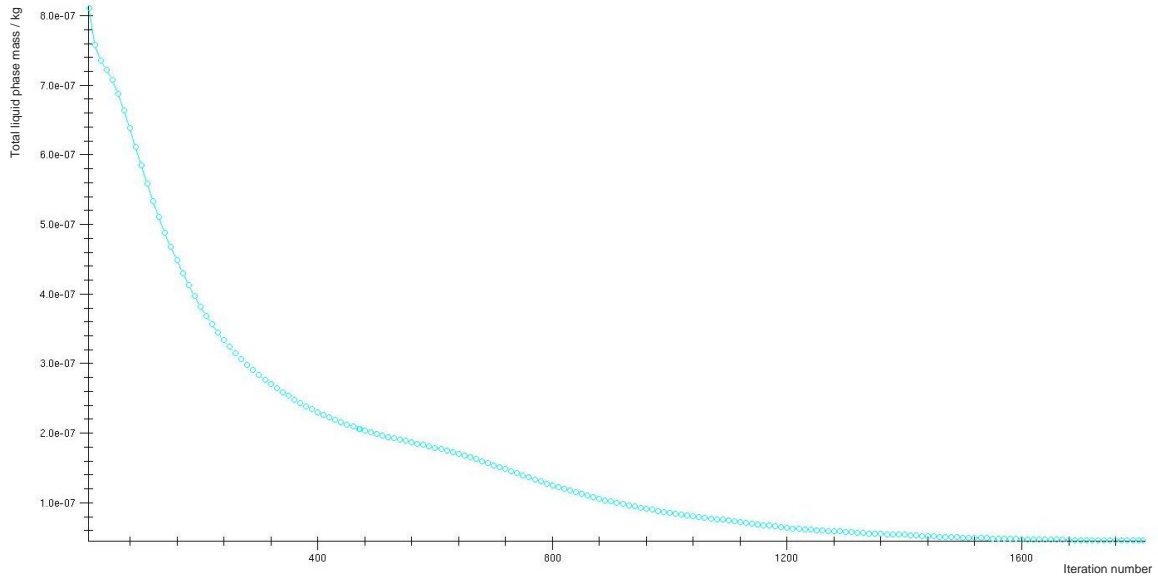
Figure 70: Total mass of liquid water phase / kg at 800 mV within the fuel cell.

```
*************************************************************************************************
*                                                                                             *
*    RUNTIME ANALYSIS AT END OF CALCULATION                                                   *
*                                                                                             *
*************************************************************************************************
*    Total MPI Timings              Count        Total CPU Time        Average WCT            *
*************************************************************************************************
*    ACCIF_EXCHANGE                  19068             0.26                  0.01             *
*    CpTempCalc                      75560           682.87                 41.75             *
*    Energy                          28320        483328.31              28397.59             *
*    File IO                         56480         20105.45               5024.42             *
*    Mesh time update                 9440           123.94                  7.36             *
*    Momentum                        18880        317145.00              18662.11             *
*    Other                              20       1934532.00             159023.23             *
*    Pressure                         9440       1934495.00             124485.73             *
*    TherChem                       852880        292128.56              17180.87             *
*    VolFrac                         18880        132378.31               7816.99             *
*************************************************************************************************
*    Total Execution                    20       5116104.50             360768.25             *
*************************************************************************************************


*************************************************************************************************
*                                                                                             *
*    RUNTIME ANALYSIS AT END OF CALCULATION                                                   *
*                                                                                             *
*************************************************************************************************
*    Total MPI Timings              Count        Total CPU Time        Average WCT            *
*************************************************************************************************
*    ACCIF_EXCHANGE                  53594             0.61                  0.03             *
*    CpTempCalc                     213320          1901.94                107.10             *
*    Energy                          79980       1387910.12              76675.49             *
*    File IO                        146400         56989.41               4138.23             *
*    Mesh time update               26660           312.30                 17.54             *
*    Momentum                        53320        887281.94              49004.64             *
*    Other                              20       4746885.50             292412.56             *
*    Pressure                        26660       3462943.25             220179.95             *
*    TherChem                      2407820        787019.19              43493.05             *
*    VolFrac                         53320        373538.06              20742.12             *
*************************************************************************************************
*    Total Execution                    20      11706324.00             707017.31             *
*************************************************************************************************
```
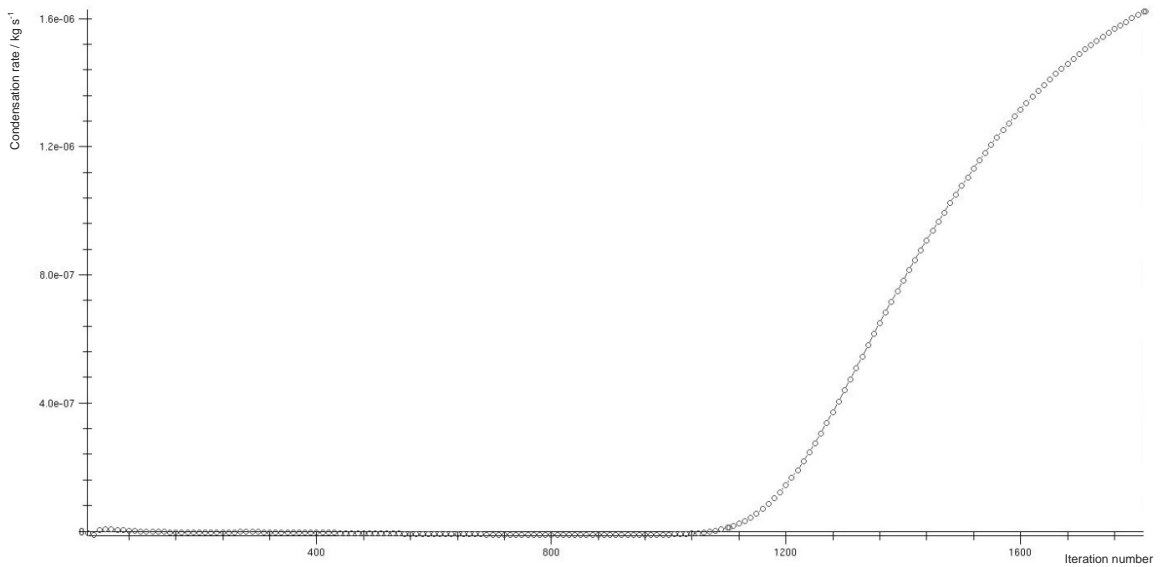
Figure 71: Runtime analysis for the calculation at 800 mV. As the calculation has been interrupted and restarted once, two separate analyses exist. The Average Wall Clock Time (Average WCT) shows the calculation time required / s. The sum of both total executions is 1067785 s. This value correlates to 296.6 h or 12.4 d. As can be seen, the most calculation time is required for "Pressure" (approx.32 %) and "Other" (approx. 42 %). The calculations realized by the Fuel Cell Module containing the electrochemical reaction mechanisms are categorized as "Other". Experimentation and optimization of the underrelaxation factors in question may lead to diminished calculation time.

Convergence of Spatial Distribution Simulation

Subsequently, the iteration behavior for the comparison of spatial distribution characteristics is shown. The simulation was finished manually at iteration number 2738.
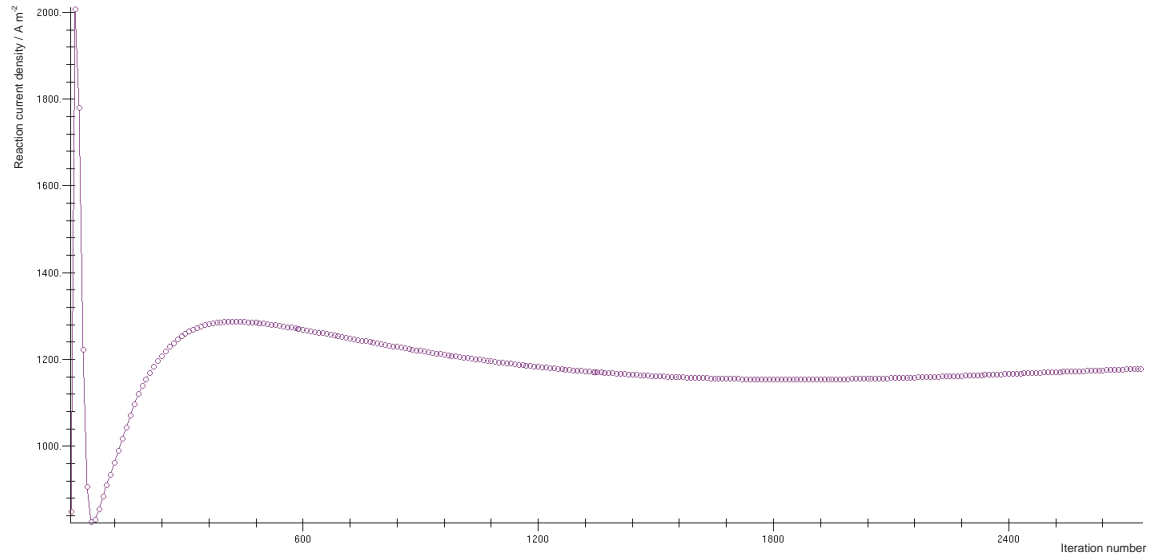
Figure 72: Reaction current density convergence behavior for comparison of spatial distribution characteristics. The reaction current density / A m⁻² in dependence on the iteration number can be seen. At the last iteration, the reaction current density showed a value of 1178 A m⁻².
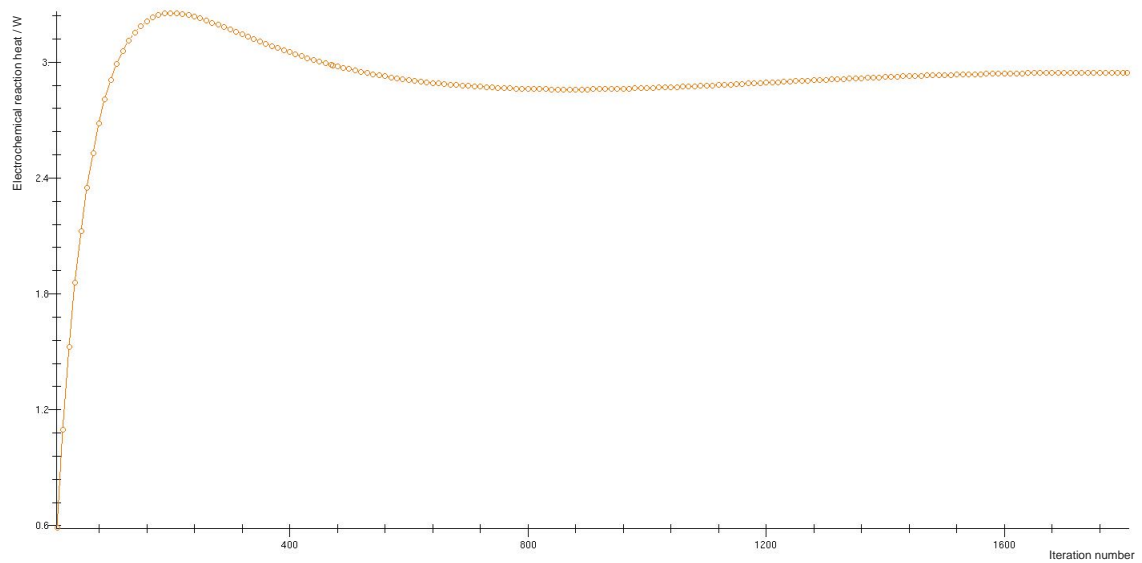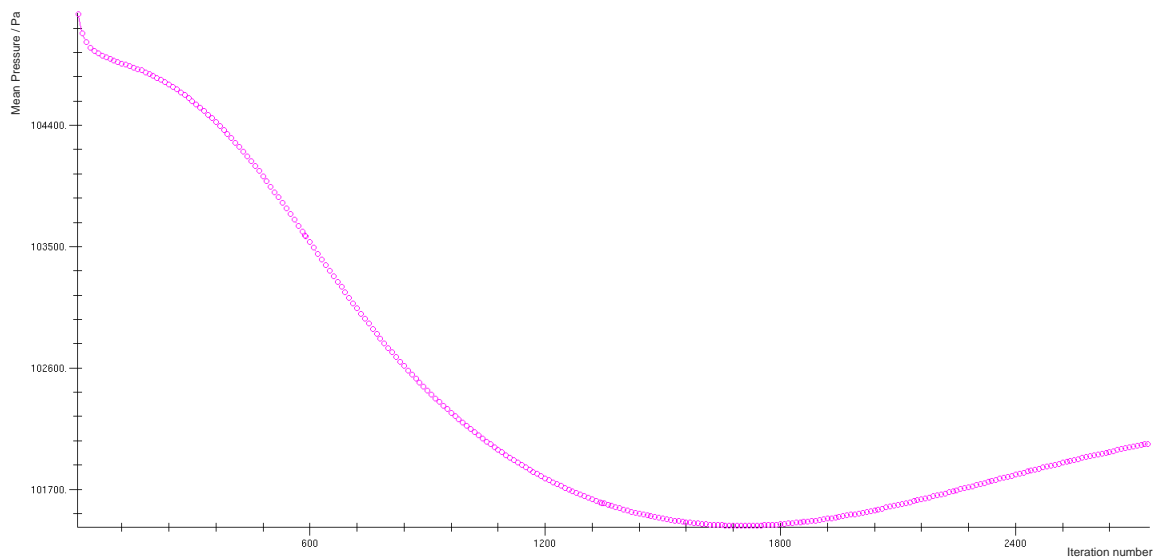

Figure 73: Pressure convergence behavior for comparison of spatial distribution characteristics. The mean pressure / Pa within the fuel cell can be observed.
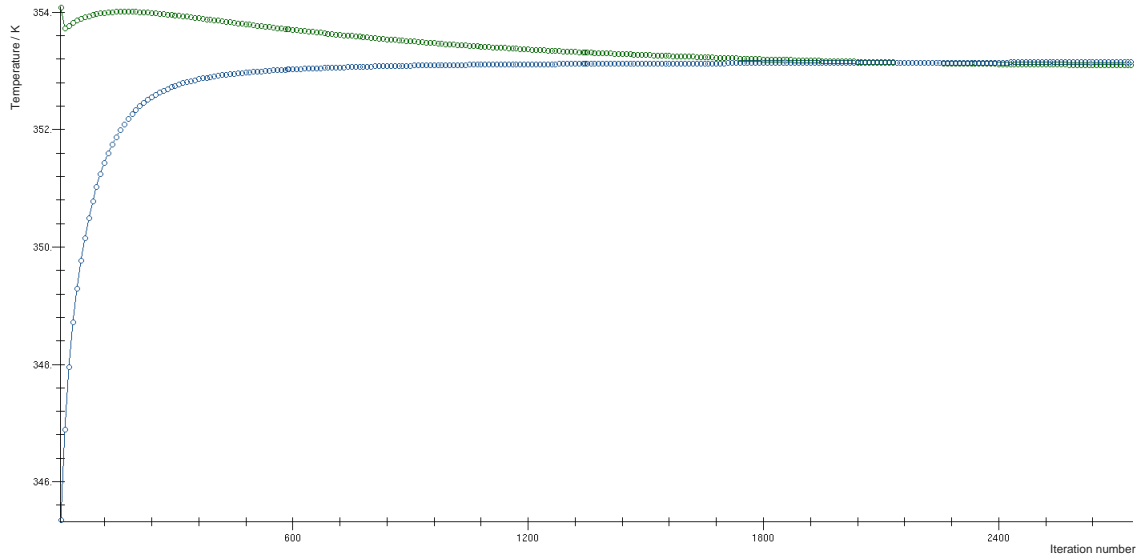
Figure 74: Temperature convergence for comparison of spatial distribution characteristics. The y-axis shows the tempera-ture / K. The temperature of the gas phase within the flow field channels (green) is approached by the temperature of the porous GDL-media (blue).
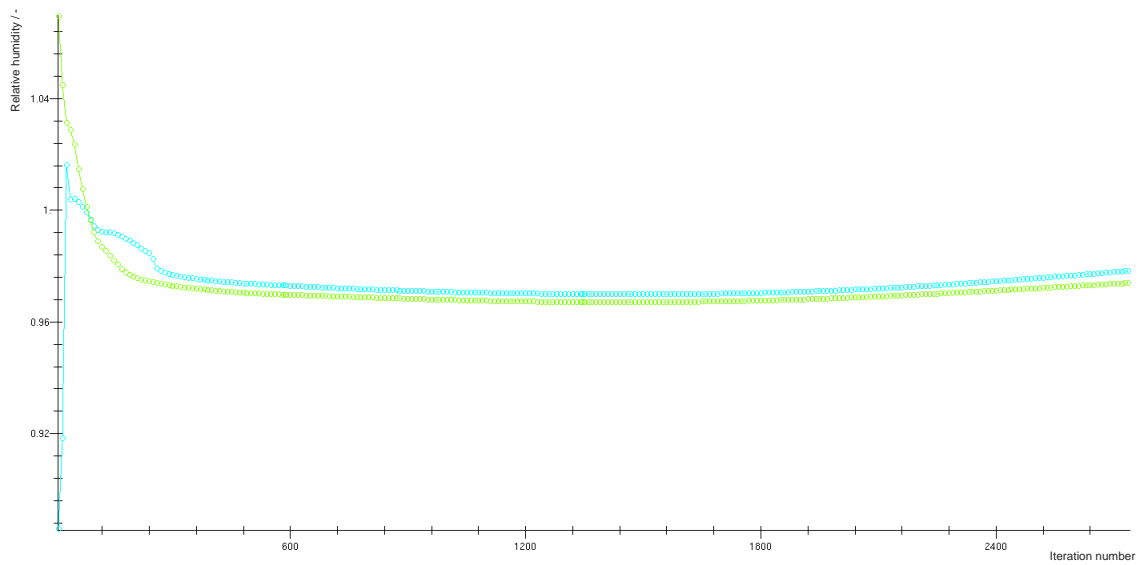
Figure 75: Relative humidity of the gas diffusion layer for the anode (light green) and the cathode (light blue) for comparison of spatial distribution characteristics. The observation takes place at the *Ano_RL* and *Cat_RL* cell selections. As shown above, they are defined as the cell layer of the anode and cathode GDL next to the membrane-mesh. The relative humidity of the *Ano_RL* is shown in light green, the relative humidity of the *Cat_RL* is shown in light blue.

Figure 76: Total mass of liquid water phase / kg within the fuel cell for comparison of spatial distribution characteristics.

```
*******************************************************************************************
*                                                                                         *
*    RUNTIME ANALYSIS AT END OF CALCULATION                                               *
*                                                                                         *
*******************************************************************************************
*    Total MPI Timings                Count       Total CPU Time        Average WCT       *
*******************************************************************************************
*    ACCIF_EXCHANGE                   23679                0.26                0.01        *
*    CpTempCalc                       93960              607.85               31.50        *
*    Energy                           35220           473840.25            24421.64        *
*    File IO                          68600            20756.54             2494.27        *
*    Mesh time update                 11740               61.97                3.30        *
*    Momentum                         23480           299062.94            15407.31        *
*    Other                               20          1878377.38           133245.33        *
*    Pressure                         11740          1030080.50            64518.73        *
*    TherChem                       1059700           289491.84            14938.88        *
*    VolFrac                          23480           134697.95             6955.35        *
*******************************************************************************************
*    Total Execution                     20          4127531.75           262079.12        *
*******************************************************************************************


*******************************************************************************************
*                                                                                         *
*    RUNTIME ANALYSIS AT END OF CALCULATION                                               *
*                                                                                         *
*******************************************************************************************
*    Total MPI Timings                Count       Total CPU Time        Average WCT       *
*******************************************************************************************
*    ACCIF_EXCHANGE                   30497                0.34                0.02        *
*    CpTempCalc                      121160              733.39               45.36        *
*    Energy                           45420           692524.06            41134.70        *
*    File IO                          86420            25029.50            11579.24        *
*    Mesh time update                 15140              243.47               14.32        *
*    Momentum                         30280           446587.62            26529.98        *
*    Other                               20          2916249.25           193453.47        *
*    Pressure                         15140          1574341.25           111299.08        *
*    TherChem                       1370360           441769.34            26215.26        *
*    VolFrac                          30280           202909.69            12209.87        *
*******************************************************************************************
*    Total Execution                     20          6301190.50           422600.38        *
*******************************************************************************************


*******************************************************************************************
*                                                                                         *
*    RUNTIME ANALYSIS AT END OF CALCULATION                                               *
*                                                                                         *
*******************************************************************************************
*    Total MPI Timings                Count       Total CPU Time        Average WCT       *
*******************************************************************************************
*    ACCIF_EXCHANGE                   55960                0.56                0.03        *
*    CpTempCalc                      222760             1347.01               72.21        *
*    Energy                           83520          1212470.12            64319.82        *
*    File IO                         152700            41147.53             2924.93        *
*    Mesh time update                 27840              331.86               17.93        *
*    Momentum                         55680           765699.56            40614.78        *
*    Other                               20          4503723.50           268513.94        *
*    Pressure                         27840          2515819.50           161618.83        *
*    TherChem                       2514220           706188.12            37527.00        *
*    VolFrac                          55680           344175.34            18354.79        *
*******************************************************************************************
*    Total Execution                     20         10092020.00           594122.75        *
*******************************************************************************************
```
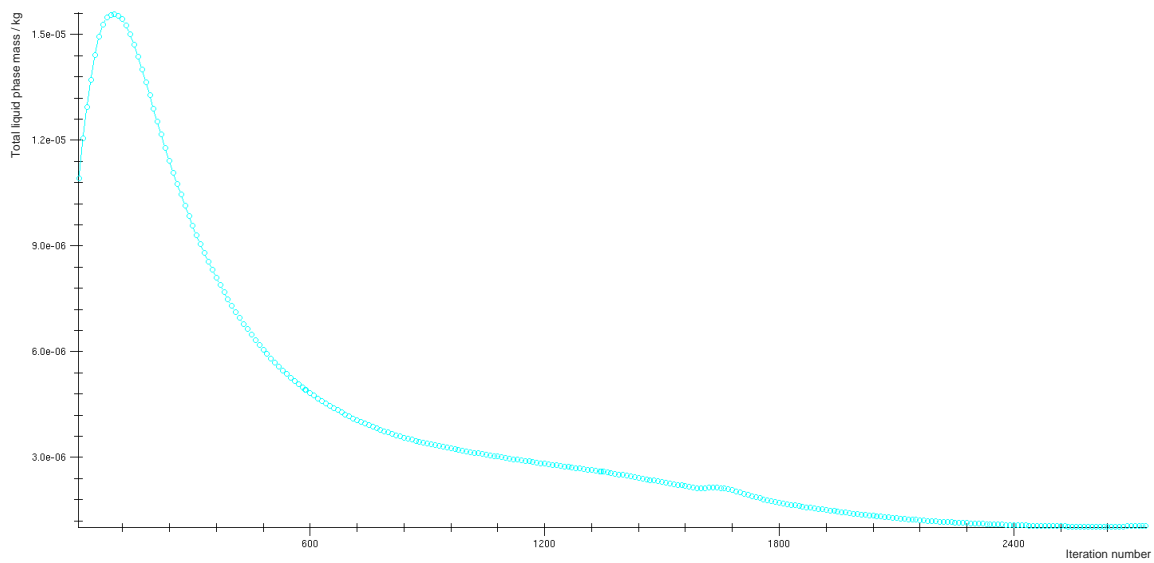
Figure 77: Runtime analysis for the calculation of spatial distribution comparison. As the calculation has been interrupted and restated twice, three separate analyses exist. The Average Wall Clock Time (Average WCT) shows the calculation time required / s. The sum of all three total executions is 1278801 s. This value correlates to 355.2 h or 14.8 d. As can be seen, the most calculation time is required for "Pressure" (approx. 26 %) and "Other" (approx. 47 %). The calculations realized by the Fuel Cell Module containing the electrochemical reaction mechanisms are categorized as "Other". Experimentation and optimization of the underrelaxation factors in question may lead to diminished calculation time.